A LONGITUDINAL BRAIN-MACHINE INTERFACE TRAINING PARADIGM WITH A LOWER-LIMB EXOSKELETON & ITS INDUCED CORTICAL CHANGES

by

Kevin C. Nathan

A dissertation submitted to the Department of Electrical & Computer Engineering

Cullen College of Engineering

in partial fulfillment of the requirements for the degree of

Doctor of Philosophy

in Electrical & Computer Engineering

Chair of Committee: Jose L. Contreras-Vidal

Committee Member: Robert G. Grossman

Committee Member: Rose Faghih

Committee Member: David Mayerich

Committee Member: Yingchun Zhang

University of Houston

May 2021

Acknowledgements

I would first and foremost like to thank my advisor, Dr. Jose L. Contreras-Vidal, for his guidance and support during my research and education pursuits. I have learned so much during my time in this research group and look forward to applying the many skills I gained in my career going forward. I would like to thank Dr. Robert Grossman, Dr. Rose Faghih, Dr. David Mayerich, and Dr. Yingchun Zhang for their participation on my dissertation committee. This project was made possible through funding support from the Houston Methodist Foundation, the Cullen Foundation, and Mission Connect - a TIRR Foundation.

I would also like to give a special acknowledgement to Dr. Atilla Kilicarslan, who initially spearheaded the NeuroREX project from its inception as a postdoctoral fellow, including developing the initial real-time control architecture, classification algorithm, and training paradigm. I'm additionally grateful for the contributions to members of Dr. Zhang's lab and the Houston Methodist Research Institute for their assistance in fMRI data collection, including Thinh Nguyen, Tom Potter, and Dr. Christof Karmonik.

Many additional thanks to the current and former members of the Noninvasive Brain-Machine Interface Systems Lab, for all of the years of mutual support, collaboration, feedback, and comradery. I owe much of the success of this dissertation, the completion of my graduate education, and invaluable friendship and memories to all of you: Akshay, Alex, Alexander, Anastasiya, Andrew, Ani, Anusha, Aryan, Bryan, David, Eric, Fangshi, Harsha, Jeff, Jesus, Jiajun, Jonathan, Jose, Justin, Kim, Luu, Manuel, Marianna, Mario, Michelle, Nikunj, Prasad, Rahul, Recep, Ryan, Sam, Sho, Teresa, Yongtian, and Zach.

Lastly, I would not have been able to achieve all of this without the support of all my family and friends, for being the support I needed every step of the way that I could rely on to refresh and recharge away from my work. Thank you to everyone for all of your help in completing this endeavor.

Abstract

Introduction: Brain-machine interfaces (BMIs) have been developed to enable cognitive control of computers and robotic devices. Such technology might potentially lead to restoring movement for persons with motor disabilities by allowing them to control robotic prostheses or orthoses naturally with their mind. However, BMIs are still in their infancy, and long-term usage with closed-loop systems has not been thoroughly studied, nor the subsequent changes in the brain induced by cortical plasticity.

Methods: Seven able-bodied subjects were recruited for a longitudinal BMI training paradigm with the Rex lower-limb exoskeleton. Participants developed their ability to use motor imagery over nine sessions to initiate the Rex's walking and stopping as a Go-No Go task. The BMI consisted of active EEG processed through a Localized Fisher Discriminant Analysis dimensionality reduction and a Gaussian Mixture Model classifier on time-lagged δ band amplitudes. Training data were accumulated to update the decoding model over the first five sessions, after which model parameters were fixed for subjects to adapt to their personalized model. Subjects underwent a final session with simultaneous EEG-fMRI recording while watching video playback of themselves walking in the Rex performing the same motor imagery.

Discussion: BMI decoding for control of the Rex's gait varied among the subjects, with at least some achieving significantly above chance classification performance by the end of training. The fMRI scans showed contrasts in activation between the Walk and Stop conditions localized in the precentral gyrus among other areas associated with motor imagery. Offline EEG analysis identified ERPs corresponding to the walk cue, but these may not have been reliably detected by the classifier.

Significance: The novelty in this study is the extended use of a subject pool continuously for many sessions of BMI training to control a walking exoskeleton. The longitudinal aspect provides insights into how much training subjects may need to achieve reliable classification, what factors separate good BMI operators from poor ones, and what other features may be more relevant in future BMI applications.

Table of Contents

List of Tables

List of Figures

Chapter 1

Introduction

Recent estimates indicate that paralysis and other motor disabilities afflict more than 5 million individuals in the United States [1]. Spinal cord injury (SCI), stroke, and multiple sclerosis together account for nearly 80% of these cases; for SCI in particular, more than 80% of cases are attributed to either motor vehicle accidents, falls, or acts of violence (primarily gunshot wounds) [2]. In addition to drastically reducing the quality of life due to lack of mobility, SCI incurs monumental costs to both the patients and the overall healthcare system of more than $40 billion annually [3]. Nearly 42% of the paralyzed population are unable to work due to disability, with lifetime costs of care accruing up to $2.5 million for individuals with paraplegia and more than double that amount for those with tetraplegia. These figures make clear the need for seeking novel methods to restore movement and mobility for the paralyzed population.

Conventional means of restoring motor function via physical rehabilitation are often variable and incomplete, particularly in the case of gait and the ability for patients to independently navigate their environment. Bottom-up approaches are typically applied when there is some residual ability for movement: therapists act on the distal physical level (bottom) aiming to influence the neural system (top), thereby promoting mechanisms of neural plasticity [4]. Traditional therapies to improve functional ambulation for patients may involve overground training and require designed preparatory exercises, observation by a physical therapist, direct manipulation of the limbs during gait over a regular surface, followed by supervised walking. This type of physical rehabilitation is both physically burdensome and time-consuming for the therapists, as such repetitive guided movements can be performed more consistently

by robotic systems.

For motor restoration and rehabilitation, powered robots in the form of orthotic exoskeletons use actuators to apply torques on the joints of the leg to assist in gait. While prosthetic systems also exist whereby an amputated limb is wholly replaced, we focus here only on the former category, which act externally on the disabled limbs to either restore movement if the limb is paralyzed or to rehabilitate the limb if recovery can be expected through reforming the neuromuscular pathways. Exoskeletons have been used extensively for motor rehabilitation as part of robot-assisted gait therapy [5, 6, 7], having been shown to have bottom-up changes on the brain, even when only physically affecting the lower limbs [8, 9, 10], and even more so when combined with neural stimulation [11, 12, 13, 14, 15]. However, these devices are generally operated by unnatural physical maneuvers, e.g., pressing buttons or joysticks [16] or shifting body weight to initiate walking [17].

Brain-machine interfaces (BMIs), which record the users' brain signals to detect motor intent, hope to substitute a volitional cognitive control for users who are fully dependent on these devices, to regain a mobility as seamless as they had prior to injury. This also ensures cognitive engagement in the motor task, thereby promoting stronger neuroplasticity [18, 19, 20, 21, 22]. BMI efforts involving the surgical implantation of electrodes in the brain have gone as far to enable tetraplegic patients to manipulate a robotic arm to feed themselves [23, 24, 25, 26]. But while these invasive BMIs offer more reliable signals for better control, these come at the expense of greater risk from the surgical procedures, higher costs, and complications due to implant degradation over time. Similar, but weaker, neural signals can be recorded from the scalp through electroencephalography (EEG) use in a non-invasive BMI system. Much of the focus on BMI research has been aimed at upper-limb reaching tasks [27], but a review of the relevant literature concerning EEG control of lower-limb exoskeletons for walking concludes a need for significant improvement in reliability and

accuracy for these systems to be adopted outside of the highly controlled environment of a lab or clinic [28]. Moreover, limited longitudinal studies leave the long-term effects on performance and changes in the brain as a result of extended BMI training to be underexplored.

A study by Donati et al. [29] is of particular note since it demonstrated induced neurological recovery in 8 SCI patients through long-term EEG-based BMI training with an exoskeleton. The intensive 12 month training paradigm incorporated nearly 600 collective hours for a combination of traditional rehabilitation with a treadmill-based exoskeleton and overground harness-supported walking; BMI training in a virtual environment with tactile feedback; and BMI control of both the treadmill-based exoskeleton and a separate overground exoskeleton system. As a result of the training, the reported results indicated major neurological improvements in somatic sensation, recovery of some voluntary motor control below the level of injury, and an upgrade from complete to incomplete SCI classification in half the patients. While this was indeed a significant achievement showcasing new rehabilitation potential for EEG-based BMI systems, the wide breadth of the training protocol obfuscates what would be minimally necessary to reproduce the same results for other patients and leaves unanswered the isolated contribution of extensive BMI training with an exoskeleton.

This dissertation aims to address the high-level question of whether individuals can be trained to control a walking exoskeleton with their EEG, and if this can ultimately be a means to restore mobility for the paralyzed population. The hypothesis proposed is that able-bodied subjects can be trained to elicit their kinesthetic motor imagery (KI) [30, 31] to initiate walking and stopping in a robotic exoskeleton, and that longitudinal training will both show improved performance and induce plasticity in the cortical pathways underlying the imagery of gait. This hypothesis will be investigated by addressing the following two specific aims:

Specific Aim 1 (SA1): Assess the ability to predict from δ band EEG the intention

of users to walk and stop while controlling a robotic lower limb exoskeleton.

Specific Aim 2 (SA2): Identify the neural correlates of KI through offline analysis of electroencephalography and functional magnetic resonance imaging, and how these correlates relate to brain-machine interface performance.

The remaining chapters of this dissertation will be organized as follows. The second chapter will focus on Specific Aim 1, providing a review of the relevant literature pertaining to BMI control of lower-limb exoskeletons; describing the experimental paradigm, technical specifications, and the data collection for the overall study; and then presenting the results and analysis from the BMI decoding task. The third chapter will be dedicated to Specific Aim 2, reviewing our current understanding of KI and the analysis of its representation in our EEG and fMRI data during this BMI task. In the fourth and final chapter, the dissertation will wrap up the conclusions evaluating the efficacy of this longitudinal BMI paradigm.

Chapter 2

Longitudinal Brain-Machine Interface Training to Control a Walking Robotic Exoskeleton

2.1 Introduction

The feasibility for brain-machine interface technologies to allow for EEG-control of locomotion could be traced back as early as 1994, when leg movements were found to elicit distinct event-related synchronization (ERS) patterns, i.e., changes in spectral power cued to an event, over motor areas [32]. Identification of neural signatures of isolated leg movements would be pivotal for generating command signals for BMI-based robotics. Merely distinguishing differences in ERS patterns would not be sufficient however, since such differences could only be ascertained by averaging over numerous trials, thus not being viable for real-time control. Later attempts would circumvent extracting signals from motor intent for BMIs by instead using more easily identifiable evoked potentials. BMI studies throughout the 2000s often used flashing visual stimuli to elicit P300 and SSVEP signals that could be used to control the navigation of a motorized wheelchair [33, 34, 35], manipulate a robotic arm [36, 37, 38], and even control the walking of a humanoid robot [39]. However, these evoked potentials are not inherently motor signals and do not correspond with neural patterns arising from natural volitional movement.

More precise prediction of lower-limb kinematics was demonstrated first in non-human primates walking on a treadmill by applying a linear decoder to neuronal spiking rates from invasive recordings [40]. The results were later replicated in a study with healthy humans during treadmill walking using the same type of continuous decoder on low-frequency δ band EEG amplitudes, the first demonstration of decoding gait patterns noninvasively [41]. This was corroborated by earlier fMRI studies in which cortical activation was detected during motor imagery of walking in both healthy [42] and paraplegic subjects [43], opening the field for future studies employing EEG-based BMI systems for the control of lower-limb exoskeletons described below and summarized in 2.1. The table uses the following abbreviations for Task types: W-walk, S-stand, Kin-continuous kinematics, W_p-passive walk, W_a-active walk, L-turn left, R-turn R, K-kick, A-acceleration, D-deceleration; and for Classifier types: NB-Naive Bayes, GMM-Gaussian Mixture Model, UKF-Unscented Kalman Filter, LogReg-Logistic Regression, k-NN - k-Nearest Neighbor, CCA-Canonical Correlation Analysis, LDA-Linear Discriminant Analysis, SDA-Sparse Discriminant Analysis, CNN-Convolutiontal Neural Networks, RF-Random Forest, CVA-Canonical Variant Analysis, MKL-SVM - Multiple Kernel Learning Support Vector Machine.

The efforts in [41] were extended to overground walking with an exoskeleton (X1, NASA) with two healthy subjects and one stroke survivor [44]. Lower limb joint angles and EMG envelopes were predicted offline with an unscented Kalman filter under walking conditions with and without the exoskeleton in both active and passive modes. A longitudinal study with five stroke survivors undergoing rehabilitation and robot-assisted gait training with the H2 exoskeleton (Technaid S.L., Spain) showed offline decoding accuracy of the angular kinematics (also using an unscented Kalman filter) improved over the course of the 12 training sessions [45]. These methods were also employed in a closed-loop setting for a walking virtual avatar with moderate accuracies [46, 47, 48]. Only one study [49] was found that performed closed-loop continuous prediction of joint angles in an exoskeleton: albeit this was a hybrid approach based

on using EEG for high level class decoding (stop, normal walk, accelerate, and decelerate) and joint angle trajectories were governed by EMG amplitudes in a central pattern generator model.

It is essential for continuous decoding of joint angles to be extremely robust to ensure safe closed-loop control of an exoskeleton. Current results have not yet demonstrated this reliably, and most closed-loop efforts have focused on simpler binary classification of walking versus stopping or standing. The feasibility of closed-loop control of an exoskeleton was demonstrated in 2013 with a single SCI patient [50] using the REX exoskeleton: this study used δ band EEG in a Gaussian mixture model and saw an accuracy improvement from 21% to 70% over the first period of trials with 90% accuracy on the final trial. The algorithm is later evaluated with an H^{∞} artifact removal algorithm and saw up to a 10% improvement in offline decoding accuracy for two able-bodied subjects trained over 9 sessions [51]. Another 2013 study [30] used the treadmill-confined RoGO Lokomat (Hocoma, Switzerland) with one able-bodied and one SCI patient each with a Bayesian classifier and features from the integrated power spectral density over 1-40 Hz was used. Studies with the H2 exoskeleton detected gait intention with features from both ERD (7-25 Hz) and movement-related cortical potentials (MRCPs, 0.1-1 Hz) through sparse discriminant analysis and a linear classifier first with three able-bodied subjects and four with paraplegia from SCI [52] and then with four incomplete SCI patients using [53]. One more study with the H2 [54] showed that applying tDCS could improve BMI performance in four healthy subjects. Finally, one more binary-class study employed a customized lower-limb gait training exoskeleton [55], evaluating two independent naive Bayes models based on sensorimotor rhythms (SMRs) and MRCPs.

Some closed-loop BMI applications have attempted to expand beyond the two class problem, to distinguish between three or more commands for the exoskeleton. The first study with multi-state classification attempted to use 8-30 Hz ERD features

in a logistic regression classifier to distinguish offline between active walking, passive walking, and rest using the RoGO Lokomat for healthy subjects and stroke patients [56]. Other studies have used SSVEP to distinguish between turning left and right and speeding up in the XYKXZFK-9 rehabilitation robot (Xiangyu Medical Equipment Co. Ltd., China) [57], and between walking, stopping, accelerating, and decelerating in the hybrid EEG-EMG BMI study with the custom exoskeleton described in [49]. Several multi-state classification studies were performed with the REX: one closed-loop study [58, 59] with 11 healthy subjects used SSVEP to navigate a course consisting of 10 sit/stand cycles and walking along a marked circle both clockwise and counter-clockwise; another achieved three class closed-loop classification (walk forward versus turn left/right) by cascading two binary classifiers [60]; and another using δ band amplitudes achieved four state classification (walk, stop, turn left, turn right) for one able-bodied and one SCI subject using multiple kernel support vector machines (SVMs) [61].

Few studies have attempted to conduct multiple sessions with the same subjects due to inherent difficulties in subject retention and commitment, even though extended BMI training in an exoskeleton has shown to have clinical benefits. Contreras-Vidal et al. [45] showed improved functional ambulatory ability in a longitudinal study with chronic stroke survivors that trained with the H2 for 12 sessions across four weeks; the improvements were correlated with the increase in the decoding accuracy of the BMI, suggesting an improved neural representation for gait in the damaged cortex. As described in Chapter 1, Donati et al. [29] demonstrated landmark neurological recovery in eight complete SCI patients after an intensive 12-month rehabilitation protocol with a custom exoskeleton. To investigate the role of extensive exoskeleton BMI training by itself, we explore here the ability to evaluate binary-state closed-loop control in a longitudinal BMI paradigm with multiple able-bodied subjects over a large number of sessions.

Table 2.1: Studies incorporating BMI control of lower-limb exoskeletons. Closed-loop BMI control denoted with *. This table is an updated adaptation from a previous review paper [28].

First Author	Year	Robotic Device	Subjects		BMI				
			Impaired	Able-bodied	Tasks	Pre-Processing	Feature Extraction	Dimensionality Reduction	Classifier
Do [30]*	2013	RoGO Lokomat	1 SCI	1	W,S	CAR, noisy channels removed	0–40Hz ERD	CPCA, AIDA	NB
Kilicarslan [50]*	2013	REX	1 SCI	-	W,S	—	0.1-2Hz MRCP	LFDA	GMM
He [44]	2014	NASA X1	1 stroke	2	Kin	CAR	0.1-3Hz MRCP	PCA	UKF
García-Cossio [56]	2015	RoGO Lokomat	3 stroke	10	W_p, W_a, S	CAR, CCA, Laplacian	8–30Hz ERD	-	LogReg
Kwak [58]*	2015	REX	-	11	W,L,R,S,Sit	CCA	SSVEP	-	k-NN
Zhang [57]*	2015	XYKXZFK-9	-	3	W,L,R,S,A,D	-	SSVEP	-	CCA
Donati [29]*	2016	RoGO Lokomat, custom exo	8 SCI	-	W,S,K	CAR	CSP (arm MI)	-	LDA
Kilicarslan [51]*	2016	REX	-	2	W,S	H^∞	0.2-3Hz MRCP	LFDA	GMM
López-Larraz [52]*	2016	H2	4 SCI	3	W,S	CAR, noisy trials removed	7–25Hz ERD, 0.1–1Hz MRCP	-	SDA
Gui [49]*	2017	Custom exo	2	10	Kin	-	SSVEP	-	LDA
Kwak [59]	2017	REX	-	7	W,L,R,S,Sit	-	SSVEP	-	CNN
Lee [60]*	2017	REX	-	5	W,L,R	CAR	14–19Hz ERD	-	RF
Liu [55]*	2017	Custom exo	-	6	W,S	Laplacian, CAR	4–48Hz SMR, 0.1–1Hz MRCP	-	CVA-NB
Zhang [61]	2017	REX	1 SCI	1	W,S,L,R	ASR	0.1-2Hz MRCP	-	MKL-SVM
Contreras-Vidal [45]	2018	H2	5	-	Kin	ASR, CAR	0.01-3Hz MRCP	PCA	UKF
Rajasekaran [53]*	2018	H1	4	-	W,S	Optimal spatial filter, CAR, z-score, noisy channels removed	0.1-1Hz MRCP, 7-30Hz ERD	-	SDA
Rodriguez-Ugarte [54]*	2018	H2	-	4	W,S	Laplacian	6-35Hz ERD	-	SVM

2.2 Methods

2.2.1 Subject Demographics

Seven able-bodied participants (four males & three females, ages 20-30; Table 2.2) with no history of neurological disease or physical impairments were recruited in this study to assess their ability to control a walking lower-limb exoskeleton with their brain activity. Subjects provided written informed consent and completed a preliminary health assessment. The clinical progress (monitoring for pain, fatigue, skin condition, and other discomfort) of each subject was documented after each session. Subsequent recruitment of subjects was put on hiatus due to safety concerns during the 2020 COVID-19 pandemic. All experimental protocols were approved by the Institutional Review Board of the University of Houston.

Table 2.2: Subject Info.

Subject ID	**Sex**	**Age (yrs)**	**Enrollment Length (Days)**	**MIQ Score Avg**
S1	M	26	22	5.07
S2	F	22	16	4.71
S3	M	29	15	5.86
S4	F	20	36	6.07
S5	M	23	45	5.71
S6	F	20	81	—
S7	M	30	37	4.64

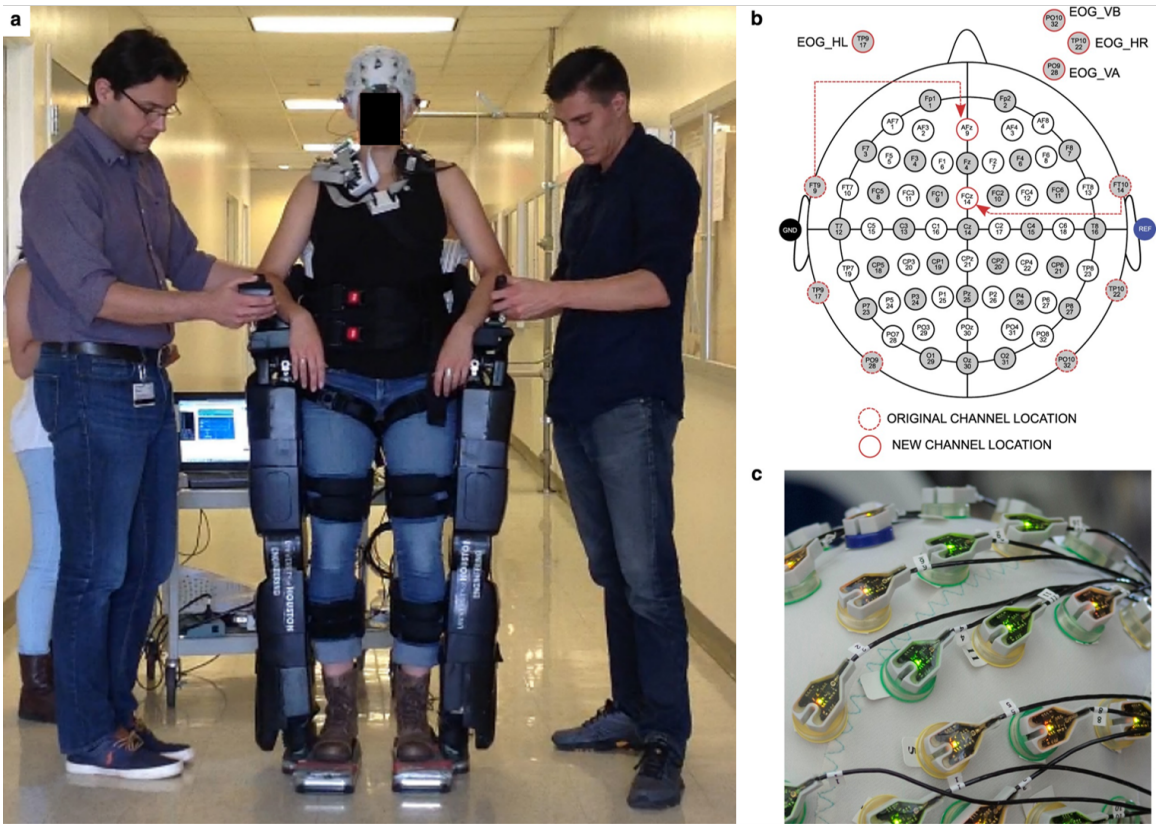

Figure 2.1: (a) Subject in the REX exoskeleton wearing an EEG cap. (b) EEG channel montage and EOG channel locations. (c) Active EEG electrodes. Adapted from [63] CC BY 4.0).

2.2.2 Powered Lower-Limb Robotic Exoskeleton

The REX (Rex Bionics Ltd; Auckland, NZ) is a powered robotic exoskeleton with bilateral actuators on the hip, knees, and ankles, to fully assist in locomotion for people with paralysis, e.g., patients with complete SCI. It is self-balancing thereby alleviating the need for arm supported crutches. The REX can be operated via a joystick to walk forward, walk backward, and turn. For this study, we developed a custom configuration allowing the REX to be operated wirelessly, bypassing the joystick, for the purpose of controlling the walking movements of the REX (initiating walking from stopping and initiating stopping from walking) using a closed loop EEG-based brain-machine interface (Figure 2.1A) [50, 62].

2.2.3 Experimental Task and Paradigm

The experimental paradigm consisted of nine sessions scheduled approximately 2-3 times per week per the subjects' availability. Each session involved a training phase, three blocks of closed-loop testing in a Go/No-Go task (consisting of 4 trials each for a total of 12 trials) [64], followed by two closed-loop 6-minute tests. The training phase involved collection of EEG data from the subject walking in the exoskeleton for six stop-walk-stop (SWS) cycles; the training cycles were preprogrammed such that the REX was in full control of the subjects' legs. A loud auditory beep was used as a cue at the start of the stop-to-walk and the walk-to-stop transitions. During the training, subjects were instructed to elicit kinesthetic motor imagery (KI), i.e., to focus on the contractions of their legs' muscles and joints and imagining the forces they would be exerting if they were controlling their legs themselves. KI has previously been used to identify walking and idle states to control the walking of both a virtual avatar [31] and a physical exoskeleton [30]. The EEG associated with the KI of walking contrasted with that during rest was used as the basis for developing the classifier. The trials of the closed-loop test blocks consisted of a single SWS cycle; subjects heard the same beep cue to signal the start of each of the stop, walk, and second stop phases. Subjects were instructed to continue eliciting their KI according to each phase, but this time the REX would stop or walk depending on the real-time classified output from the decoder. Trials would end prematurely if the subjects experienced failed classifications for 30 consecutive seconds; a successful trial was one in which the subject completed the full SWS cycle while avoiding the 30s timeout. After the 12 trials, subjects performed two more closed-loop tasks: a 6-minute stop task and a 6-minute walk task, trying to maintain either the stop or walk states continuously for 6 consecutive minutes. This would be akin to the common 6-Minute Walk Test clinical assessment commonly used in motor rehabilitation [65]. The protocol is outlined in the top of Figure 2.2.

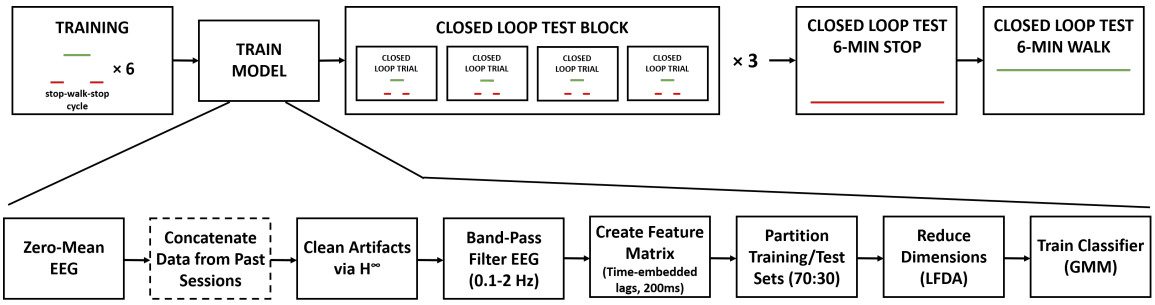

Figure 2.2: Flowchart of the experimental protocol (top) and the real-time EEG signal processing (bottom).

After the first trial, the training data from the prior sessions were concatenated to the current session to increase the robustness of the classifier. After the fifth session, the classifier became fixed and no longer received the new training data so that the subject could then adapt how they evoked their KI based on the classifier performance.

After the 9 BMI sessions, subjects underwent an MRI scan (Philips Ingenia 3.0T, Koninklijke Philips N.V.; Netherlands) for both a T1-weighted structural scan and a fMRI recording. For the functional scans, subjects watched a 10-minute video of themselves walking in the REX for 11 SWS cycles. The video was filmed from the first person view of the subject as if they were looking down at their own legs in the exoskeleton. While watching the video in the scanner, subjects were again asked to try to evoke their KI as if trying to control the exoskeleton.

2.2.4 Data Acquisition and Processing

EEG data sampled at 100 Hz were collected and wirelessly transmitted from 64 Ag/AgCl active electrode channels (actiCap System, MOVE System; Brain Products GmbH, Germany) placed and labeled according to a modified version of the international 10-20 system [66]. Four posterior channels (TP9, TP10, PO9, PO10) were relocated to be used as VEOG and HEOG sensors to measure baseline signals

for eye blink and eye movement artifacts. Channels FT9 and FT10 were also relocated to the AFz and FCz positions respectively for more scalp coverage, displacing the ground and reference electrodes to the top of the left and right ear respectively (Figure 2.1B). Electrolytic gel was injected between the electrodes and the scalp to maintain impedances below 20 kΩ. The 3D spatial locations of all EEG channels were digitized with a binocular camera scanner (CapTrak, Brain Products GmbH; Germany) for more detailed analyses to identify dipole source locations. An elastic mesh was placed over the EEG cap to compress the electrode cables to reduce artifacts induced by the motion of the cables. During the fMRI recording, EEG data were collected simultaneously using a custom MR-compatible EEG cap (Brain Products GmbH) with digitized channel locations (FastTrak, Polhemus; Colchester, VT) [67].

The classifier model was generated offline using custom scripts in MATLAB (Mathworks; Natick, MA), and the real-time processing was performed with multi-threaded C++ code in Visual Studio (Microsoft Corporation, Redmond, WA). For both real-time processing and offline classifier model generation, the mean of the EEG was first subtracted out. The VEOG and HEOG sensors were then used as reference channels for artifact rejection with an H^∞ filter [51]. Performance of this artifact removal method was validated by visually inspecting to ensure reduction of eye blink signals in channel FP1. Building on previous successes with detecting motor intent from low-frequency δ band in EEG [41, 44, 45, 47, 50], the cleaned signals were then band-pass filtered from 0.1-2 Hz using a second order Butterworth filter. Separate channels were then used to create a feature matrix using a 200ms window with a shift of 20ms, each row having the time shifted from $[ch_1(t-n), ..., ch_1(t), ch_2(t-n), ..., ch_2(t), ..., ch_m(t)]$, where n is the window size in samples and $m = 64$ is the total number of channels. Each row of this feature matrix was normalized such that the values ranged between 0 and 1. The resulting feature matrix was either used for determining the dimensionality reduction/classification parameters when training the model or to determine the real-time walk/stop output during the closed-loop trials. These steps are outlined in

the lower half of Figure 2.2.

2.2.5 Classification Algorithm

We applied dimensionality reduction to the feature matrix (originally 1,200 dimensions, from the product of 60 channels and 20 time lags) using Local Fisher's Discriminant Analysis (LFDA) to preserve the multimodal structure. LFDA is an extension of classical linear discriminant analysis (LDA) that uses locality-preserving projection to preserve the multimodal statistical structure within data. Unlike LDA, it does not require class distributions to be either Gaussian or unimodal and does not put an upper-bound on the number of reduced dimensions [68]. For a dataset with training samples $\mathbf{X} = \{\mathbf{x}_i\}_{i=1}^{n}$ in $\mathbb{R}^d$ (d-dimensional feature space) and class labels $y_i \in \{1, 2\}$ (for either Walk or Stop) where n is the total number of samples and n_l is the number of samples in class l, LFDA defines the *local* between-class $S^{(lb)}$ and within-class $S^{(lw)}$ scatter matrices as

$$S^{(lb)} = \frac{1}{2}\sum_{i,j=1}^{n} W_{i,j}^{(lb)}(\mathbf{x}_i - \mathbf{x}_j)(\mathbf{x}_i - \mathbf{x}_j)^T \tag{2.1}$$

and

$$S^{(lw)} = \frac{1}{2}\sum_{i,j=1}^{n} W_{i,j}^{(lw)}(\mathbf{x}_i - \mathbf{x}_j)(\mathbf{x}_i - \mathbf{x}_j)^T, \tag{2.2}$$

where $W^{(lb)}$ and $W^{(lw)}$ are $n \times n$ matrices defined as

$$W_{i,j}^{(lb)} = \begin{cases} A_{i,j}(1/n - 1/n_l), & \text{if } y_i = y_j = l \\ 1/n, & \text{if } y_i \neq y_j \end{cases} \tag{2.3}$$

and

$$W_{i,j}^{(lw)} = \begin{cases} A_{i,j}/n_l, & \text{if } y_i = y_j = l \\ 0, & \text{if } y_i \neq y_j \end{cases}, \tag{2.4}$$

with $A_i, j \in [0, 1]$ being the affinity (heat kernel) between samples $\mathbf{x}_i$ and $\mathbf{x}_j$

$$A_{i,j} = \exp(-\frac{\|\mathbf{x}_i - \mathbf{x}_j\|^2}{\gamma_i \gamma_j}), \tag{2.5}$$

based on $\gamma_i = \|\mathbf{x}_i - \mathbf{x}_i^{(k_{nn})}\|$ denotes the local scaling of data samples in the neighborhood of $\mathbf{x}_i$, and $\mathbf{x}_i^{(k_{nn})}$ is the k_{nn}-nearest neighbor of $\mathbf{x}_i$. As in LDA, Fisher's ratio is maximized but using the local scatter matrices to obtain the transformation matrix (Φ_{LFDA}) for dimensionality reduction

$$\Phi_{LFDA} = \underset{\Phi_{LFDA}}{\arg\max}\, \mathrm{tr}[(\Phi_{LFDA}^T S^{(lw)} \Phi_{LFDA})^{-1} \Phi_{LFDA}^T S^{(lb)} \Phi_{LFDA}]. \tag{2.6}$$

The reduced data was used to train a Gaussian Mixture Model (GMM) classifier to map the demarcated stopping and walking phases of the SWS cycles during the training session to the processed EEG in the reduced feature matrix. A Gaussian mixture model is a probabilistic model that assumes all data samples are generated from a mixture of a finite number of Gaussian distributions with unknown parameters, whose probability density function is defined as

$$p(\mathbf{x}) = \sum_{k=1}^{K} \alpha_k \mathcal{N}(\mathbf{x}, \mu_k, \Sigma_k), \tag{2.7}$$

where

$$\mathcal{N}(\mathbf{x}, \mu_k, \Sigma_k) = \frac{1}{(2\pi)^{d/2} |\Sigma_k|^{1/2}} \times \exp[-\frac{1}{2}(\mathbf{x} - \mu_k)^T \Sigma_k^{-1} (\mathbf{x} - \mu_k)]. \tag{2.8}$$

The parameters for the optimal number of distributions K, their centroids μ_k, their widths Σ_k, and their mixing weights α_k are determined by the expectation-maximization algorithm [50, 69]. The overall LFDA-GMM model was trained on a random subset of 70% of the training data and evaluated on 30% of the remaining data.

During the closed-loop trials, the GMM classifier would return a value for either Walk or Stop at every time sample (10ms). These binary values for filtered with an exponential moving average to prevent jittery Walk and Stop transitions. A dual-threshold Schmitt trigger with hysteresis controlled the switching between states, toggling Walk when the moving average filtered output exceed a high threshold, and reverting back to Stop only when the output dropped below a lower threshold. Threshold levels were initially fixed for the first five sessions as the classifier model accrued more data for each session, but once the model was fixed after Session 5, the threshold values were manually fine-tuned as needed at the start of each session.

2.3 Results

2.3.1 Closed-Loop BMI Decoding Accuracies

The results of closed-loop decoding for BMI control of the REX are shown first in Figure 2.3 for all subjects and each of the 9 sessions using two different metrics. The Balanced Accuracy (black diamonds) measures accuracy as a function of correctly predicted samples. Because the class distribution may be uneven, often biased towards the Stop class, a simple percentage of correctly predicted samples is insufficient. The Balanced Accuracy accounts for this by taking the average of the sensitivity (true positive rate) and specificity (true negative rate) for a better metric adjusted to a 50% chance level. The Task Completion Accuracy (blue line, yellow triangles) is the percentage of the 12 trials that were successful, i.e., subjected completed each phase of the Stop-Walk-Stop cycle without triggering the 30s fail timeout. Performance for both metrics are rather varied across subjects with no consistent trends; S1 and S3 did show general improvement from the first to the last sessions, both achieving a Task Completion Accuracy of 100% for Session 9 but starting close to 0 for Session 1. S1 in particular showed a notable trend in improvement in performance once the

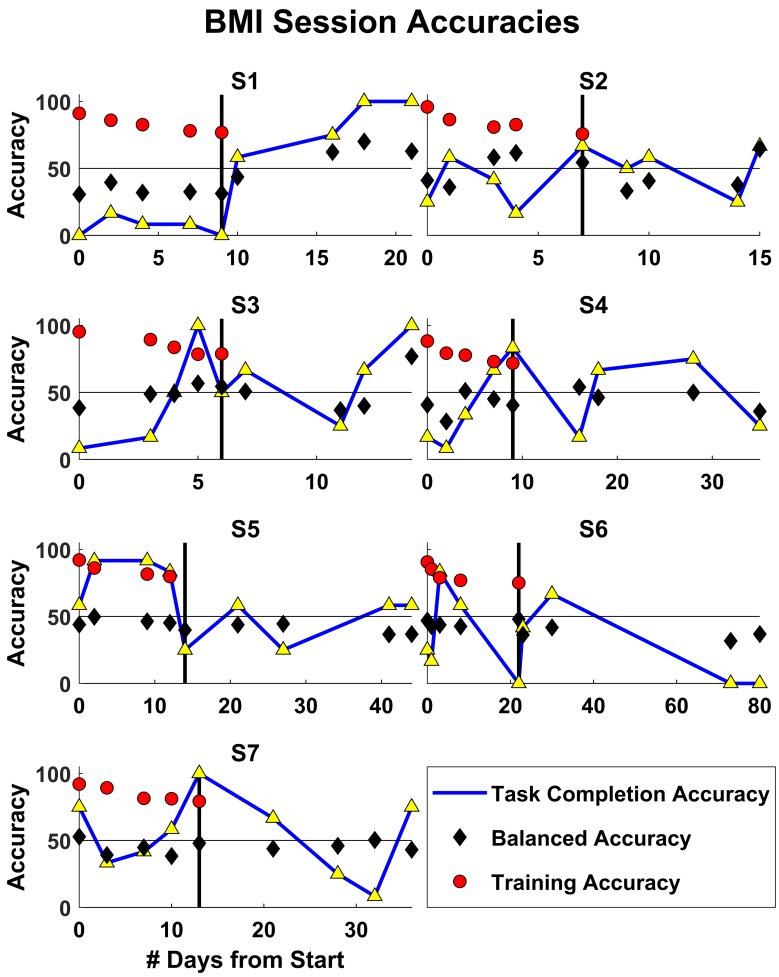

Figure 2.3: BMI accuracies for all subjects and their 9 sessions: Task Completion Accuracy is the percentage of the 12 trials successfully completed; Balanced Accuracy is the mean of sensitivity and specificity of the classified samples; Training Accuracy is the cross-validation classification accuracy during model training.

decoder parameters were fixed after Session 4. Most other subjects performed at or around chance except for a few sparse sessions of good accuracy. Because of this variability, some of the future analysis will selectively focus on S1 as good-performing subject that showed improvement across session and S2 as a poor-performing subject that was consistently at chance. The average trial accuracy for the final session for all subjects was 60.7%, compared to 29.8% for the Session 1 average, while the average Session 9 Balanced Accuracy was only 51.0%.

The cross-validation training accuracies (red circles) from calibrating the decoder

model are also shown for the first 5 sessions (4 for the case of S5); the vertical black line demarcates the early sessions with the adaptive decoder and the late sessions with the fixed decoder. As is common in machine learning, these were very high (>90% accuracy) relative to the closed-loop accuracies. As the size of the training dataset grew with each session, the training accuracy decreased slightly as the model began to generalize for inter-session signal variability. Note that the time scales are different for each subject, as sessions were scheduled according to each subjects' availability; S6 in particular was not available for a 43 day period and overall took 81 days to complete the protocol, in contrast to S1, S2, and S3 who efficiently completed the 9 sessions within 3 weeks.

The BMI performances of the individual trials within each session are shown in Figure 2.4. The first four sessions can be described as a familiarization period with the BMI as both the model and the subject are adapting, and are thus omitted from this plot. Each trace shows the cumulative average of the classification accuracy for the duration of each trial. All traces start at 100% and either decay with misclassifications or rise towards convergence with correctly classified samples. The traces are also color-coded (red for Stop, green for Walk) for each phase of the SWS cycle. Traces for successful trials go through the green and second red phases, while fail trials finish prematurely in either the green or first red phase and/or end on a negative slope. The final classification accuracy for the trial is denoted with a black circle at the end of each trace while the Balanced Accuracy for the session (same as from Figure 2.3) is marked with a star. Session 9 for both S1 and S3 show excellent BMI performance with all 12 trials successfully going through the full SWS cycle, not ending on a prolonged negative slope (otherwise indicating a triggered 30s fail count timeout), and very efficiently completing most trials in about a minute or less.

Each BMI session concluded with a pair of 6 Minute Tests, in which the subjects were asked to maintain either a continuous Stop or a continuous Walk for a duration

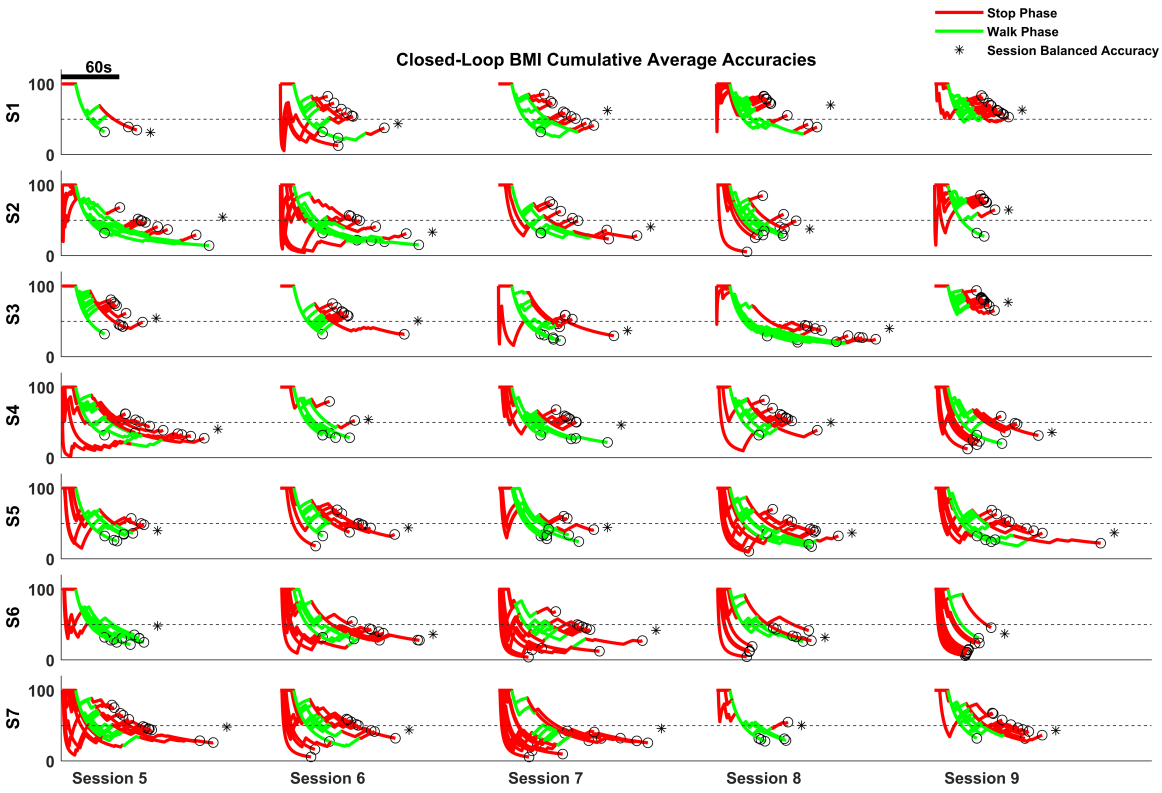

Figure 2.4: Individual closed-loop BMI accuracies for all subjects for sessions 5-9. Accuracy is shown as the cumulative time average for the duration of the trial, color-coded for each phase of the SWS cycle, with the overall trial accuracy as a black circle at the end of each trace, and the session balanced accuracy as a black star.

of 6 minutes. Figure 2.5 shows the performance for these tests. The top plot shows individual accuracies as a percentage of correctly classified samples for the Walk and Stop tests separately in each of the 9 sessions. To better relate this to the traditional 6 Minute Walk Test used in physical rehabilitation [65], we assess the total distance covered for the 6 minute period by identifying the number of correctly predicted Walk samples during the Walk Test and subtracting the number of incorrectly predicted Walk samples during the Stop Test; this normalized difference is shown in the bottom plot of Figure 2.5. Difference scores of 0 might occur if the decoder is completely biased towards one state, and negative scores are possible if more walking occurs during the Stop test. Consistent with the previous decoding results, S1 and S3 again have high accuracies (median scores of 0.60 and 0.88 respectively) demonstrating

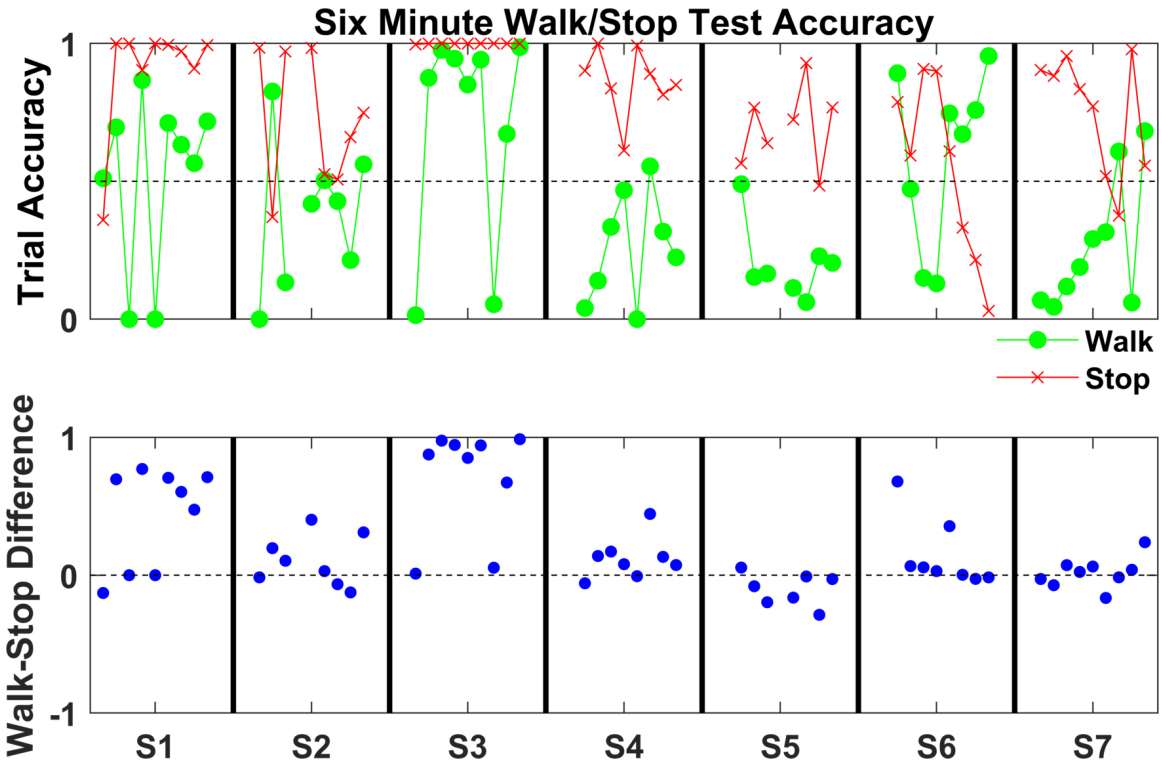

Figure 2.5: Decoding accuracies for the closed loop 6 Minute Walk and Stop Tests. The top plot shows individual classification accuracies for the Walk and Stop tests separately as percentage of correctly classified samples. The bottom plot shows the normalized difference in distance covered between the Walk and Stop tests.

strong ability to maintain a consistent state.

2.3.2 EEG Signal Analysis

Given the variability in BMI performance both among subjects and sessions, we take a closer look into what might be the causes by analyzing the quality of the EEG signals as inputs to the decoder. The EEG impedance is a common variable that can greatly influence signal quality during an experiment; as described in the methods, impedance values were maintained as low as possible to ensure good conductivity. Figure 2.6 shows the electrode impedances before and after each session for all subjects. Values less than 10 kΩ (within the green portion of the spectrum) are ideal for EEG experiments, as is shown to be the case for most sessions and subjects. Both

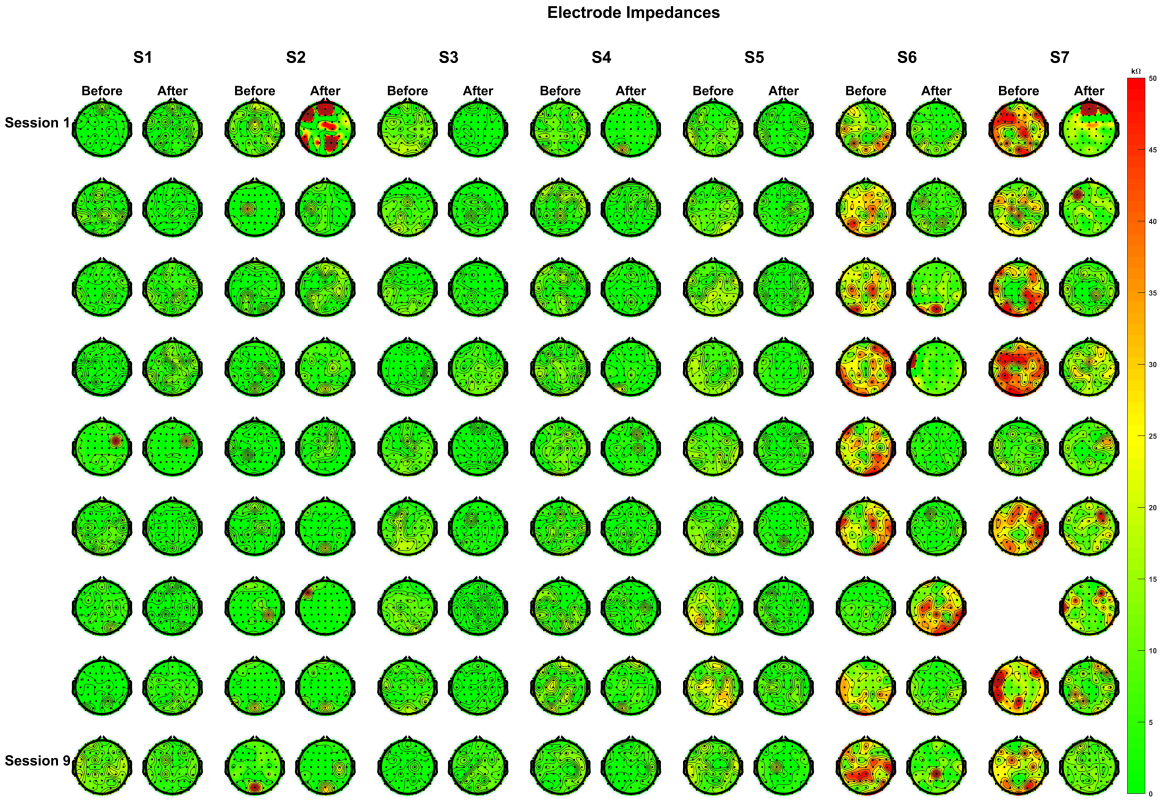

Figure 2.6: EEG electrode impedances at the start and end of each session for all subjects. Most sessions began with acceptably low impedance values (<10 kΩ) although some ended with a low number of channels losing their conductivity by the end.

S6 and S7 had numerous sessions above this range, although most of the impedance values did settle by the end of the session. Still, even individual channels with high impedances can cause irregularities that might disrupt the decoder's performance. Impedance values for S7's Session 7 were not saved at the beginning of the trial due to a technical error.

Besides impedance values, we looked into a number of other metrics to discern any underlying features that may explain why some trials were successful with the BMI and others weren't. While our closed-loop decoding algorithm used simple spectrotemporal features (i.e., δ band amplitudes), we assessed more complex features of

the EEG trial data to distinguish between the successful and failed trials. The Shannon's entropy, spectral edge frequency, dyadic entropy, fractal dimension, Hjorth parameters (the normalized slope descriptors: activity, mobility, and complexity) [70], and statistical moments (skewness and kurtosis) were calculated for each channel and averaged, as these were features that have been shown successful in detecting EEG irregularities during seizure detection [71]. Figure 2.7 shows these features evaluated for each trial and color-coded based on the trial's outcome (green circle for success, red x for failure). Each feature's median value for all trials are shown on the right side of each plot in black. Not much separability is apparent between the two conditions for any of these features, but the median values for both the fractal dimension and mobility show the least overlap. The fractal dimension is a measure of a signal's complexity and self-similarity in time [72, 73], and mobility represents an estimate of the mean frequency, defined by the ratio of the standard deviations of the signal's derivative and the signal itself [70]. Figure 2.8 takes a closer look at these two features, in addition to skewness as a contrast, for each subject individually, illustrating the distributions as raincloud plots (probability density functions as the clouds and a scatter of the individual data points as the rain) [74]. A two-sided Wilcoxon rank sum test was performed for each of these distributions, verifying statistical difference in the distributions for both the fractal dimension and mobility measures at the $p < 0.05$ significance level for the group subject data as well as individually for S1 and S7.

2.3.3 Feature Matrix Analysis and Clustering

Another way we evaluate the BMI decoder post hoc is by looking at the EEG feature matrix data just as it's going into the classification algorithm. The feature vector for each classification sample consisted of 200ms windows of δ EEG amplitudes concatenated for all channels. The averaged windows for each channel are visualized for two subjects, S1 as the best performing subject and S2 as a subject that performed

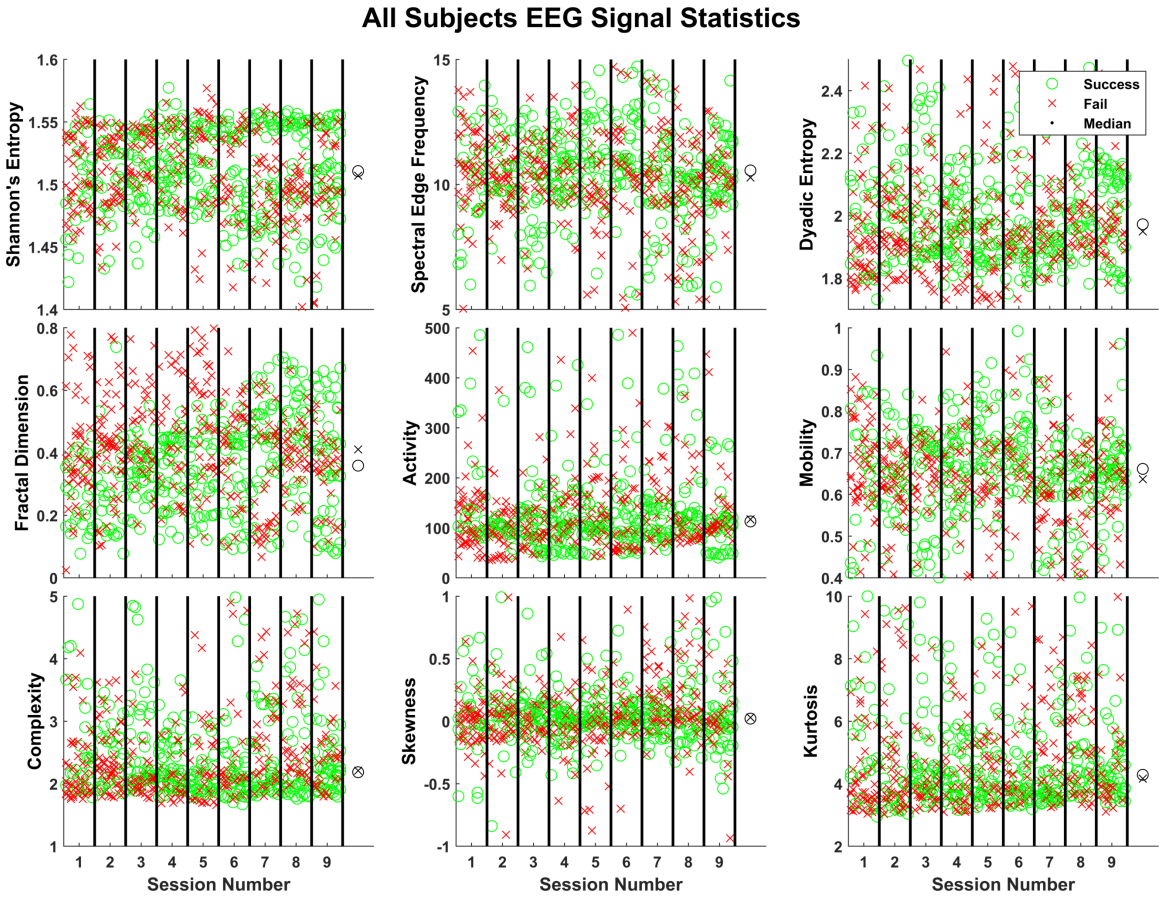

Figure 2.7: Various nonlinear and complex EEG features (averaged across channels) were calculated for each of the closed-loop trials to discern indicators of successful or failed BMI performance. Each feature is plotted across the 12 trials for the 9 sessions (separated by vertical lines), with the overall median plotted in black.

mostly at chance, in Figures 2.9 and 2.10 respectively. Some channels are removed for the purposes of clarity. The scalp maps are sorted in a confusion matrix according to the BMI classification of each feature vector: true positives (TP) vs. false positives (FP) vs. true negatives (TN) vs. false negatives (FN). Each trace represents the averaged feature window for a whole session, and are color-coded in order of a yellow-orange-red-black color gradient (Session 1 as yellow and Session 9 as black). A thick blue trace shows the overall average across all sessions. For both subjects, the dynamic range of values is very small, with the scale bar set to limits from 0.485 to 0.515 μV. As each feature vector was normalized to the range [0 1], the collective average seems

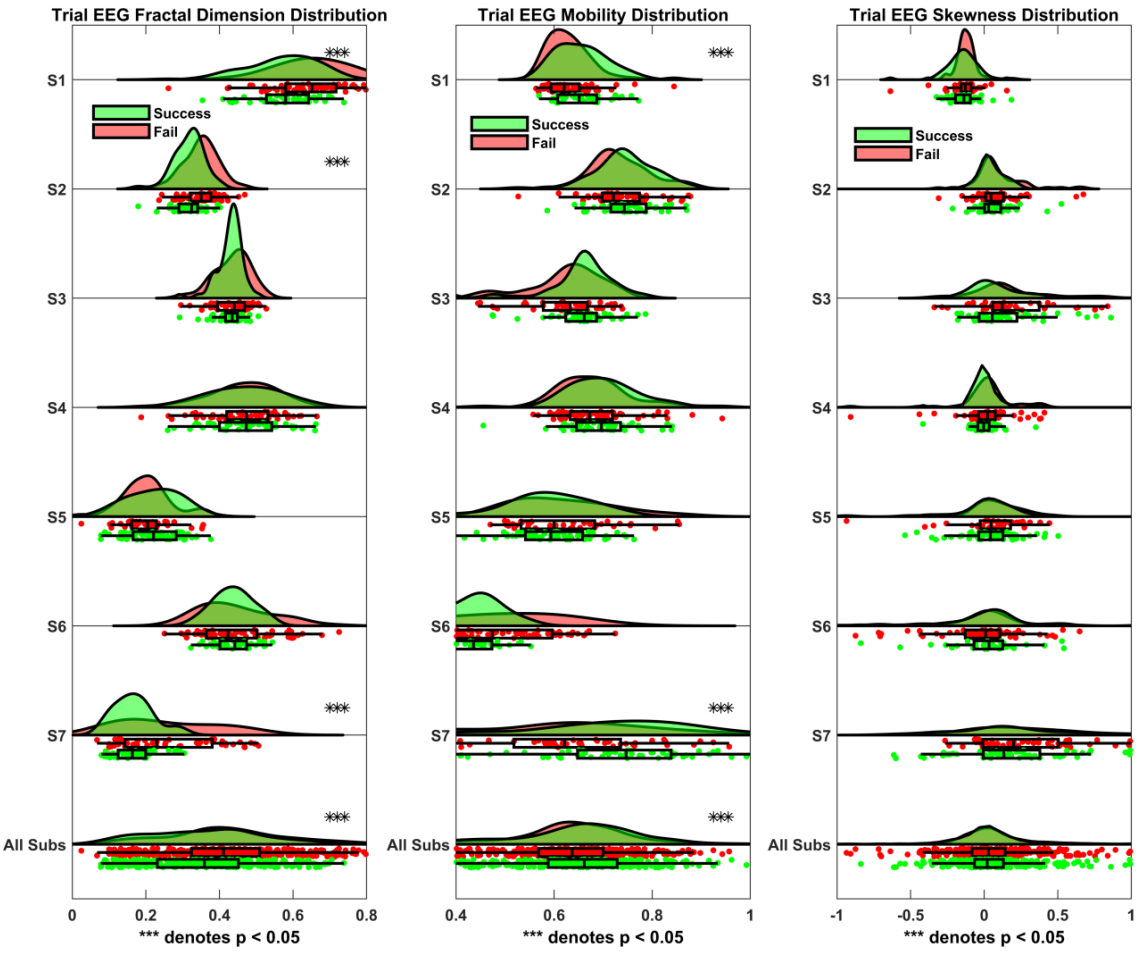

Figure 2.8: Raincloud plots for fractal dimension, mobility, and skewness showing their distribution (probability density function and boxplots together) for successful and failed trials, separated by subject. *** denotes statistically significant different distributions ($p < 0.05$) based on a two-sided Wilcoxon rank sum test.

to converge to the midpoint of this range. Although likely not significant, the TP and FP scalp maps show more traces deviating farther from the mean, suggesting that the decoder was guessing Walk feature vectors with larger variances.

We also explored if the issue might have been with limitations in the Gaussian Mixture Model classifier failing to find any separability in the feature matrix. Did the GMM do the best it could do with the feature matrix it was given, or could another classifier improve upon these results? The same closed-loop data was passed through three other unsupervised clustering algorithms (k-means, hierarchical, and spectral

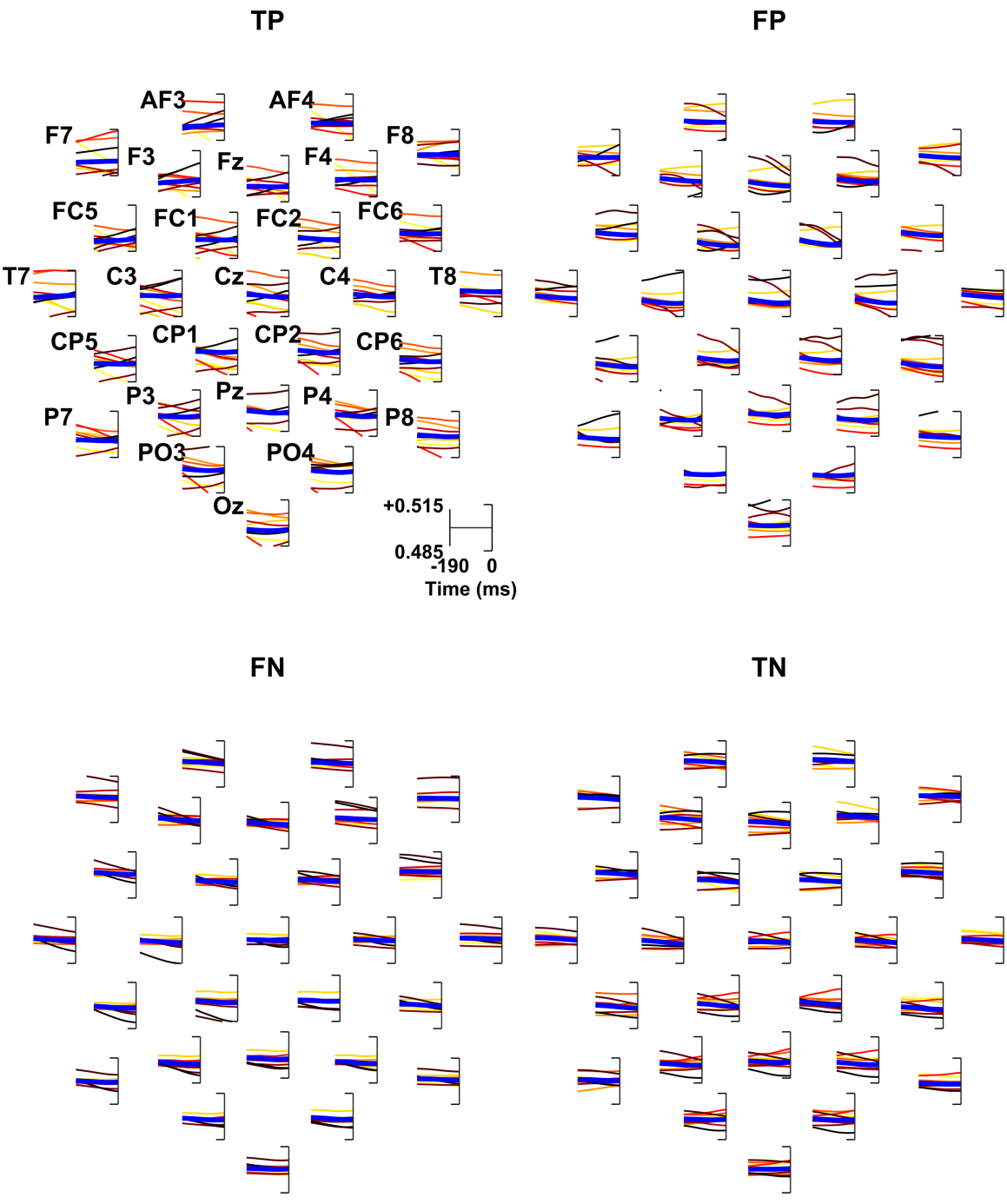

Figure 2.9: Average EEG features for subject S1 (best performing subject) on scalp maps, sorted by true/false positive/negative classifications. Each trace represents the session-averaged window of δ amplitudes, ordered by a yellow-red-black gradient (Session 1 yellow, Session 9 black) with the overall average in blue.

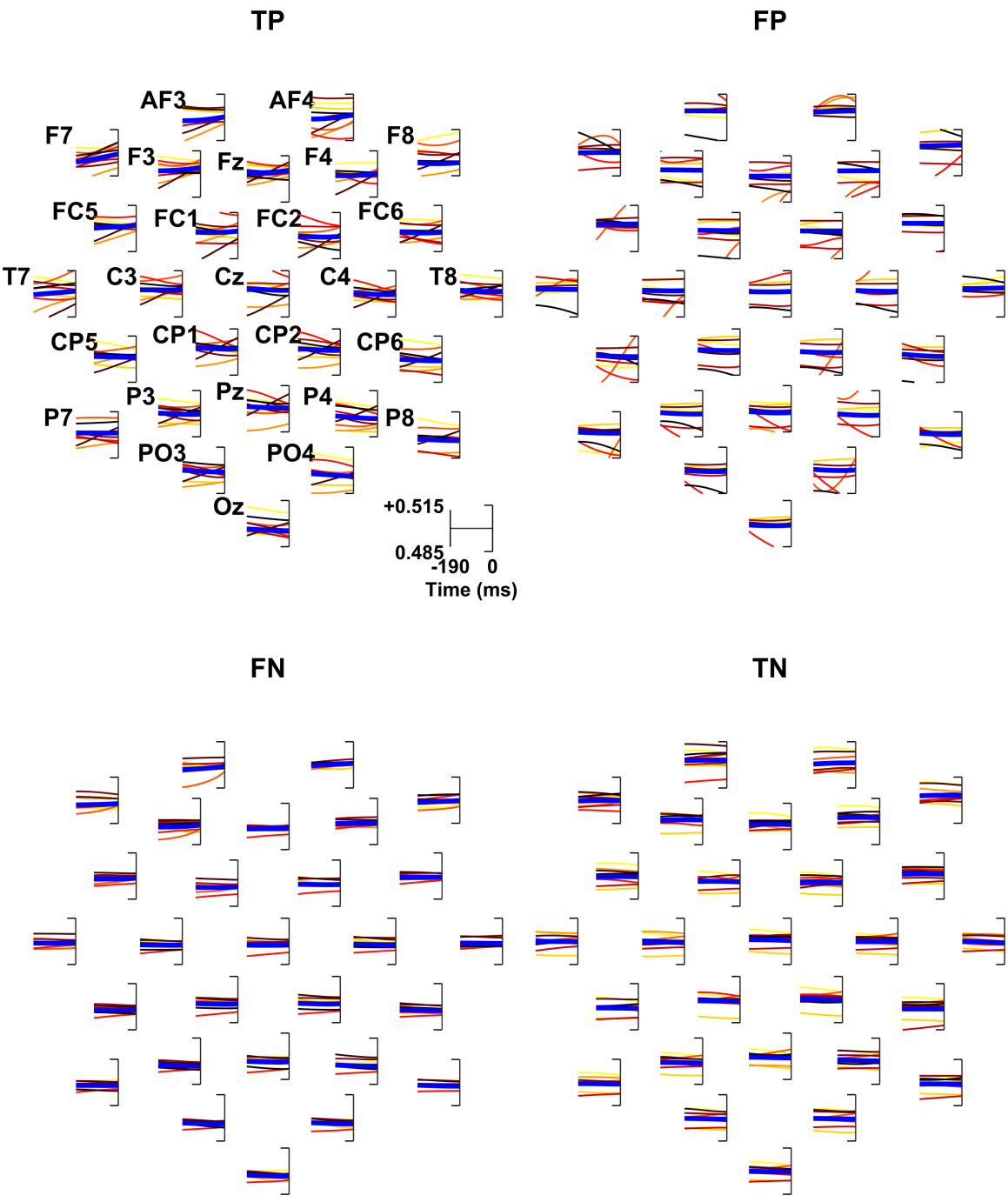

Figure 2.10: Average EEG features for subject S2 (worst performing subject) on scalp maps, sorted by true/false positive/negative classifications. Each trace represents the session-averaged window of δ amplitudes, ordered by a yellow-red-black gradient (Session 1 yellow, Session 9 black) with the overall average in blue.

clustering) with two different distance metrics (Euclidean and cosine). Each trial was clustered independently and accuracies (assigned based on the known class labels from the trial) were averaged for the whole session. Figure 2.11 shows the clustering accuracies for the three different algorithms and the two distance metrics for each subject, both on the normalized data (as seen by the GMM classifier; top plot) and the data before normalization (bottom). Hierarchical and spectral clustering both performed well above chance, both performing with average overall accuracies of 70.1% using the cosine distance. Using the un-normalized data rendered the cosine distance ineffective for the hierarchical algorithm, but it did improve average accuracies for the Euclidean distance from 59.9% to 71.7%, even achieving accuracies as high as 89.1%. The k-means classifier performed at chance for most of the sessions. Curiously, the subjects who had the highest offline accuracies, S4 and S6, both performed near chance levels during the closed-loop trials (Figure 2.3).

2.4 Discussion

2.4.1 Variability in BMI Performance Among Subjects

The purpose of this study was to develop a brain-machine interface for the control of a walking exoskeleton and to evaluate the performance of users over an extended period of 9 sessions. While the closed-loop decoding accuracies were overall rather varied across subjects, 5 of the 7 subjects that completed the protocol were able to successfully complete more than half of their trials in the last session. Two subjects in particular, S1 and S3, performed demonstrably better than the others, both completing 100% of their final session's trials and with respective median 6MWT scores of 0.60 and 0.83 (on a scale from -1 to 1). In post-session debriefing, both individuals were confident in their ability to control the REX's gait at will by the end.

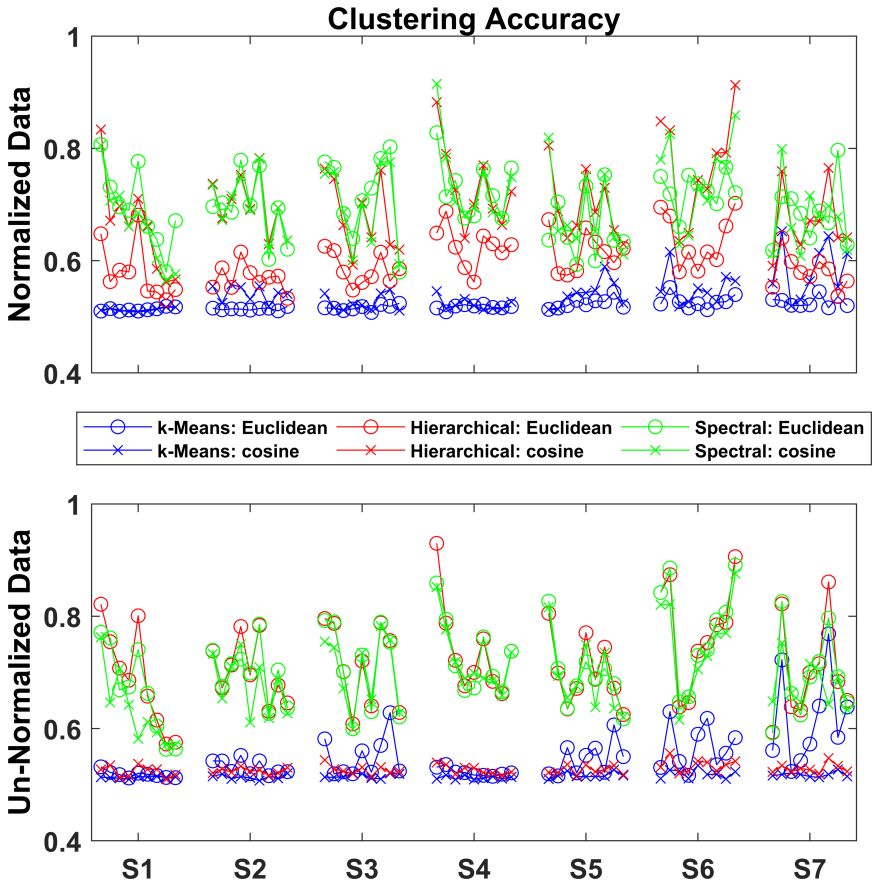

Figure 2.11: Accuracies from offline unsupervised clustering of the feature matrix of the closed-loop EEG data.

The exemplary performance of these two subjects demonstrates the feasibility of BMI control for at least certain individuals, suggesting that some people may be more adept BMI performers than others. Quantitative attempts to explain the discrepancy in subjects' performances were not conclusive (Figures 2.7, 2.8) at finding features and statistical measures that could predict trial success. Certain features, such as the fractal dimension and mobility, had statistically different distributions when evaluated on the EEG from successful and failed trials separately, but these patterns were not consistent across all subjects (or even on the well-performing subjects together). Other qualitative factors did seem to have an impact on a subject's daily performance. Long delays between sessions (most notably a month long hiatus between S6's seventh

and eighth sessions) negatively impacted performance as the subject had to refamiliarize themselves with the BMI. Anecdotally, mental well-being may have also played a role; some subjects admitted participating in the experiments while being stressed with coursework and other personal issues, and S3 reported not having slept well the night before his seventh session, an outlier in an otherwise positive trend. While BMI protocols remain novel, it would seem that attaining strong performances would be contingent upon the subjects' mental well-being.

2.4.2 Comparisons with other Exoskeleton BMI Studies

This study was unique among other noninvasive BMI studies to control an exoskeleton in that it took place over many sessions over several weeks to develop a generalizable decoding model. One study did test their subjects over 5 sessions on consecutive days [54], but a new model was trained each day and no meaningful differences were reported across sessions, suggesting the intervals were too short for inducing any plasticity. Their testing protocol also involved trials of decoding SWS cycles, but of fixed time lengths and the robot was disabled during the Stop cycles eliminating the possibility of false positive movements; for two subjects, they were able to achieve mean accuracies of 73.4% using a SVM on ERD features between 6-35 Hz. A 2013 study by Do et al. [30] was the earliest but most similar to our protocol in that they focused on extracting KI to switch between alternating prolonged Stop and Walk cycles. They report using an able-bodied and a SCI subject over 5 sessions, but these sessions are all on the same day and more akin to the trial blocks (sets of 4 trials) used in our study. They evaluated performance by calculating the cross-correlation of the cue signal with the exoskeleton state signal (average of 0.812 for the two subjects), and showed rather robust control with ERD features from 0-40 Hz through classwise PCA dimensionality reduction and a Naive Bayes classifier. However, both of their subjects were non-naive BMI users and experienced with KI,

which may explain their quickness to learn to control the exoskeleton.

Two other studies used a BMI as a "brain-switch" [75] attempting to only detect a single instance of gait intention to trigger walking in the exoskeleton [52, 55]. Both studies used protocols with trials instructing subjects to attempt to walk following a cue after a period of rest, detecting for the readiness potential (i.e., motor-related cortical potential) to trigger a gait cycle for the trial. Lopez-Larraz et al. [52] tested a mixed group of 3 able-bodied and 4 SCI subjects, using both low frequency δ and ERD features between 7-25 Hz in a sparse discriminant analysis for 84% and 78% accuracies among healthy and SCI patients respectively. Liu et al. [55] used a slightly different approach by trying to evoke hand motor imagery to scan a broader cortical representation, attaining 69% detection in 6 able-bodied subjects with canonical variant analysis and Naive Bayes. Specifics in the study by Donati et al. [29] regarding the BMI protocol and decoding performance were not provided in enough detail for commentary here. Other studies that have been carried out using BMIs for classifying more than 2 states are not used for comparison here, but are discussed in Section 2.1 and detailed in Table 2.1 [49, 57, 58, 60].

2.4.3 Examining Alternative Features and Classifiers

The feature matrix as visualized in Figures 2.9 and 2.10 showed minimal differences between the Walk and Stop conditions, even for subject S1 for whom decoding was mostly successful. The grand average across all subjects (not shown) showed even fewer changes within the already small amplitude scale. The choice of 200ms windows was perhaps too small compared to the previously discussed studies [30, 52, 54, 55], which employed window sizes ranging from 750ms to 2s to capture the relevant features. Our use of a 200ms might have missed the necessary feature for triggering the BMI, but extending the window length will come at the expense of higher dimensionality and computation times, unless trade-offs are made that sacrifice channels

or time resolution. Alternatively, the frequency bandwidth can also be expanded to include signals from the higher end of the frequency spectrum. Our rationale for using a range of 0.1-2 Hz was based on some of our previous work that showed strong correlations in this range with angular kinematics of gait [41, 44, 46, 47, 48, 76, 77], and while they were similarly used to detect readiness potentials in [52, 55], they were still used in conjunction with ERD features at higher frequency ranges, or ERD features were used exclusively [30, 54].

Other clustering algorithms, particularly the hierarchical and spectral methods, showed improved ability to separate the data than the GMM used in real-time. Moreover, the GMM parameters were optimized during the model training phase, while only the type of distance metric was varied for the other clustering methods. Interestingly, the newer algorithms performed best for S4 and S6, who were among the poorest performers for closed-loop control. These higher clustering accuracies should be taken with caution though, since they may not necessarily translate well to closed-loop decoding. It is possible that the good clustering may be a result of overfitting from the algorithm having a full distance matrix for every sample in the closed-loop set, and that introducing unseen data in real-time may not be as successful. Selecting a new type of decoding scheme or even alternative features is naturally difficult because you can only judge based on offline performance on training data, which showed consistently high accuracies even with the GMM (red circles in Figure 2.3).

2.4.4 Limitations

Although the results presented in this study show promise, there are a number of factors in the experimental protocol that add difficulty to the interpretation of the results and potentially hinder the efficacy of the BMI system. The REX exoskeleton itself has hardware limitations that insert an inherent time delay when executing movement commands. Since the REX is meant to be fully stable, it has to complete

a whole gait cycle before stopping, resulting in a slower time response to switch states than the BMI output. This ensured stability does result in a slightly unnatural walking motion that may not fully match the users' expectation when trying to elicit kinesthetic motor imagery if imagining normal walking without an exoskeleton.

Negative feedback from the closed-loop nature of the experiment can also physically affect the subject during misclassifications. Some studies circumvent this issue by suppressing any false positive movements [52, 54], but during our misclassifications, the REX may start walking when the subject is trying to maintain an idle state and the unexpected disruption of the movement can negatively affect the subject's focus and BMI performance. Reduction of these false classifications could possibly be done with prior BMI training with KI itself (without an exoskeleton) [31, 55] and providing either visual or tactile feedback to guide the subject that their imagery attempts are being decoded in the right direction [29]. The drawback here is that the subject may switch their focus from the KI of their imagined movements to instead guiding the visual/tactile feedback cue. Even the strategy of using kinesthetic imagery for the BMI requires effort and for subjects to maintain focus [55], also rendering the subject susceptible to occasional distractions, since experiments were carried out in a long public hallway. The motors of the REX are also rather loud and the noise itself can be both a distraction or create an unwanted auditory response in the EEG that could interfere with the BMI decoding.

We were unable to reliably analyze the EEG signals during the trials due to the inconsistent timing of imagery cues and the concurrent feedback of the REX. The extracted epochs would have to be categorized as either true/false positive/negative states (as in Figures 2.9 and 2.10) and would ultimately be of either insufficient length or number (only 200ms in length in the reported figures). As is usually the case in EEG studies, a legitimate concern is the possibility of noise and artifacts contaminating the data. Motion artifacts are typically minimal during walking at

speeds as slow as the REX [78], but more robust offline artifact cleaning methods including Artifact Subspace Reconstruction [79, 80] and Independent Component Analysis [81, 82] will be employed in the following chapter. And as is usually the case, this experiment certainly could have benefited from having more subjects and more data per subject. The full protocol was already a major time commitment for the subjects as is, and it would be unreasonable to ask them to commit to even more trials and/or sessions. We were also limited in having to prematurely stop subject recruitment due to the ongoing COVID-19 pandemic.

2.5 Conclusions

In this study, a brain-machine interface was designed to allow able-bodied subjects to initiate walking in a robotic lower-limb exoskeleton. Subjects were trained across 9 sessions over several weeks to track improvement and other changes in performance. Our results showed mixed performance among the full cohort of subjects but very robust decoding in at least 2 participants, demonstrating that kinesthetic motor imagery, measured noninvasively using EEG, can be used to switch between walking and stopping states when controlling an exoskeleton. This work contributes to the body of literature by benchmarking the performance of the LFDA-GMM classifier used here, the windowed δ band features, and a longitudinal protocol that accrues multi-session training data for a more generalizable decoder. While the ultimate goal of this research is to determine the viability of a BMI to restore motion to the paralyzed population, our use of able-bodied subjects serves as an initial proof-of-concept that subjects can cognitively control a robotic device for mobility. Future steps that could further the results presented here would be to enroll paralyzed patients with spinal cord injury, evaluating alternative features and more advanced classifiers, and incorporating tactile feedback or electrical stimulation as a means to improve decoding performance and cortical plasticity.

Chapter 3

The Neural Correlates of Kinesthetic Motor Imagery of Gait during Brain-Machine Interface Training

3.1 Introduction

Kinesthetic motor imagery (KI) is the mental simulation of movement that requires a sense of feeling and perception of the muscles contracting and stretching in accordance with the imagined motion [83, 84, 85]. This internalized embodiment of the movement is in contrast to visual motor imagery (VI), which only requires mentally seeing (but not feeling) the motion from either a first- or third-person point of view [83]. Even without eliciting movement or electromyographic (EMG) response, KI can still induce physiological responses including increases in heart rate, blood pressure, and respiration [83, 86, 87]. Moreover, KI can be useful in motor imagery training to improve voluntary muscle strength [84, 86, 88, 89], motor performance [90, 91], motor sequencing [92], aiming [93], and timing [94] in either sports [95] or physical rehabilitation applications [96, 97, 98], with comparable training curves to training with motor execution [92]. KI training can also improve the strength of EMG and movement-related cortical potentials (MRCPs) [84], and even induce stronger plasticity when used in conjunction with functional electrical stimulation (FES) [99, 100, 101].

Kinesthetic imagery involves similar overlapping yet distinct neural structures

when compared to both visual imagery and actual movement. Imaging studies using fMRI show that both KI and executed movement activate regions in the premotor and parietal cortices, supplementary motor area (SMA), cingulate gyrus, the putamen and caudate nucleus of the basal ganglia, and cerebellum [54, 83, 84, 102, 103]. The literature is somewhat inconsistent in reporting primary motor cortex (M1) activation during motor imagery, but it is found more often during KI (albeit decreased) rather than VI [102, 104, 105, 106], which otherwise sees more activation in occipital visual areas such as primary visual cortex, cuneus, and prestriate cortex [83, 105]. Both SMA (superior and medial frontal cortices and dorsolateral prefrontal cortex) and basal ganglia are more prominent in KI than real movement, suggesting that imagery involves recruitment of both a fronto-parietal network and subcortical and cerebellar regions [105, 107, 108, 109]. The parietal cortex is crucial in the generation of mental images [110, 111] and sensory-visual representation [84], whereas the cerebellum regulates balance control and locomotor speed [105]. Guillot et al. also identified a ventral premotor system corresponding to mirror neurons that is active during KI, responding to perception of kinesthetic feedback [83]. Neuroimaging studies that looked specifically at the imagery during walking identified representation for foot movements located within the interhemispheric fissure of sensorimotor cortex [112], general activation of prefrontal cortex (PFC), SMA, cingulate cortex, basal ganglia, and brainstem [105, 107, 113], with deactivation of multisensory vestibular cortical areas [114]. The integration of these numerous structures makes sense as gait necessitates controlled balance between automatic and cognitive controlled processes [113, 115]. Hamacher et al. provides a comprehensive review of studies identifying walking-related brain activity [116].

Other studies have shown how KI can be detected and measured in cortical potentials using electroencephalography (EEG). The most consistent finding is the μ event-related desynchronization (ERD), i.e., the decrease in spectral power within the 7-13 Hz frequency band [54, 104, 112, 117], although this power suppression has also

been seen in a range as wide as 6-35 Hz [117] spanning the high θ through β frequencies. Electrode channels that see motor imagery-related ERD are usually positioned over the vertex and bilaterally over central motor areas with surrounding areas seeing the opposite effect in event-related synchronization (ERS) as a focal ERD/surround ERS effect [104, 117, 118, 119]. Tariq et al. also reports a high β rebound (ERS) at the end of the KI period [112]. These distinct neural patterns within EEG suggest that KI can be used as a "brain switch" to control a brain-machine interface (BMI) [75, 120], with detectable state differences even in paralyzed populations without the ability to move [29, 31]. The ability to elicit strong KI responses can also be identified through questionnaires [121], which may be a useful tool to screen candidates for successful BMI performance [83]. In addition to ERD and ERS features, cortical activation during motor imagery distributes through the sensorimotor cortex as EEG sensorimotor rhythms (SMRs) that produce stable features over time with latencies lasting several seconds; MRCPs are usually associated with motor execution, but can be more easily detected during imagery as a peak preceding movement onset [55]. Several BMI studies have used features derived from kinesthetic imagery to detect gait intent to control exoskeletons [29, 30, 31, 55, 112]. The classification of the BMI performances are discussed in detail in Chapter 2. Despite some variability among subjects within and across the studies [30, 104], feature extraction for walking KI generally involved electrodes overlying PFC, SMA, and sensorimotor areas for the legs and arms.

One key question related to the use of KI in brain-machine interfaces is how longitudinal training might effect KI responses. Most of the previously discussed studies conducted limited or single-session BMI training without allowing for observation of long term effects or changes. One exception to this was a study by Donati et al. [29], which saw extensive training yield a significant increase in amplitude in the event-related potential (ERP) and an increase in the number of localized dipole sources clustered near the leg representation in motor cortex in SCI patients. These effects

are however confounded by the multiple facets of the training paradigm, which incorporated physical rehabilitation in a body-weight support system and an exoskeleton, virtual reality KI training with tactile feedback, as well as BMI control of a virtual and physical exoskeleton. The purpose of the current study is to investigate the neural correlates underlying the KI of walking within the context of a multi-session BMI training paradigm with an exoskeleton. We measure EEG responses during the course of the training with a final fMRI recording upon completion of nine BMI sessions to observe changes in the spatial and temporal dynamics that may indicate BMI-induced neuroplasticity.

3.2 Methods

The neural data analyzed for this experiment are from the same overarching dataset with the subject pool and behavioral task as described earlier in Chapter 2, with the subject demographic information included in Table 2.2. All subjects had provided written informed consent and all experiments were approved by the Institutional Review Board of the University of Houston.

3.2.1 Experiment Setup and Protocol

Behavioral Task

Seven able-bodied subjects (four males & three females, ages 20-30) were recruited in this study to elicit their kinesthetic imagery while walking in the REX lower-limb robotic exoskeleton (Rex Bionics Ltd; Auckland, NZ). Over nine sessions, scheduled approximately 2-3 times per week per the subjects' availability, EEG data were collected from the subjects walking in the REX for six stop-walk-stop (SWS) cycles with the REX in full control of the subjects' legs (Figure 2.1a). An auditory beep cued

the start of each stop-to-walk and walk-to-stop transition. Subjects were instructed to elicit their KI during the walk phases in accordance with the movement of the exoskeleton. Each session lasted approximately five minutes and the collected data was used to train the closed-loop BMI decoder as described in Chapter 2.

EEG Data Acquisition

EEG data sampled at 100 Hz were collected and wirelessly transmitted from 64 Ag/AgCl active electrode channels (actiCap System, MOVE System; Brian Products GmbH, Germany) placed and labeled according to a modified version of the international 10-20 system [66]. Four posterior channels (TP9, TP10, PO9, PO10) were relocated to be used as VEOG and HEOG sensors to measure reference templates for eye blink and eye movement artifacts. Channels FT9 and FT10 were also relocated to the AFz and FCz positions respectively for better scalp coverage over the motor cortex, displacing the ground and reference electrodes to the top of the left and right ear respectively (Figure 2.1b). Electrolytic gel was injected between the electrodes and the scalp to maintain impedances below 20 kΩ. The 3D spatial locations of all EEG channels were digitized with a binocular camera scanner (CapTrak, Brain Products GmbH; Germany) for more detailed analyses to identify dipole source locations. An elastic mesh was also placed over the EEG cap to compress the electrode cables to reduce artifacts induced by the motion of the cables.

MRI Data Acquisition

After the nine sessions, subjects underwent an MRI scan (Philips Ingenia 3.0T, Koninklijke Philips N.V.; Netherlands) for both a T1-weighted structural scan and a fMRI recording. For the functional scans, subjects watched a 10-minute video of themselves walking in the REX for 11 SWS cycles filmed from the subject's first person view as if they were looking down at their own legs in the exoskeleton. While

watching the video in the scanner, subjects were again asked to try to evoke their KI in accordance with the exoskeleton's movements. EEG data were also collected during the MRI scan using a custom MR-compatible EEG cap (Brain Products GmbH) with digitized channel locations (FastTrak, Polhemus; Colchester, VT) [67]. Due to a data collection hiatus during the COVID-19 pandemic, subjects S6 and S7 did not undergo the MRI scan.

Motor Imagery Questionnaire

Subjects were asked to complete the Motor Imagery Questionnaire - Revised Second version (MIQ-RS) [121] as a post-experiment follow-up survey. The MIQ-RS is an established assessment for obtaining a quantitative measure of a subject's movement imagery ability in both visual and kinesthetic domains. Such questionnaires have shown to be a useful tool to screen candidates for successful BMI performance [83]. Subjects completed the questionnaire independently with a guided online instructional video. The average score across the 14 questions in the MIQ-RS are reported in Table 2.2. No response is given for subject S6 who did not return the completed questionnaire.

3.2.2 Offline EEG Signal Processing

The collected EEG data underwent a rigorous offline processing pipeline to remove physiological and non-physiological artifacts. All analysis steps were performed using custom code scripts written in MATLAB (Mathworks; Natick, MA) with extra functions from the open source toolboxes EEGLAB [122] and Fieldtrip [123]. The overview of the processing steps are shown in the flowchart in Figure 2.2.

The EEG data were first high-pass filtered at 0.1 Hz with a fourth order Butterworth filter to remove baseline drift. Electrical line noise was removed using the

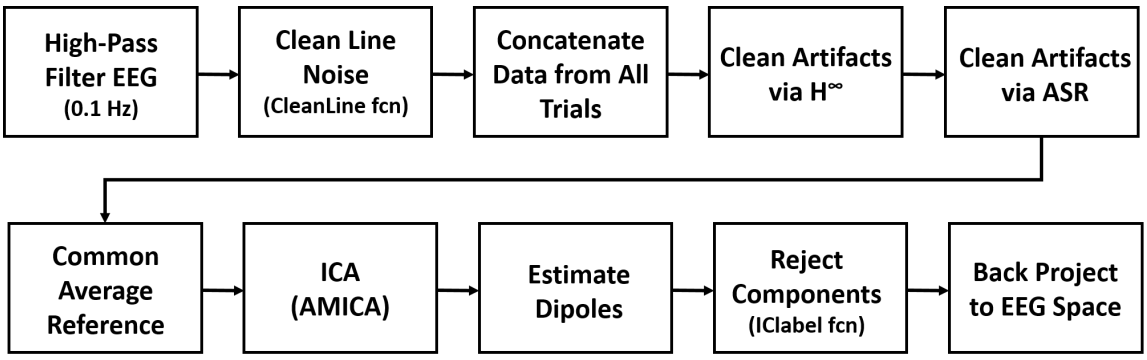

Figure 3.1: Flowchart for offline processing steps of the EEG during kinesthetic imagery of walk and stop while walking in the REX exoskeleton.

CleanLine plugin, which uses a sliding window to adaptively estimate the sine wave amplitude for subtraction. The dataset was then concatenated with the remaining EEG data from the closed-loop BMI trials to ensure sufficient length downstream for independent component analysis (ICA); these would be separated out later. Next, the VEOG and HEOG sensors were used as reference channels for artifact rejection with an H^{∞} filter, which has been shown to be especially effective in mitigating ocular artifacts [51]. Afterwards artifact subspace reconstruction (ASR) [79, 80] was used to remove noisy bursts from the data using a channel correlation criterion of 0.8 and a burst criterion of 10 standard deviations to remove corrupted subspaces. If necessary, missing channels that were rejected by ASR were then replaced via a spherical interpolation. The EEG data were then re-referenced to the common average of the 60 channels.

Independent Component Analysis and Dipole Source Localization

Statistically independent sources in the EEG data were identified using Adaptive Mixture ICA (AMICA) [124], which has been shown to have improved accuracy over traditional Infomax ICA [125]. The digitized electrode positions were aligned to the standard MNI brain model (Montreal Neurological Institute, Quebec, Canada) [126] and equivalent current dipole models were estimated to match the scalp projection of

each independent component using a standard three-shell boundary element model with the DIPFIT toolbox [122, 123]. The *fitTwoDipoles* plugin [127] was used to estimate symmetrically constrained bilateral dipoles if they provided a better fit over the single dipole model. Following the dipole fitting procedure, any dipoles that explained less than 90% of the residual variance of the component projections were rejected from further analysis. Additional components were rejected if their projections were deemed to be noise related, based on probabilistic estimates from the automated labeling plugin *IClabel* [128]. For visualizing dipole cluster locations, the remaining components were clustered according to their 3D locations using k-means to obtain across-subject and across-session component clusters. For all other spectral and temporal analyses, the remaining components were projected back to the EEG channel space and segmented in time to separate the walk and stop phases of kinesthetic imagery.

3.2.3 fMRI Analysis

All fMRI analysis was performed using standard processing steps on each subject's data with the open source SPM12 software package within MATLAB [129]. The DICOM images received from the scanner were first converted into the NIFTI format. The converted images were realigned (using the *Realign (Estimate)* function) by registering to the mean using a 2nd degree B-spline. The realigned images were then warped to the normalized space (*Normalize (Est & Wri)*), aligned to the first image of the series with very light regularization. These files were smoothed (*Smooth*) using default parameters to clean high frequency spatial artifacts before statistical analysis. Finally, each voxel time series was put into a voxel-based general linear model (GLM), where the block design sequence (timed to the stopping and walking onsets of the REX in the video) was convolved with the hemodynamic response function (HRF) to compute the BOLD signal.

After the preprocessing steps, both the Walk and Stop KI conditions were contrasted against the baseline Rest and also with each other. All contrasts were statistically thresholded with Family Wise Error-corrected $p < 0.05$ to identify individual regions of interest (ROIs). Due to the limited number of subjects, we did not perform any group comparisons of ROIs.

3.3 Results

3.3.1 Spatial Distribution of EEG Spectral Power During Imagination of Gait

The Thomson's multitaper power spectral density estimate was computed for each EEG channel (*pmtm* function in MATLAB) after segmenting the Walk and Stop phases of kinesthetic imagery. These were integrated into the five frequency EEG frequency bands: 0.1-4 Hz for δ, 4-8 Hz for θ, 8-15 Hz for α, 15-31 Hz for β, and 31-50 Hz for γ. The across-subject mean value of the logarithmic ratio between each condition and baseline rest are plotted on scalp maps for each frequency band (columns) and each session (rows) in Figure 3.2. As expected based on previous motor imagery studies, ERD is seen in the α range (middle column, blue/negative values), quite widespread but particularly over central motor areas and anterior-frontal cortex. The amount of α suppression increases by an average of 4.8 dB between Session 1 and Session 9, with the greatest changes in channels AFz, AF3, and AF4 (average change of -12.5 dB). Bilateral central and parietal channels CP1/2, CP5/6, C3/4, P3/4, and Pz show prominent suppression in Session 9 (-10.3 dB average for these channels) without having as large a change across sessions. Strong γ ERS (fifth column) is also consistent across most of the scalp for all sessions (7.24$\pm$3.8 dB). In contrast, the power ratios comparing Stop to Rest (right half of Figure 3.2) are much smaller as visually apparent given the fainter colored scalp maps. For Session 9, average α

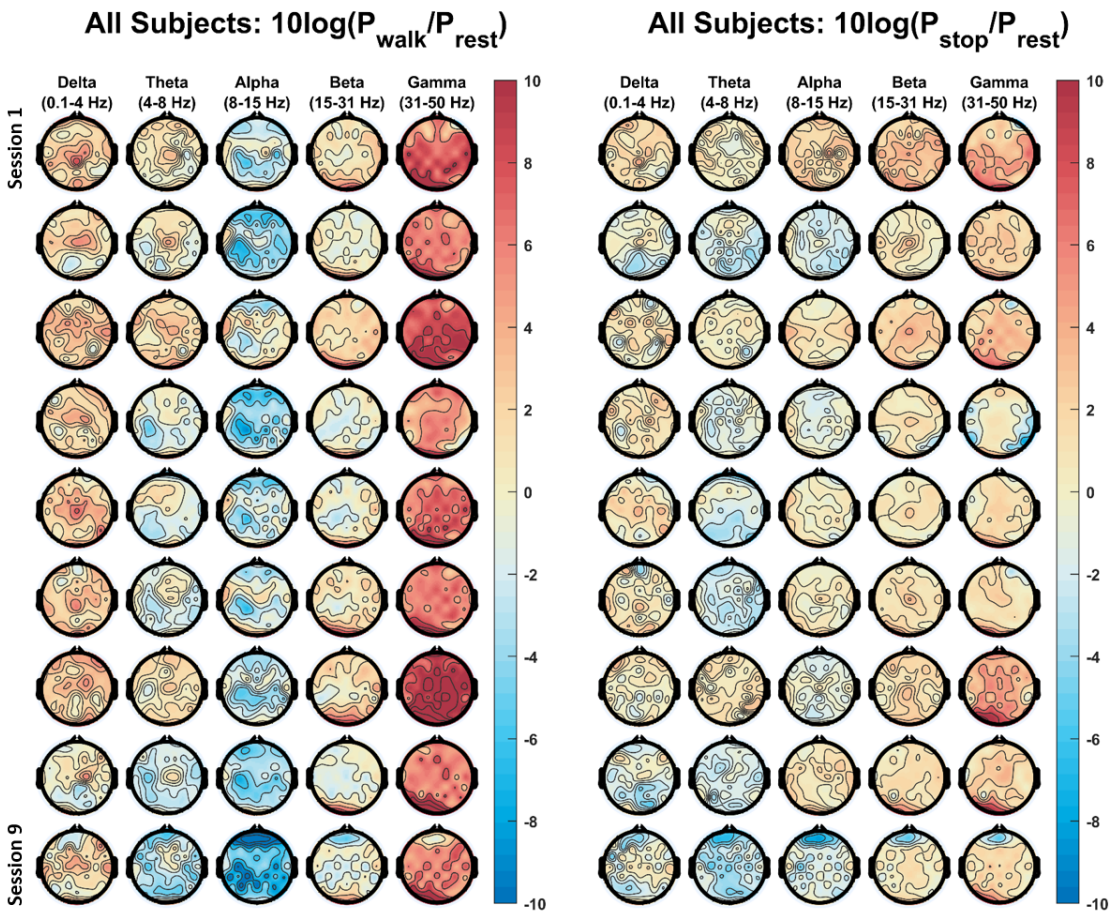

Figure 3.2: Event-related de-/synchronizations for both the Walk and Stop conditions versus Rest as baseline projected onto scalp maps and averaged for all subjects. Sessions descend in rows and each column corresponds to the five typical frequency bands within EEG.

Walk and Stop ERD are -6.3 dB and -1.6 dB respectively, and average respective γ ERS are 6.0 dB and 1.5 dB. This suggests that the KI during the Stop condition was mostly similar to the baseline Rest condition.

Individual subject ERD/ERS scalp maps contrasting Walk with Rest are shown for subjects S1 and S2 in Figure 3.3. These subjects were chosen as the best and worst (chance-level) performing subjects respectively in the BMI task as described in Chapter 2. Of these two subjects, only S1 shows strong α ERD, which also spreads to the θ and β frequency bands, while S2 actually shows some slight α ERS (mean 1.9 dB for all sessions and channels). The average change in α power in S1 decreases

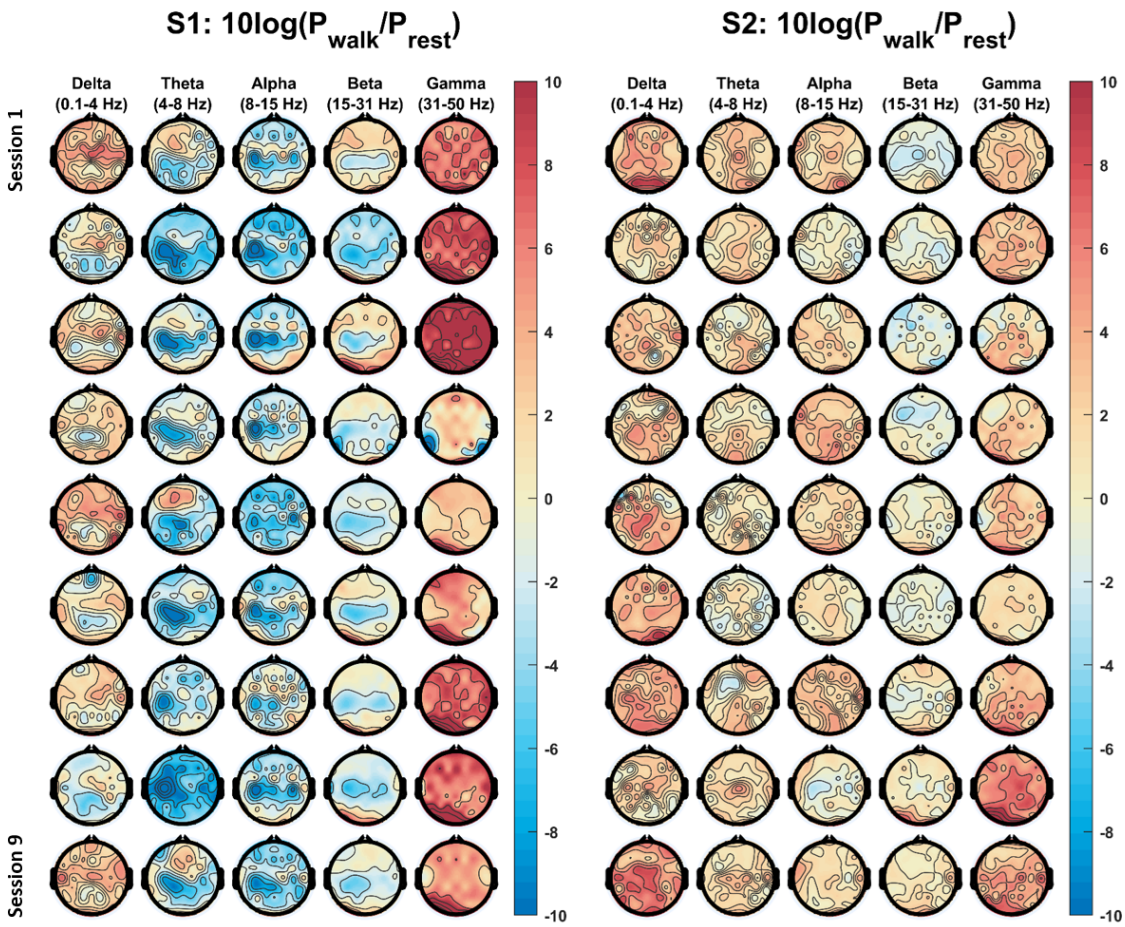

Figure 3.3: Event-related de-/synchronizations for Walk versus Rest projected onto scalp maps for the best (S1) and worst (S2) performing BMI subjects. Sessions descend in rows and each column corresponds to the five typical frequency bands within EEG.

from -1.8 dB to -3.2 dB between Session 1 and Session 9, and most commonly seen in central and parietal channels with slightly deeper blue areas (more suppression) in the left hemisphere. The trend in γ ERS is also prevalent in S1 at an average of 7.0 dB across sessions, while only 3.4 dB for S2.

3.3.2 Cortical Potentials Related to Walking Imagery

Next, we calculate the time course of ERD/ERS as temporal changes in spectral power relative to onset of walking and stopping KI. The time-series of each EEG

channel were band-pass filtered into each of the five frequency bands, squared in amplitude to obtain power samples, segmented ±2 s relative to the beep cue for switching between Walk and Stop KI states, and averaged across trials and channels. Additionally, the ERP was calculated with the same segmentation and averaging process without the filtering or squaring. These temporal signals are plotted for the average of all subjects and individually for S1 and S2 in Figure 3.4. The traces for Session 1 and Session 9 are shown to indicate pattern changes as a result of the longitudinal training. Note that there is a difference in scaling in the y-axis for θ power for S1 and α power for S2, as denoted by the red numbering. In the group-averaged data, there is a notable ERP response after both the Walk and Stop beeps, resulting in a peak of 0.12 μV approximately 420 ms after the Walk beep and a peak of 0.11 μV 460 ms after the Stop cue. In S1, this ERP peak also occurs at approximately 460 ms after the beep cue, but with a large increase 0.20 μV to 0.30 μV between the first and last session, and only peaks at 0.17 μV after the Stop beep. S2 has no apparent ERP peak during the Session 1, but the final session's amplitude is still reduced relative to S1 and occurs earlier (0.12 μV at 350 ms). Another notable change is the increase in α power seen in the group-averaged data before the Walk beep (while the subject is at rest) before and after the longitudinal training; this is the well-documented μ rhythm over sensorimotor areas [32, 104, 130], which increases from 13.5 μV^2 to 28.9 μV^2 after the nine sessions, and the heightened α decreases after the subject is cued to imagine walking. S2 was found to have very low α power overall (note the different y-axis scale), while S1 shows a more oscillating pattern whose peak preceding the Walk beep increases from 60.7 μV^2 to 83.1 μV^2 between Session 1 and Session 9, and then sees a sharp drop 200 ms after Walk beep. Patterns in the higher frequency bands (β and γ) are more varied and inconsistent with the average subject data only showing a sharp peak preceding the Stop beep.

We then look at the ERPs on a per channel basis, but filtered into the δ band as this was the frequency range of interest used during the BMI decoding in Chapter

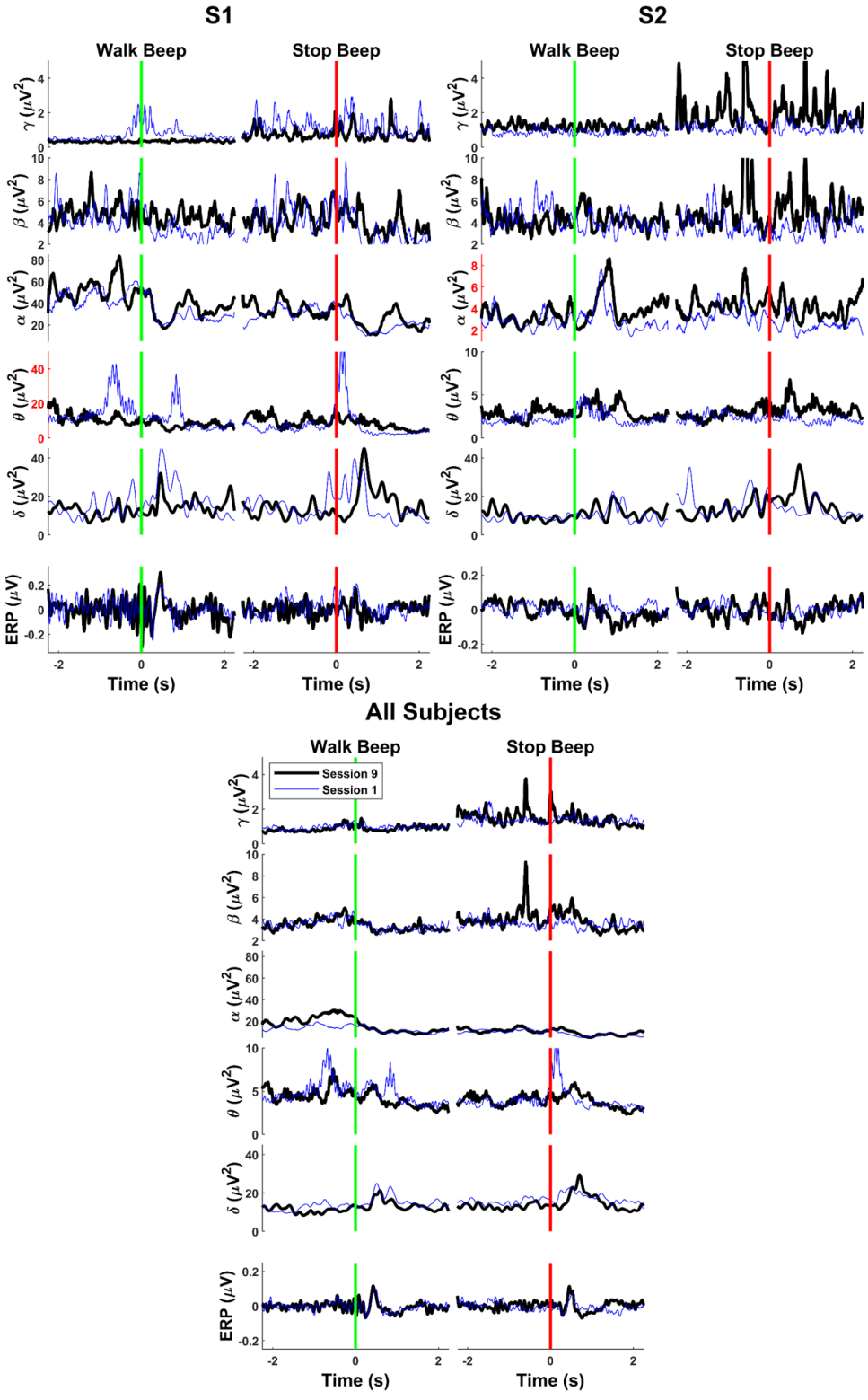

Figure 3.4: Time courses for the Event-Related Synchronizations and the Event-Related Potential for S1, S2, and group-averaged data relative to the Walk and Stop beeps. Data are shown for the first (thin blue trace) and last (thick black line) sessions to indicate change after the longitudinal training.

2. Individual traces for nine select channels over the central motor-related areas are shown for each session, color-coded on a yellow-red-black gradient (yellow for Session 1, black for Session 9) in Figure 3.5. The most common feature in these channels is a biphasic peak (a small negative deflection followed by a large positive peak) in response to both Walk and Stop beep cues. Peak negativity usually occurs about 250 ms after the cue ranging from -1.0 to -2.3 μV among the channels where visible in the group-averaged data, with the main positive peak occurring at about 450 ms ranging from 1.2 μV to 3.6 μV. The effect is much larger in S1 than in S2, the former having positive spikes larger than 13 μV. The largest amplitudes are found in the central and central-parietal channels (Cz, CP1/2/z), and only for these do we see a difference between the Walk and Stop conditions. The peak amplitudes do not vary significantly over sessions.

We also investigated changes in the movement-related cortical potentials (MRCPs) in this dataset to see how it evolved over training and its relation with BMI performance. These were obtained by passing the offline EEG data through a high-pass filter (0.1 Hz, 4th order Butterworth), then re-referenced using a large Laplacian spatial filter, and finally low-pass filtered (1 Hz, 4th order Butterworth) [131, 132]. As with the ERPs, these were segmented $\pm$2s relative to the Walk and Stop beeps and then averaged across trials. The MRCPs for the same nine central EEG channels are shown in Figure 3.6. Two distinct patterns are present among these signals: a negative deflection after the cue seen in the central and frontal channels and a positive peak with a negative rebound seen in parietal/posterior channels. The former is an example of the readiness potential, the increase in negativity in the MRCP that precedes movement [52, 55, 131, 133]. As with the other previous findings, these effects are most pronounced in S1 but diminished in S2 and the subject-averaged plots. The readiness potential negativity peaks around 800 ms (781$\pm$123 ms) for the group-averaged data. For the biphasic response, the positive peak occurs around 500 ms (485$\pm$39 ms) with the negative rebound around 1150 ms (1156$\pm$123 ms). No

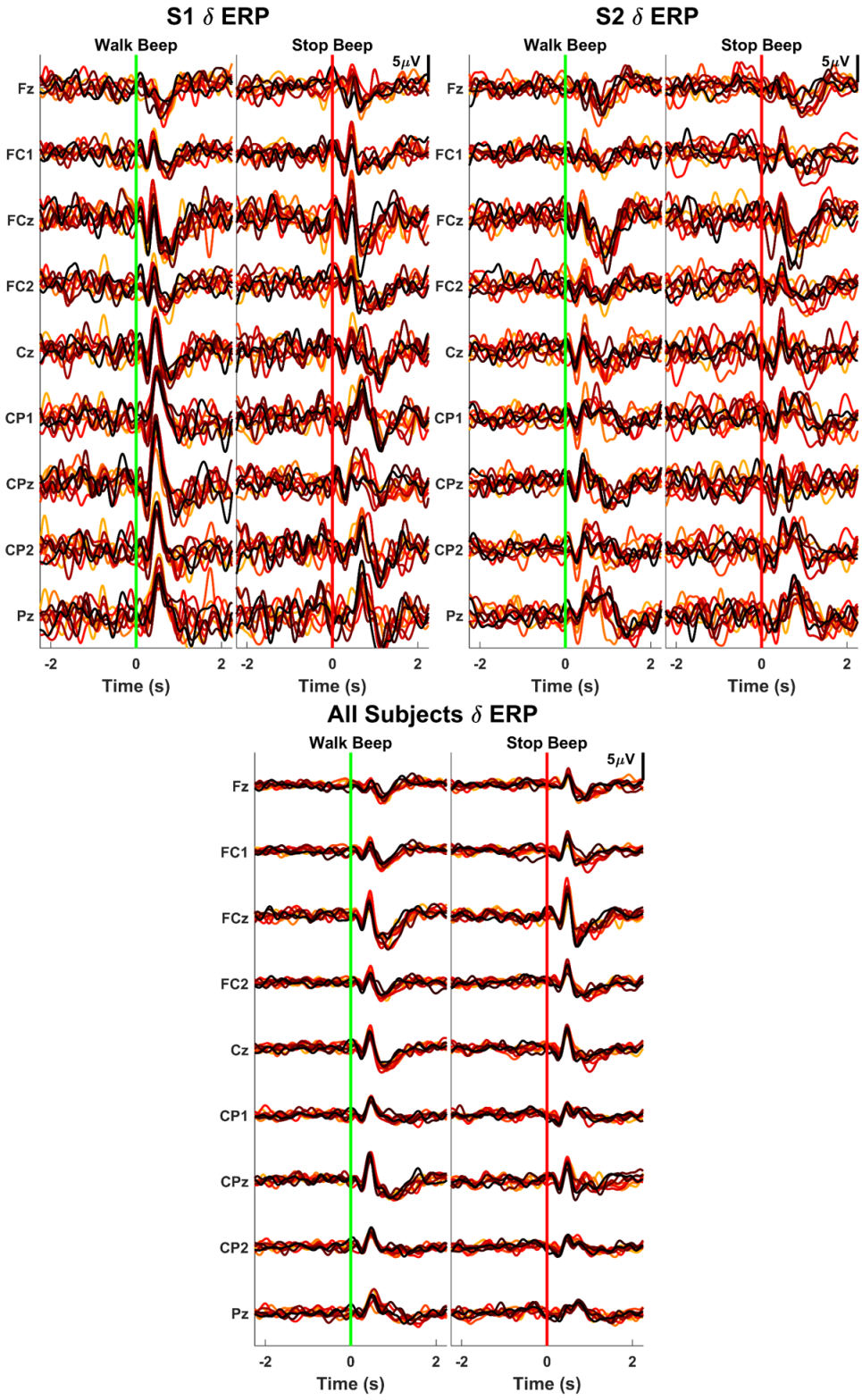

Figure 3.5: Traces for the ERP filtered into the δ band for select EEG channels over the central motor areas for S1, S2, and group-averaged data relative to the Walk and Stop beeps. Data are shown for all sessions, color-coded on a yellow-red-black gradient (yellow for Session 1, black for Session 9)

significant variability was found across sessions. The across-session average MRCPs were then plotted with Walk and Stop together on the scalp map topography in Figure 3.7. The Stop MRCPs show a similar response to the Walk response although with a lower peak amplitude for the readiness negativity and the biphasic positivity, particularly for channels closer to the vertex.

3.3.3 Localized Dipole Sources from EEG during Gait Imagery Training

Figure 3.8 shows a graph ranking the most frequently identified locations for the equivalent dipole sources associated with the EEG independent components. The most common location is the superior frontal gyrus in the right hemisphere, but the next three most common locations are on the left side specifically in the precentral, lateral occipital, and the superior parietal gyri. Some of these regions (e.g., superior frontal and precentral gyri) also show bilateral dipoles in both hemispheres. The dipole sources were then clustered based on their 3D location using a k-means algorithm with $k = 5$. The choice of five for the number of clusters was determined to be optimal based on the highest value of the Calinski-Harabasz Index and the Silhouette Coefficient clustering criteria for values of k from 5-15. The five individual clusters for the group data are shown in Figure 3.9 separately for the early and late sessions (Session 1-3 and 7-9 respectively). Clusters 1 and 2 both span the central superior parts of the brain, but are separated by the central sulcus. The centroid for Cluster 1 lies in the left posterior cingulate cortex for both the early and late sessions with a slight shift closer to the midline and increased membership from 23 components to 25. Cluster 2's centroid lies in the right precuneus and sees a drop in membership from 18 to 13. Cluster 3 spans the left temporal lobe with its centroid specifically in the bank of the superior temporal sulcus with no change in the number of components. Cluster 4 covers the rear occipital areas with the early sessions having 7 members

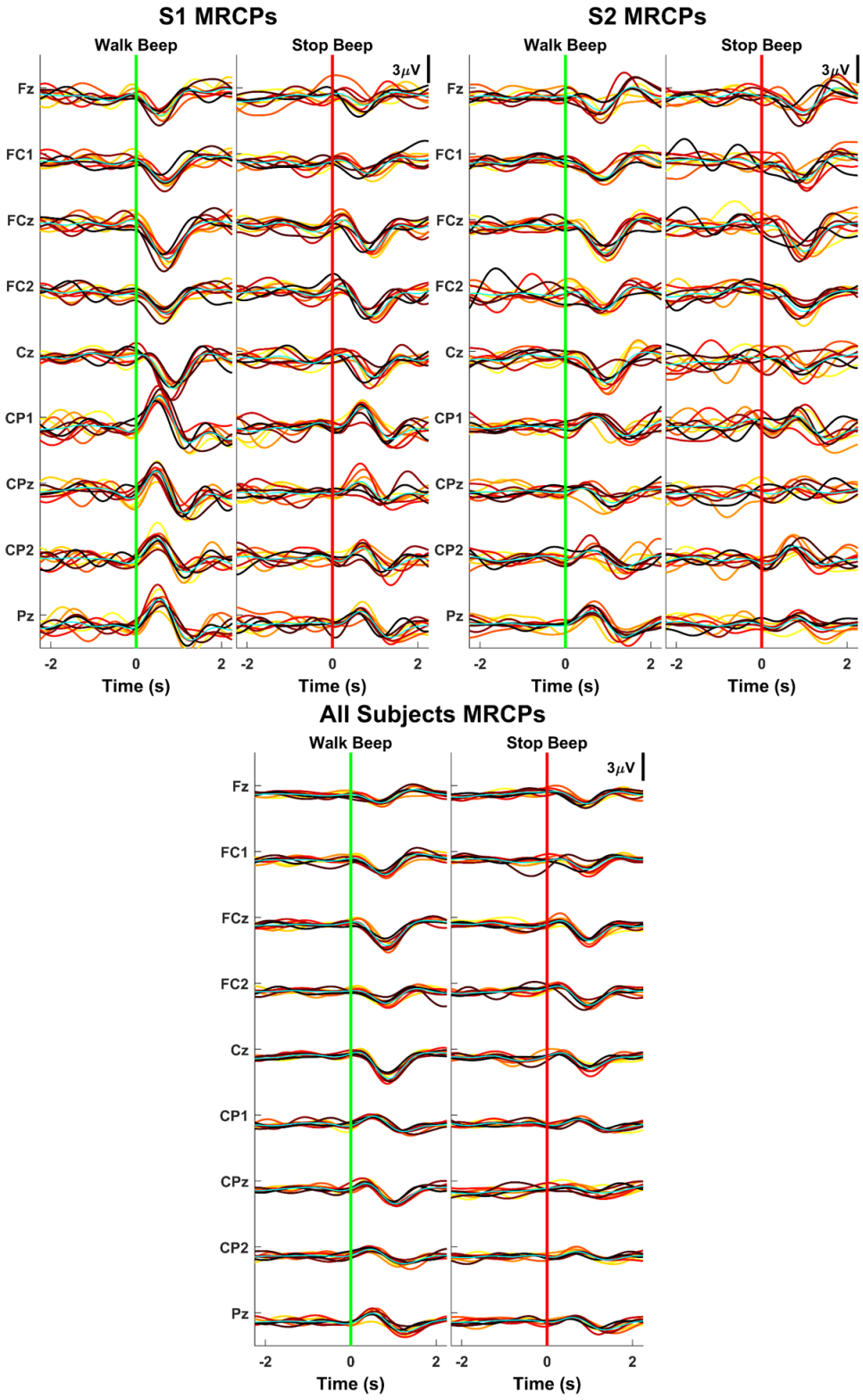

Figure 3.6: Movement-related cortical potentials for select EEG channels over the central motor areas for S1, S2, and group-averaged data relative to the Walk and Stop beeps. Data are shown for all sessions, color-coded on a yellow-red-black gradient (yellow for Session 1, black for Session 9) with the mean value as a cyan trace.

and its centroid in the left lateral occipital gyrus and the later sessions having 14 members centered around the left lingual gyrus. Cluster 5 is the most widespread of the clusters in frontal cortex, and sees the largest increase in membership from 10 to 24 and the centroid migrates from the right insula to the caudal middle frontal gyrus. The same five clusters are collectively visualized for S1 and S2 separately in Figure 3.10. The clustered dipole locations for S1 are a smaller representative sample of the grouped subject data, but with only 21 and 24 dipoles for the early and late sessions respectively. For S2, considerably fewer dipoles met the acceptable thresholds for residual variance and probability of being non-artifact (only 8 and 13 for early and late sessions), and the original Cluster 1 and Cluster 2 over the vertex have merged in the later sessions.

Additionally, Figure 3.9 shows the ERP associated with each dipole cluster obtained by averaging the independent component activation ± 2 s from each beep cue. The ERPs associated with Cluster 1 and Cluster 2 (i.e., those closest to motor areas) exhibit the most prominent responses. The Cluster 1 ERP response consists of biphasic peaks for both Walk and Stop: for Walk there is first a negative peak of -0.65 μV at 270 ms after the beep, followed by a positive peak of 0.5 μV at 430 ms, and then a slower negative rebound to -0.5 μV at 840 ms; the Stop ERP has a smaller first negative peak (-0.3 μV) that is slightly delayed at 320 ms but a larger positive peak extending to 0.65 μV with no second negative rebound. The ERP for Cluster 1 is greatly enhanced in amplitude with similar timings for Sessions 7-9 (note the difference in scaling on the y-axis): the first Walk negativity reaches -0.82 μV, rises to 0.55 μV, and drops to -0.88 μV for the slower negativity phase; the Stop ERP peak amplitudes are increased to -0.55 μV and 0.8 μV. For Cluster 2, the early Walk ERP reaches peaks of -0.33 μV (260 ms) and 0.59 μV (480 ms) and the negative rebound lasts up to 1.2 s after the beep; the corresponding Stop ERP only has a positive peak of 0.41 μV at 650 ms. The Walk ERP for this cluster does not increase at the end of the training, but there is seemingly contradictory α activity in the Stop ERP that

subsides after the beep, i.e., when the subject imagines coming to rest. Given the otherwise general similarities between the responses of these two clusters, there is also a consistent delay between the peak timings that could suggest a cascading of the same signal through a pathway connected by these regions.

3.3.4 Contrasting Walk and Stop Imagery through fMRI

All subjects, excluding S6 and S7, underwent an fMRI scan to measure brain activation while eliciting their KI and viewing first-person video playback of themselves walking in the REX. Changes in blood flow were measured from the BOLD contrast to indicate regions of temporal brain activity. The segmented Walk and Stop scans were contrasted using statistical parametric mapping. Figure 3.11 shows regions of statistically significant activation in which voxels during Walk KI had higher intensity than during Stop KI through a glass brain view. Despite having rather disparate BMI performance, patterns of activation are most similar in S1, S2, and S4, for which the most significant areas of activation are in supplementary motor cortex (SMA) by the interhemispheric fissure and the bilateral inferior occipital gyrus (IOG). Subect S3 also had very good BMI performance but very different patterns of activation than S1, with more widespread activation emphasizing the bilateral superior parietal lobule and cerebellum more than the IOG and central gyrus near motor areas. S5 had very little activation in motor areas but also recruited bilateral IOG. Coronal slices for each subject's T1-weighted structural scans are shown in Figures 3.12-3.16 overlaid with contrast blobs both for which activation in Walk is statistically greater than Stop and vice versa. Although on a smaller scale of T scores, there is still significant activation during Stop KI, particularly in S2 and S3 in the cerebellum, cuneus, postcentral gyrus, lingual gyrus, and occipital pole. The full information of all identified significant activation clusters and their associated brain regions for all subjects are shown in Table 3.1 for Walk activation and Table 3.2 for Stop activation.

Table 3.1: Regions of brain activation and MNI coordinates for each subjects' fMRI contrasts of Walk KI vs. Stop KI.

Subject	Brain Region(s)	t value	MNI Coordinates (mm)		
			x	y	z
S1					
	L/R supplementary cortex, L precentral gyrus	21.7	0	-10	74
	L inferior occipital gyrus	20.2	-52	-74	8
	R inferior occipital gyrus, R middle temporal gyrus	16.6	54	-68	6
	R/L cerebellum exterior, L inferior occipital gyrus	13.0	34	-46	34
	R superior temporal gyrus, R supramarginal gyrus	12.4	68	-36	14
	L planum temporale, L superior temporale gyrus, L supramarginal gyrus	10.9	-64	-34	16
	L/R postcentral gyrus	9.9	-42	-28	40
	R superior parietal lobule, R supramarginal gyrus	7.9	34	-34	48
	R precentral gyrus	7.7	16	-32	46
	L/R thalamus	6.8	-4	-20	2
	brain stem, cerebellar vermal lobules I-V	6.5	10	-30	-18
S2					
	R/L inferior occipital gyrus, R middle occipital gyrus	13.0	50	-72	0
	L supplementary motor cortex, L precentral gyrus	12.0	-2	-12	76

Table 3.1: Continued

L/R parietal operculum, L planum temporale, L supramarginal gyrus	11.0	-50	-40	26
L/R superior parietal lobule	9.3	-26	-42	48
S3				
R occipital pole, R/L superior parietal lobule	20.1	20	-96	0
L/R cerebellum exterior	17.8	-16	-66	-18
L inferior occipital gyrus, L middle temporal gyrus	17.4	-22	-98	0
R/L precentral gyrus, R/L postcentral gyrus	15.8	62	2	34
L temporal gyrus, L fusiform gyrus	15.5	-62	-8	-26
R/L superior frontal gyrus, R frontal pole	14.3	16	70	20
L middle occipital gyrus, L superior occipital gyrus	13.8	-28	-94	24
R lateral orbital gyrus	12.5	38	58	-14
L angular gyrus, L superior parietal lobule	12.3	-40	-72	48
R pallidum	11.8	18	2	0
L/R middle frontal gyrus	11.5	-52	4	42
R supramarginal gyrus	11.1	62	-34	28
brain stem	9.9	4	-46	-62
L supplementary motor cortex	8.7	-10	10	52

Table 3.1: Continued

	L calcarine cortex, L lingual cortex	7.6	-16	-66	2
S4					
	R/L superior parietal lobule	9.4	30	-44	44
	R middle/superior temporal gyrus	8.7	58	-62	-4
	L parietal operculum	8.2	-48	-38	24
	R/L precentral gyrus, L supplementary cortex	8.2	4	-16	68
	L inferior temporal gyrus	6.8	-48	-38	24
	L putamen	5.6	-26	-2	6
	R precuneus	5.4	12	-50	50
S5					
	L inferior occipital gyrus, L middle temporal gyrus	17.0	-24	-98	-2
	R inferior occipital gyrus, R occipital pole	15.1	28	-84	4
	L/R precentral gyrus	9.9	-30	-4	40
	L superior parietal lobule	7.8	-38	-40	48
	L parietal operculum	7.7	-46	-34	16
	R supramarginal gyrus	7.7	64	-18	40
	L/R cerebellum exterior	7.5	-18	-66	-22
	L inferior frontal gyrus, L central operculum	7.0	-50	10	4

Table 3.2: Regions of brain activation and MNI coordinates for each subjects' fMRI contrasts of Stop KI vs. Walk KI.

Subject	Brain Region(s)	t value	MNI Coordinates (mm)		
			x	y	z
S1					
	L/R cuneus	8.9	-8	-90	-16
	L superior parietal lobule	8.3	-18	-78	54
	L superior temporal gyrus, L planum temporale, L middle temporal gyrus	7.6	-56	-34	6
	R transverse temporal gyrus, R superior temporal gyrus	7.0	46	-14	0
	L inferior frontal gyrus, L middle frontal gyrus	6.1	-46	20	24
	L middle temporal gyrus	5.7	-54	-48	2
S2					
	L inferior occipital gyrus, L cuneus	11.5	-24	-96	-10
	R occipital pole, R lingual gyrus	10.4	26	-98	-4
	L/R middle frontal gyrus, R central operculum	9.7	-40	50	4
	R/L postcentral gyrus	9.1	0	-40	74
	R/L supramarginal gyrus	8.4	64	-46	28
	L middle frontal gyrus, L superior frontal gyrus	7.8	-30	38	38
	L/R cingulate gyrus, L precuneus	7.1	-2	-26	28

Table 3.2: Continued

L posterior insula, L superior temporal gyrus, L transverse temporal gyrus	6.7	-32	-26	16
L temporal pole, L entorhinal area, L posterior insula	6.6	-40	4	-18
R precentral gyrus	6.4	42	-12	56
R cerebellum exterior	6.4	10	-78	-34
L superior parietal lobule	6.4	-24	-72	54
L/R caudate	6.3	-10	10	10
R putamen, R caudate	5.8	26	16	-4
R cerebellum exterior, cerebellum vermal lobules I-V	5.8	10	-66	-10
R superior frontal gyrus	5.6	26	22	58
S3				
R precuneus, L postcentral gyrus	20.0	6	-54	66
R/L cerebellum exterior	14.8	12	-86	-44
R lateral ventricle, R lingual gyrus	9.3	26	-42	10
L temporal pole	8.5	-54	4	-42
brain stem	7.6	4	-28	-52
S4				
R/L cerebellum exterior	6.1	36	-76	-26

Table 3.2: Continued

S5					
	R/L lingual gyrus	9.3	14	-72	-8
	L/R superior occipital gyrus	8.4	-22	-90	22
	R superior temporal gyrus	6.9	64	0	-2

3.4 Discussion

3.4.1 Neural Signatures of Gait KI with an Exoskeleton

The underlying neural correlates of the kinesthetic imagery of walking while undergoing BMI training to control a robotic exoskeleton were explored using both EEG and fMRI analysis. The fMRI results show slightly varied patterns of activation in the five subjects that underwent the scanning, with the most consistently activated regions including motor-related areas (supplementary motor area, SMA, and precentral gyrus/primary motor cortex, M1) close to the leg representation in the interhemispheric fissure and areas associated with visual processing (bilateral inferior occipital gyrus, IOG, and superior parietal lobule, SPL). Numerous studies find similar activation in SMA, specifically associated with motor initiation [30, 54, 83, 84, 102, 103, 105, 113, 116], while M1 activation, involved in motor execution, is less consistently found during KI [102, 104, 105, 113]; S1, S2, and S4 all show activation in both SMA and M1, S3 shows activation in SMA only, and S5 does not show any in this region. Among visual areas, the SPL was most consistently activated while the IOG was only found in 4 subjects but was usually among the strongest activated regions. The SPL is more commonly involved during non-kinesthetic visual motor imagery (VI) [83, 107, 113, 134], and lesions to this region can impair motor

imagery ability [110, 135]. The IOG is observed less frequently during motor imagery, more notably known for visual processing and recognition of shapes and faces [136, 137, 138]; IOG activation has been seen in a gait-imagery study in Parkinson's disease patients watching a video of an actor walking [139] and another study with healthy subjects imagining walking down a path displayed on a screen [140]. This suggests that the video playback of the subjects walking in the REX may have contributed to increased activity in the IOG rather than the walking imagery. Consistent activations during the Stop phase occur in the cuneus/ precuneus for S1, S2, and S3, known for visual processing and generating mental images [83, 105], but also the brain's default mode network active during wakeful rest [141, 142]. This inter-subject variability is not unexpected [30, 55], as subjects may be employing different imaging strategies. The lack of activation in M1 or SMA in S5 suggests that the subject may have only trained using VI instead of KI.

The localized dipole sources derived from the EEG data also reflect the patterns found in the fMRI activations. Cluster 1 and Cluster 2 in Figure 3.9 both span somatosensory areas near representation of the legs, although Cluster 1 most directly reflects the M1 and SMA activation found in fMRI. The centroid for Cluster 2 lies in the precuneus, and the centroid for Cluster 1 is in the posterior cingulate cortex, which has shown to be active in other imagery studies [84, 102]. Cluster 4 likely corresponds to the visual areas that were activated. The top regions in Figure 3.8 have a near one-to-one correspondence with fMRI activations: precentral L represents M1 and SMA, lateraloccipital L contains the IOG, superiorparietal L for the SPL, with the precuneus rounding out the top five. Interestingly, the most common singular region is the right superior frontal cortex (Cluster 5), which sees the largest increase in dipoles over the training. Only S3 showed active frontal cortex in the fMRI data, but frontal cortex activation has been previously reported during walking KI [30, 83, 105]. S3 was one of the subjects that had an overall good BMI decoding performance, and later described his strategy as less focused on the KI but task-oriented in trying to

reach a target destination, which may account for more activity in frontal areas.

The EEG results also show the expected α suppression associated with movement well-established in the literature [31, 41, 112, 117, 118]. The α ERD is mainly localized to central motor areas as seen in Figure 3.2 and Figure 3.3, with some increase in power in the surrounding channels, the noted focal ERD/surround ERS effect [117, 118]. There is a slightly more suppression in the left hemisphere, which may be related to the right-handedness of all the subjects or that the REX would always make its first step with its right leg. Some of the ERD extends to θ and β frequencies, particularly for S1, which has also been documented by Reynolds et al. [117]. This comes at the expense that we do not see the expected ERS in the β band [31, 112]; it is possible that since this phenomenon usually occurs in the higher end of β, the expected ERS was canceled out by the α ERD that extended to the lower end of β, yet may still be visible as γ ERS. In the time domain (Figure 3.4, it is apparent that α power drops in response to the Walk beep, but the reduced α power does not rebound after the Stop beep. One plausible explanation is that the REX takes several seconds to come to a stop after the beep and the α rebound is slow and occurs outside of the 2s window plotted.

An apparent but noisy ERP response emerges as a response to both cues; much of the noise is reduced when the signal is filtered into the δ band and averaging is limited to central channels 3.5. Moreover, the ERP maintains its profile after source localization and averaging across dipoles clustered within sensorimotor cortex, and the biphasic spike and the timing of the peaks are consistent with other studies using motor imagery that have identified these spikes as the N2 and P3 peaks [29, 143, 144, 145]. Similarly, the MRCP obtained via spatial filtering shows the expected negativity of the readiness potential [52, 55, 131, 133] in central and frontal channels that would be overlying motor and premotor cortex. A response with a different profile and a switch in polarity occurs in the parietal and occipital channels that may originate

from a source from a different dipole cluster and/or may be related to a response from visual structures involved in kinesthetic imagery.

3.4.2 Impacts from the Longitudinal Study

One of the goals of this study was to determine the long-term effects of KI and BMI training through multiple sessions as a longitudinal study. Although there was variability among subjects in their neural signatures, there were several features that showed a persistent increase between the start and end of the training in the group-averaged data. The amount of α power suppression (ERD) increases across sessions, particularly over the central motor areas, as a consequence of heightened μ rhythm during the Rest and Stop phases preceding the Walk beep. We did not observe any change in the amplitudes of the MRCP, as otherwise reported by Yao et al. [84], finding a 20% increase in the MRCP of Cz and C3. Their subjects trained for 5 days/week over 6 weeks, so both the frequency and duration of training would likely have played a factor. We did find an increase in the peak amplitudes of the average-channel ERP between the first and last sessions, which is accentuated in the best performing BMI subject as well as in the cluster-averaged ERP for motor cortex. The year-long multi-faceted rehabilitation protocol by Donati et al. saw a much larger increase in the ERP on the order of magnitudes, while our peak increase was approximately 60%. Their study also saw an increase in the number of dipoles clustered near motor cortex, while we saw notable cluster growth for the frontal cortex and visual areas. As stated previously, their study also incorporated physical rehabilitation with overground body-weight support and an exoskeleton, virtual reality KI training with tactile feedback, and BMI control of a virtual and physical exoskeleton. Moreover, their subject population comprised of patients paralyzed from spinal cord injury, who may have started the training with a depleted motor representation in the brain. While we did not measure outcome changes in motor execution

and physical performance, the literature is quite unified that longitudinal KI training can be useful in various aspects of physical rehabilitation and motor training [84, 86, 88, 89, 90, 91, 92, 92, 93, 94, 95, 96, 97, 98].

3.4.3 Implications for BMI Control

Our analysis showed several EEG signatures of kinesthetic imagery that may be useful for BMI control. We found identifiable peaks in both the ERP and MRCP that would be detectable before movement onset. One of the pitfalls of our decoding model used in Chapter 2 that may have accounted for poor performance was the use of 200 ms for window size to create the EEG feature matrix. While longer window sizes would lead to increased computational time and thus a slower response time, there would likely be a trade-off for better performance and reliability. Other BMI studies used particularly larger window sizes ranging from 750 ms to 2s to detect motor intention [30, 52, 54, 55], and adopting a longer window may help us detect peaks in the ERP or MRCP. The average distance between the N2 and P3 peaks in our δ-filtered ERP was about 200 ms, and we would ideally want to use a longer window to fully capture this feature. Similarly, the MRCP doesn't reach peak negativity until about 800 ms after the cue. Using δ band features seems to have helped our signal-to-noise ratio in detecting these EEG features, but this can be improved upon further by using select channels over the central motor areas, since the peripheral electrodes within the 60-channel montage may simply contribute more background noise. Another strategy that has been effective in other studies [29, 55, 112] is to use imagined hand movement to elicit a detectable response to initiate walking. This would be easier to distinguish multiple classes, such as left movement vs. right movement, since hand representation in cortex is spread out more laterally in motor cortex. However, our goal was to develop a more intuitive BMI that initiates movement with natural mental imagery.

There is also the issue that the noted responses after the Walk and Stop beeps have very similar profiles of sharp transient peaks. It is unlikely that these similar responses are due to an auditory evoked potential, as the relevant literature describes these as occurring within 100 ms of hearing the beep cue, roughly 50 ms for the first positive peak over posterior areas and a negative peak about 100 ms afer onset over frontocentral areas [146, 147, 148]. Regardless, if we were to continue to rely on these features for BMI control, we may have to reconsider from trying to reliably distinguish between the two signals to utilizing them in a different way. Instead of a different response corresponding to Walk and Stop separately, the ERP may serve better as a brain switch to toggle between the two states [75, 120, 149]. Subjects would then no longer need to sustain their KI for the duration of the phase, and could just reactivate it when needed to toggle a switch to the next state. The literature does not have a consensus on the effects of sustained vs. transient imagery, sometimes seeing stronger β oscillations/weaker ERD in the former case [150, 151] or vice-versa [117]; this effect would need to be explored further to demonstrate its viability for usage in BMI applications.

3.4.4 Limitations

This study has several limitations that are important to address. First, we had a small sample size both in terms of the number of subjects (7) and the number of trials and data points (6 Walk and 6 Stop cues per each of the 9 sessions). This would normally be insufficient for most ERP studies that require averaging of sometimes hundreds of trials to elucidate a clear response with a high signal-to-noise ratio. Furthermore, only five subjects were able to receive an fMRI recording, limiting the extent to which we can identify overall trends for a generalized population. But in order to have had more subjects and more data per subject, we would need to disassociate the KI training aspect of this experiment from the larger BMI training

paradigm, since the collected KI data served mainly to gather training data for the BMI classifier.

Secondly, the limited data and the variability within it makes it difficult to clearly identify longitudinal trends. For the sake of presentation, we were only able to report the first and last measurements but do not use regression to establish a statistically significant change. It would also have been beneficial to have recorded an fMRI from subjects at the very beginning of the protocol, to be able to compare both structural and functional differences as a result of the longitudinal training.

Thirdly, a kinesthetic imagery paradigm is often difficult to execute properly. When performed for long periods of time, KI can be cognitively demanding for subjects [108, 117], leading to fatigue and decreased performance at the end of sessions. It is also difficult to enforce whether subjects are properly working to elicit KI, as opposed to visual imagery or focusing their general attention on the task. The disparate fMRI activations give us some insight into this: S5 likely only performed with VI due to a lack of activation in and around motor cortex, and S3 may have pursued his own unique task-oriented strategy prioritizing successful BMI performance over eliciting a strong KI response. We administered the Motor Imagery Questionnaire (MIQ-RS) [121] to determine an objective measure of the subjects' ability to elicit kinesthetic vs. visual imagery (results reported in 2.2, but no clear connection could be found between scores and either BMI performance or strength of neural responses. Moreover, measuring EMG from the leg muscles during the task would have helped us determine with certainty that the subjects were not making overt attempts at movement (but restrained by the exoskeleton); motor imagery by definition is no longer imagery if there is any detectable activation in EMG [102].

3.5 Conclusions

In this study, we investigated the neural correlates of the kinesthetic imagery of gait throughout the duration of a longitudinal BMI training paradigm to control a walking exoskeleton. EEG data were collected and analyzed while subjects were instructed to elicit their KI for alternating Walk and Stop cycles in an exoskeleton over nine longitudinal sessions. Our results demonstrates changes in α suppression and μ rhythm activity, pronounced responses in the ERP and MRCP in response to the cue to switch states, and cortical activity related to the mental imagery of walking localized in both motor and visual areas of the brain. This work contributes to the body of literature by assessing what cortical changes transpire, as measured by EEG and fMRI data, as a result of nine sessions of training subjects to use their KI to control a walking exoskeleton. Future steps that could further the results presented in this chapter would be to enroll patients paralyzed from spinal cord injury to track improvement and recovery in motor response, investigate changes in functional and structural connectivity within EEG and the fMRI diffusion tensor imaging respectively, and identify correlates of a more intuitive/less cognitively demanding mode of motor imagery that could serve as a useful tool for BMI control. Additionally, this study can be integrated with either functional electrical stimulation or vibrotactile feedback [29, 54, 117] to improve upon these findings for more enhanced neural responses, better clinical outcomes for recovery, and more robust BMI performance.

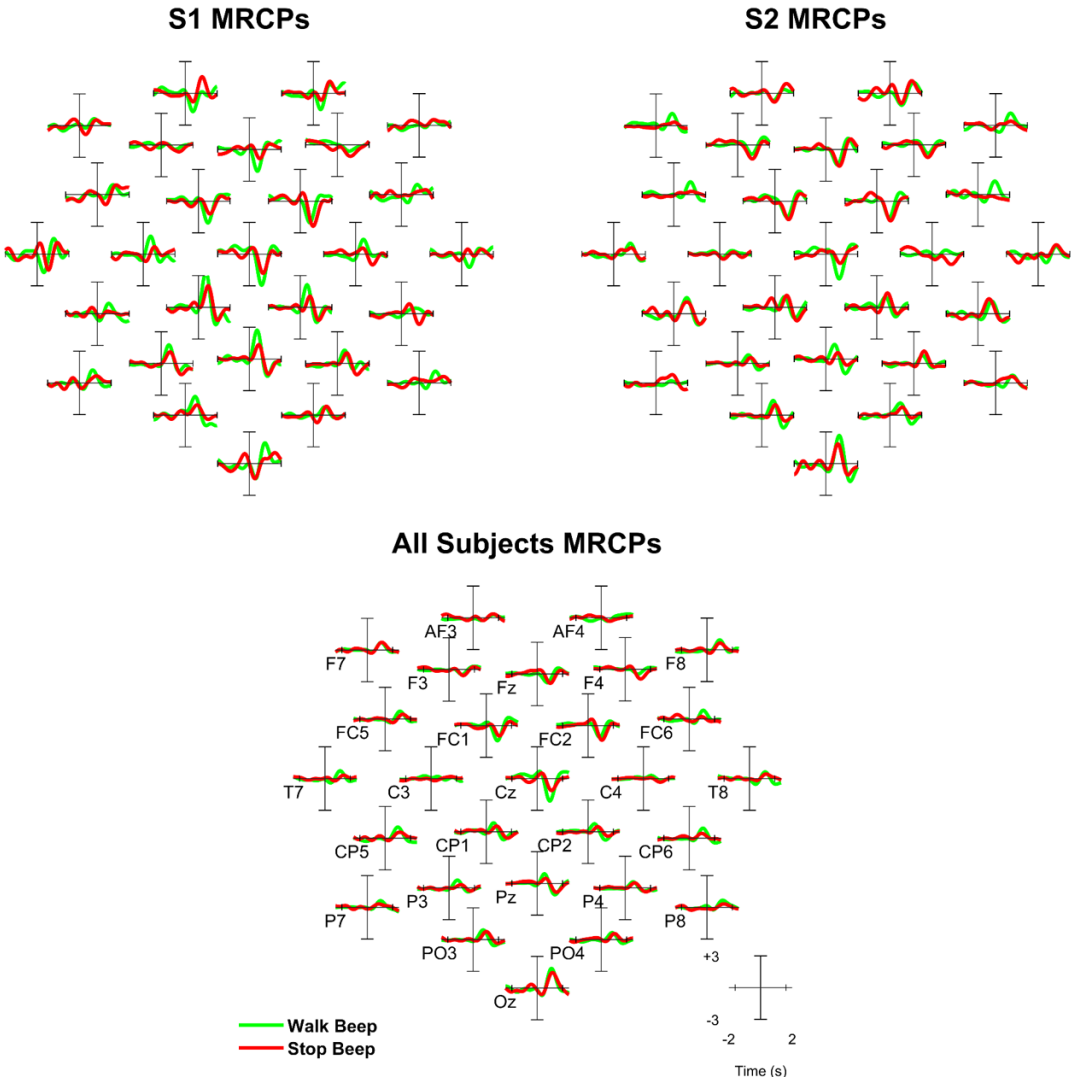

Figure 3.7: Movement-related cortical potentials plotted over the scalp topography for S1, S2, and group-averaged data overlaying the Walk (green) and Stop (red) conditions.

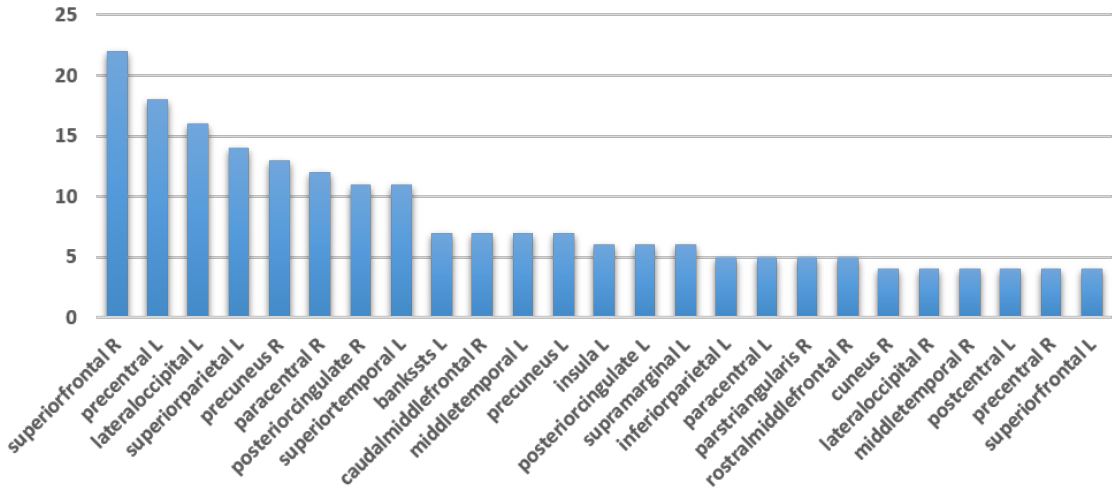

Figure 3.8: Counts of the most frequently occurring brain regions associated with the localized dipole sources for all subjects and sessions.

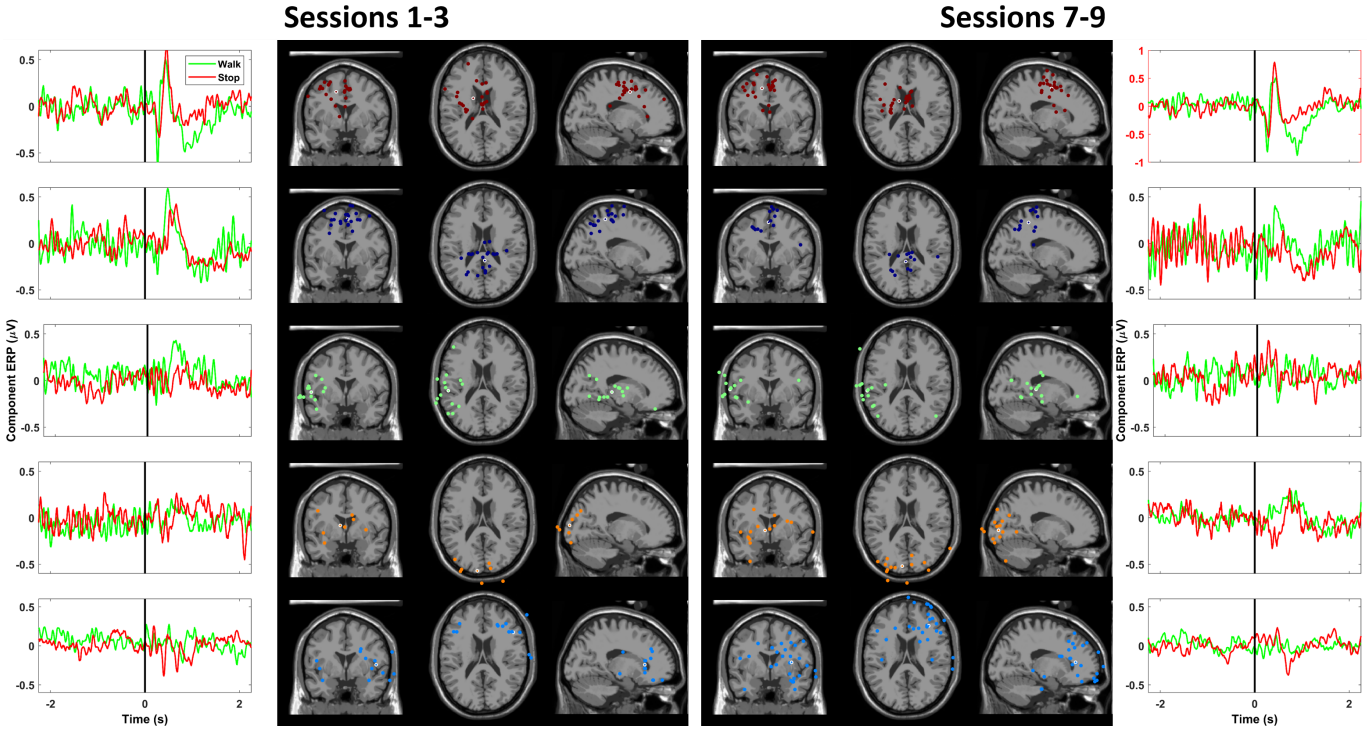

Figure 3.9: Clustered dipoles visualized on a generic brain MRI and the associated Walk and Stop ERP for each cluster, shown in rows. Dipoles are shown for all subjects but separated between early (Sessions 1-3) and late sessions (Sessions 7-9). Cluster centroids are indicated with a white ring. Red text denotes different scaling.

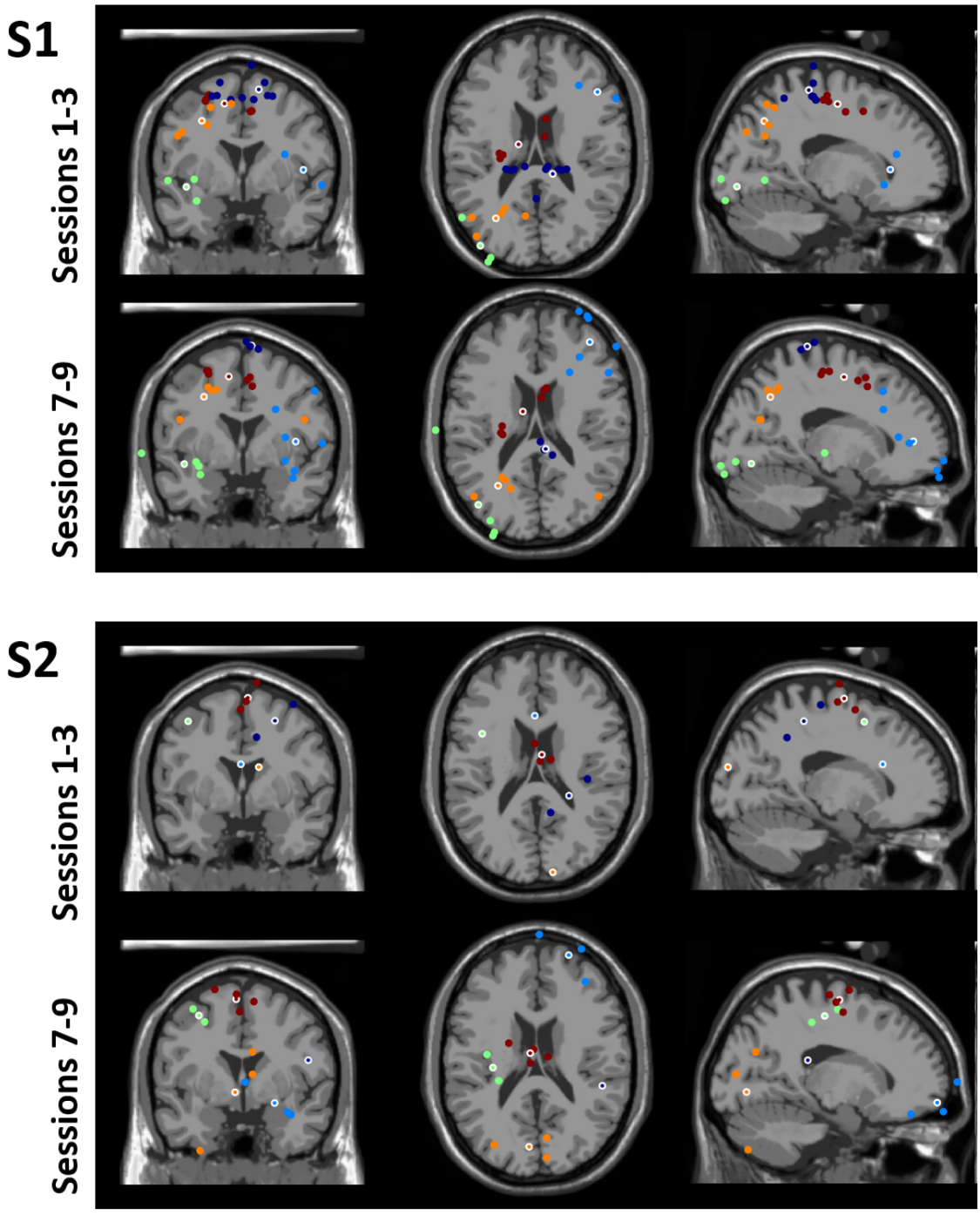

Figure 3.10: Dipoles visualized on a generic brain MRI with all clusters colorized for S1 (top) and S2 (bottom), separated by early (Sessions 1-3) and late training sessions (Sessions 7-9). Cluster centroids are shown in white with the center colored the same as the rest of the cluster.

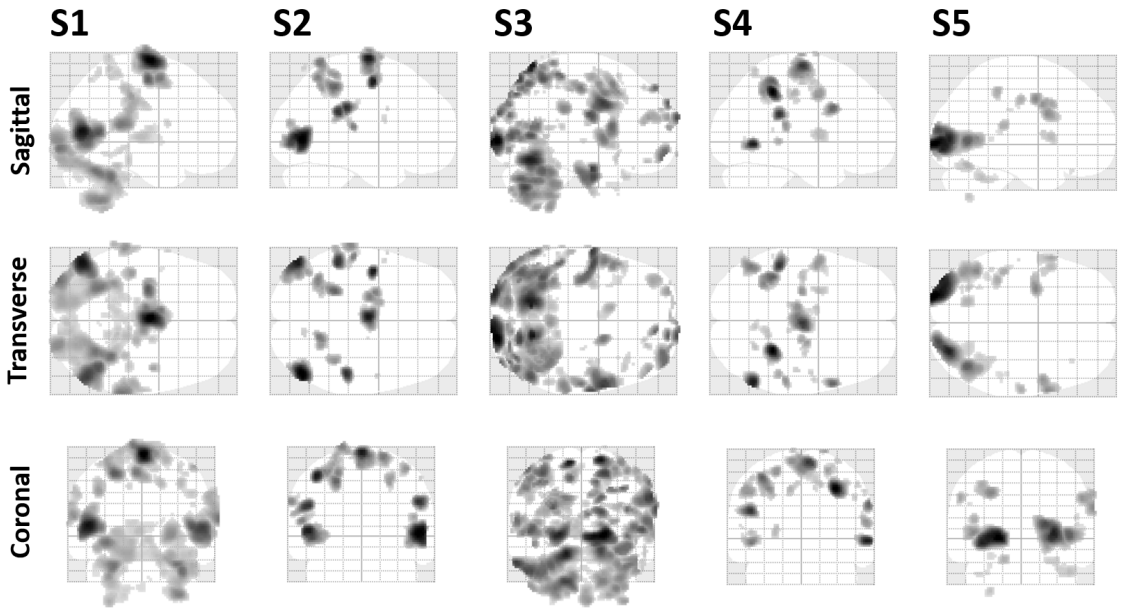

Figure 3.11: Glass brain views showing regions of statistically significant activation where voxels during Walk KI have higher intensity than during Stop KI.

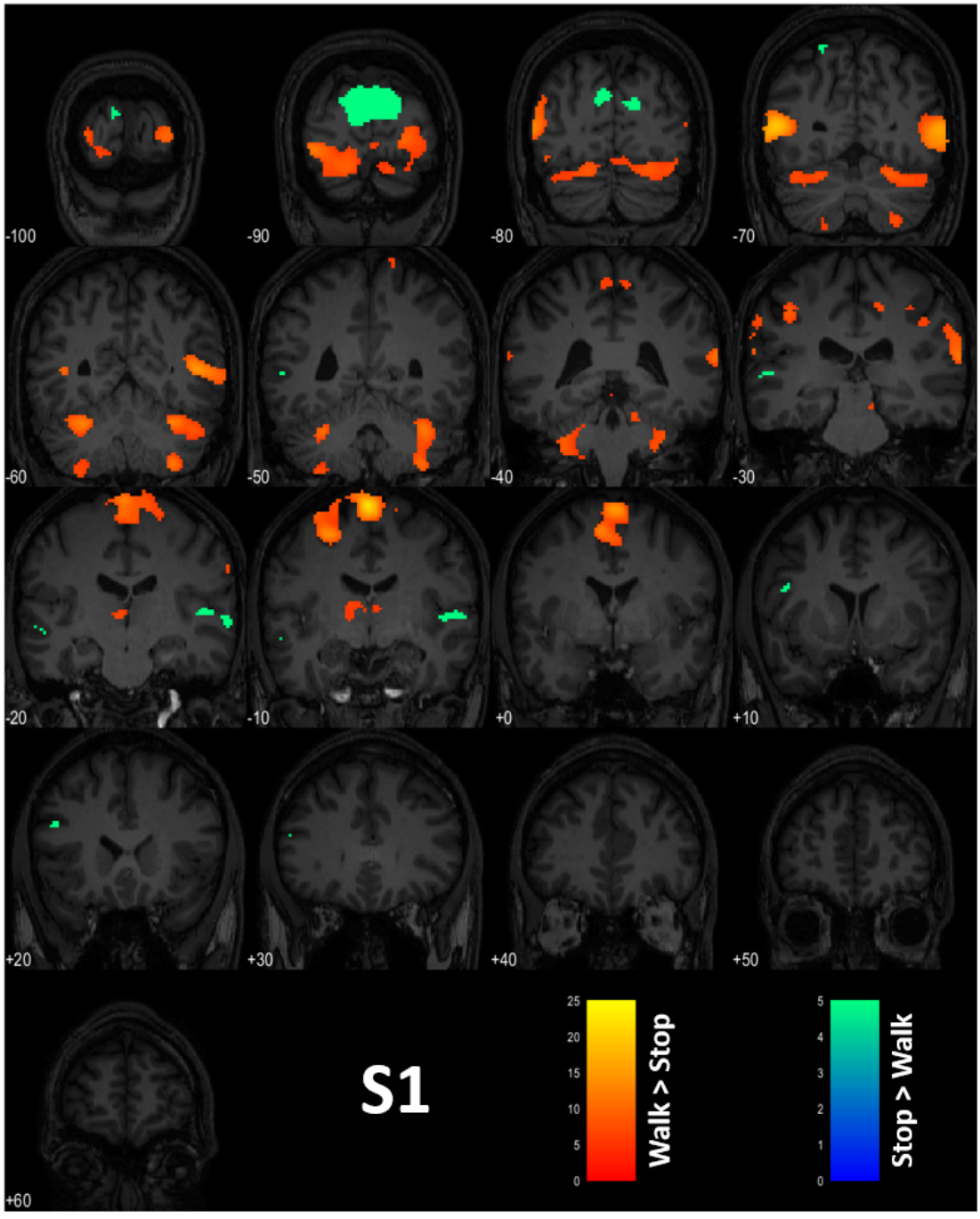

Figure 3.12: Coronal slices of subject S1's T1-weighted structural MRI overlaid with blob contrasts for both significant increases and decreases in voxel intensity during Walk and Stop KI.

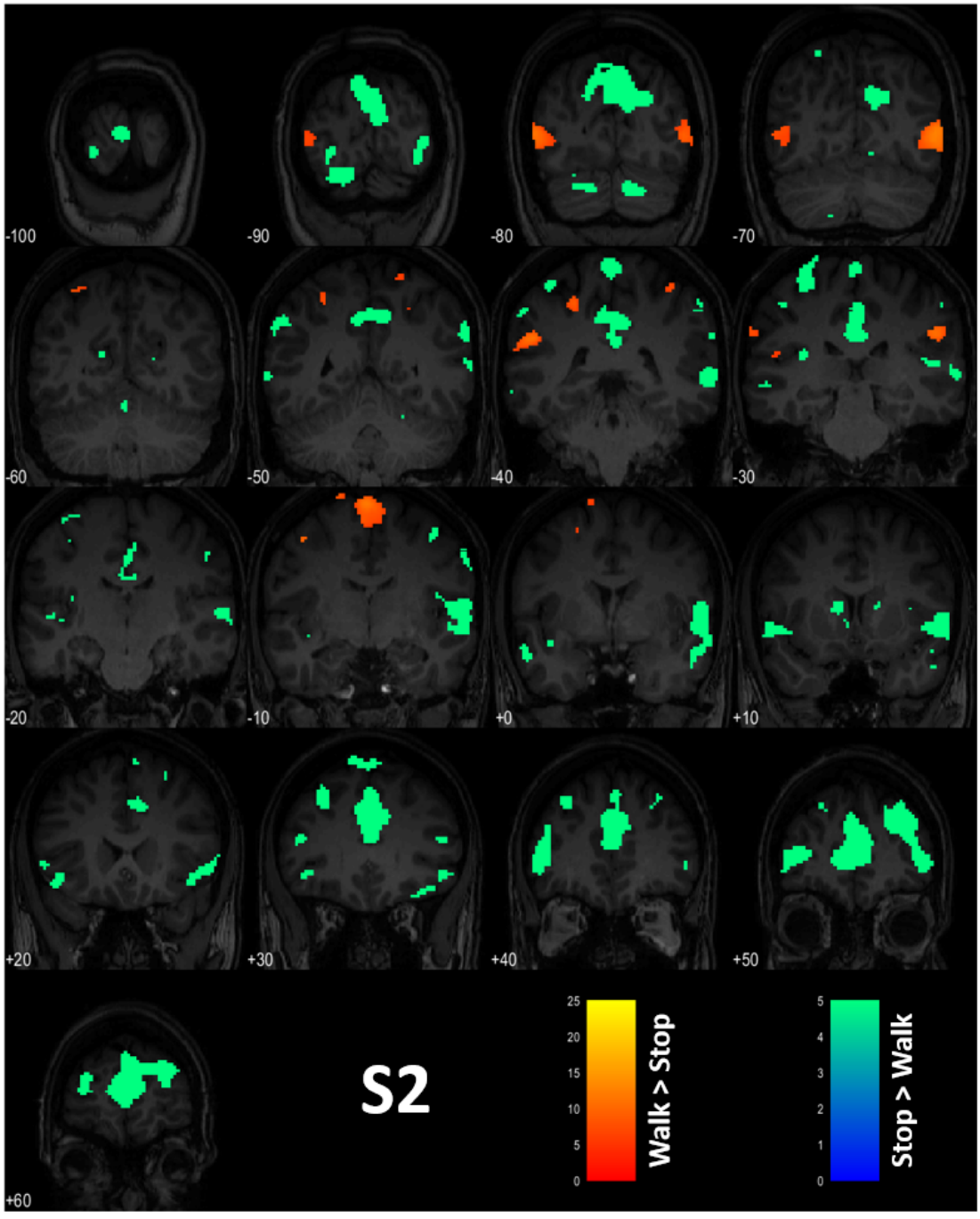

Figure 3.13: Coronal slices of subject S2's T1-weighted structural MRI overlaid with blob contrasts for both significant increases and decreases in voxel intensity during Walk and Stop KI.

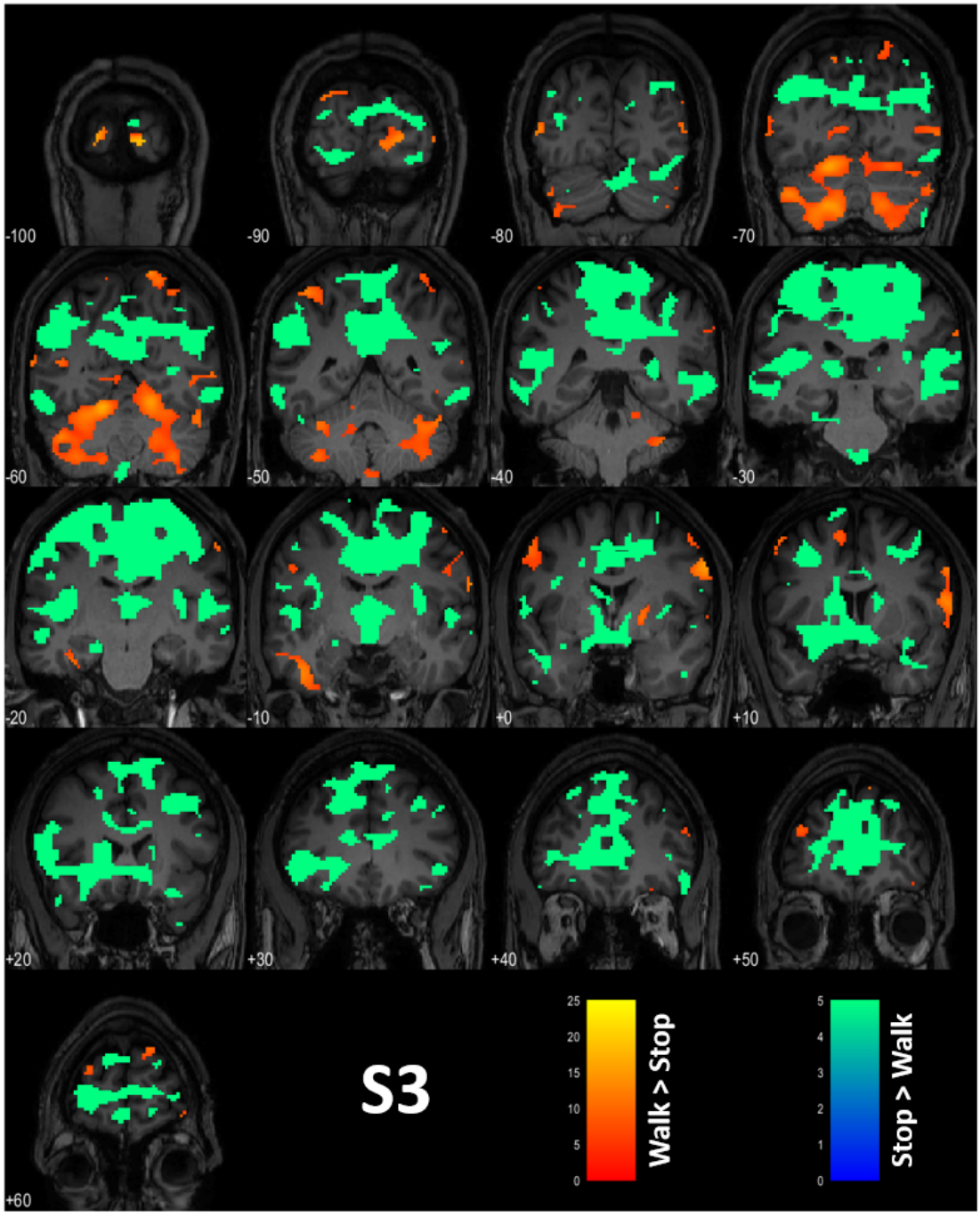

Figure 3.14: Coronal slices of subject S3's T1-weighted structural MRI overlaid with blob contrasts for both significant increases and decreases in voxel intensity during Walk and Stop KI.

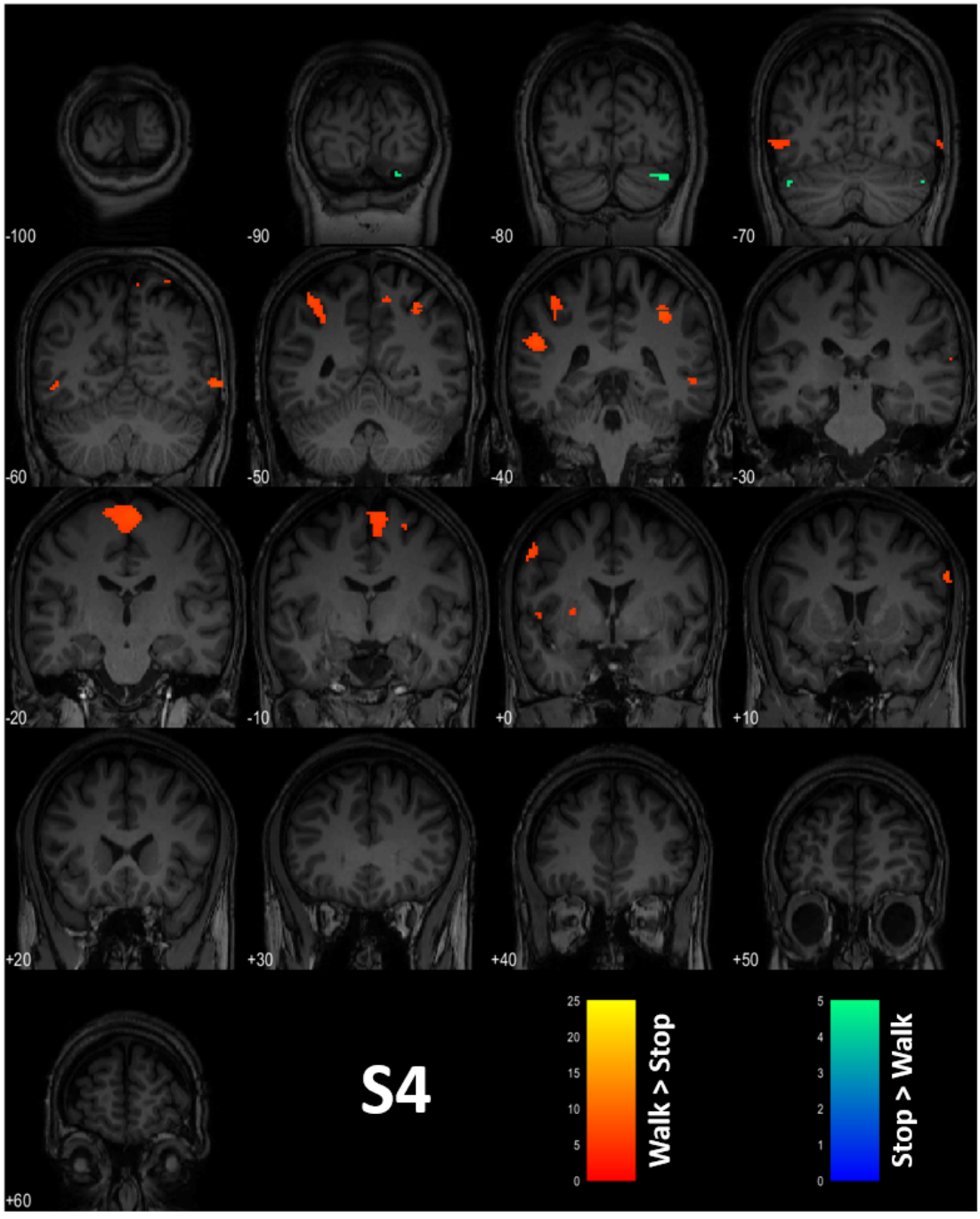

Figure 3.15: Coronal slices of subject S4's T1-weighted structural MRI overlaid with blob contrasts for both significant increases and decreases in voxel intensity during Walk and Stop KI.

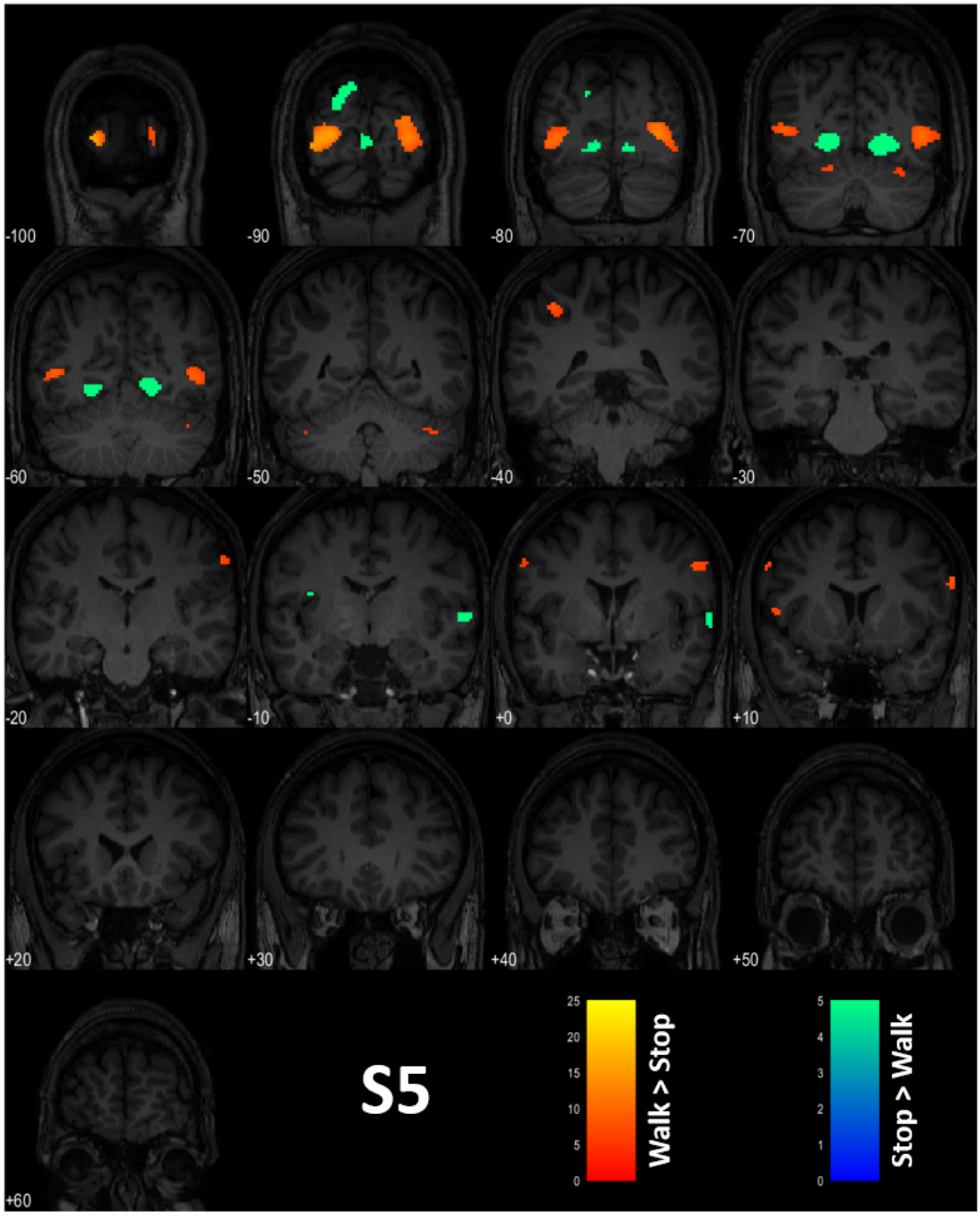

Figure 3.16: Coronal slices of subject S5's T1-weighted structural MRI overlaid with blob contrasts for both significant increases and decreases in voxel intensity during Walk and Stop KI.

Chapter 4

Conclusion

The purpose of this dissertation was to develop a brain-machine interface that detected movement intention from kinesthetic motor imagery to control a lower-limb walking exoskeleton, and to track cortical changes as subjects learned to train their KI over nine longitudinal sessions. In Chapter 1, we presented an overview of how BMI systems hold the potential for restoring movement and mobility for people suffering from paralysis and motor disabilities. In Chapter 2, we developed and evaluated a closed-loop LFDA-GMM decoder to classify Walk and Stop states from windowed δ band EEG, demonstrating robust control in at least three of the subjects by the end of their training. We also tracked how the average EEG feature vector evolved over time, its dependence on classification state, and analyzed various signal statistical measures to identify separation between well- and poorly-classified EEG. In Chapter 3, we looked at the neural correlates underlying the KI of gait from the EEG collected during the training phase of the BMI protocol. We found noteworthy changes in α suppression, prominent ERP and MRCP peaks in response to the cue to switch states, and localized the cortical activity within motor and visual areas of the brain. The work presented in this dissertation contributes to the state-of-the-art in noninvasive BMI systems for control of robotic systems, and furthering our understanding of the representation of gait-related motor imagery in the brain.

So to circle back to the original high-level question of whether individuals can be trained to control a walking exoskeleton with their EEG, and if this can ultimately be a means to restore mobility for the paralyzed population: we proved our hypothesis demonstrating that about half of our able-bodied subjects can be trained to effectively control the exoskeleton with their mental imagery. We identified time-domain and

spectral features that were prominent as the subjects focused on trying to either walk or stop, and how these features track over longitudinal training. And we built upon our knowledge of the cortical mechanisms representing imagination of walking that it may hopefully be used to restore mobility in people with motor disabilities.

References

[1] B. S. Armour, E. A. Courtney-Long, M. H. Fox, H. Fredine, and A. Cahill, "Prevalence and causes of paralysis—United States, 2013," *American Journal of Public Health*, vol. 106, no. 10, pp. 1855–1857, 2016.

[2] National Spinal Cord Injury Statistical Center, "Facts and figures at a glance," *Birmingham, AL: University of Alabama at Birmingham*, 2020.

[3] Christopher & Dana Reeve Foundation. Stats about paralysis. https://www.christopherreeve.org/living-with-paralysis/stats-about-paralysis.

[4] K. K. Ang and C. Guan, "Brain-computer interface in stroke rehabilitation," *Journal of Computing Science and Engineering*, vol. 7, no. 2, pp. 139–146, 6 2013. [Online]. Available: http://koreascience.or.kr/journal/view.jsp?kj=E1EIKI&py=2013&vnc=v7n2&sp=139

[5] D. R. Louie and J. J. Eng, "Powered robotic exoskeletons in post-stroke rehabilitation of gait: A scoping review," *Journal of NeuroEngineering and Rehabilitation*, vol. 13, no. 1, p. 53, 12 2016. [Online]. Available: http://jneuroengrehab.biomedcentral.com/articles/10.1186/s12984-016-0162-5

[6] G. Morone, S. Paolucci, A. Cherubini, D. De Angelis, V. Venturiero, P. Coiro, and M. Iosa, "Robot-assisted gait training for stroke patients: Current state of the art and perspectives of robotics," *Neuropsychiatric Disease and Treatment*, vol. 13, pp. 1303–1311, 2017. [Online]. Available: http://www.ncbi.nlm.nih.gov/pubmed/28553117http://www.pubmedcentral.nih.gov/articlerender.fcgi?artid=PMC5440028

[7] L. J. Holanda, P. M. Silva, T. C. Amorim, M. O. Lacerda, C. R. Simão, and E. Morya, "Robotic assisted gait as a tool for rehabilitation of individuals with spinal cord injury: A systematic review," *Journal of NeuroEngineering*

and Rehabilitation, vol. 14, no. 1, p. 126, 12 2017. [Online]. Available: https://jneuroengrehab.biomedcentral.com/articles/10.1186/s12984-017-0338-7

[8] N. Lapitskaya, J. F. Nielsen, and A. Fuglsang-Frederiksen, "Robotic gait training in patients with impaired consciousness due to severe traumatic brain injury," *Brain Injury*, vol. 25, no. 11, pp. 1070–1079, 10 2011. [Online]. Available: http://www.tandfonline.com/doi/full/10.3109/02699052.2011.607782

[9] J. Wagner, T. Solis-Escalante, P. Grieshofer, C. Neuper, G. Müller-Putz, and R. Scherer, "Level of participation in robotic-assisted treadmill walking modulates midline sensorimotor EEG rhythms in able-bodied subjects," *NeuroImage*, vol. 63, no. 3, pp. 1203–1211, 11 2012. [Online]. Available: https://www.sciencedirect.com/science/article/pii/S1053811912008129

[10] V. Youssofzadeh, D. Zanotto, P. Stegall, M. Naeem, K. Wong-Lin, S. K. Agrawal, and G. Prasad, "Directed neural connectivity changes in robot-assisted gait training: A partial Granger causality analysis," in *2014 36th Annual International Conference of the IEEE Engineering in Medicine and Biology Society, EMBC 2014*. IEEE, 8 2014, pp. 6361–6364. [Online]. Available: http://ieeexplore.ieee.org/document/6945083/

[11] M. M. Danzl, K. C. Chelette, K. Lee, D. Lykins, and L. Sawaki, "Brain stimulation paired with novel locomotor training with robotic gait orthosis in chronic stroke: A feasibility study," *NeuroRehabilitation*, vol. 33, no. 1, pp. 67–76, 1 2013. [Online]. Available: https://content.iospress.com/articles/neurorehabilitation/nre929

[12] A. Picelli, E. Chemello, P. Castellazzi, L. Roncari, A. Waldner, L. Saltuari, and N. Smania, "Combined effects of transcranial direct current stimulation (tDCS) and transcutaneous spinal direct current stimulation (tsDCS) on robot-assisted gait training in patients with chronic stroke: A pilot, double

blind, randomized controlled trial," *Restorative Neurology and Neuroscience*, vol. 33, no. 3, pp. 357–368, 6 2015. [Online]. Available: http://www.medra.org/servlet/aliasResolver?alias=iospress&doi=10.3233/RNN-140474

[13] R. Raithatha, C. Carrico, E. S. Powell, P. M. Westgate, K. C. Chelette, K. Lee, L. Dunsmore, S. Salles, and L. Sawaki, "Non-invasive brain stimulation and robot-assisted gait training after incomplete spinal cord injury: A randomized pilot study," *NeuroRehabilitation*, vol. 38, no. 1, pp. 15–25, 2 2016. [Online]. Available: http://www.medra.org/servlet/aliasResolver?alias=iospress&doi=10.3233/NRE-151291

[14] H. G. Seo, W. H. Lee, S. H. Lee, Y. Yi, K. D. Kim, and B. M. Oh, "Robotic-assisted gait training combined with transcranial direct current stimulation in chronic stroke patients: A pilot double-blind, randomized controlled trial," *Restorative Neurology and Neuroscience*, vol. 35, no. 5, pp. 527–536, 10 2017. [Online]. Available: http://www.medra.org/servlet/aliasResolver?alias=iospress&doi=10.3233/RNN-170745

[15] A. Picelli, E. Chemello, P. Castellazzi, M. Filippetti, A. Brugnera, M. Gandolfi, A. Waldner, L. Saltuari, and N. Smania, "Combined effects of cerebellar transcranial direct current stimulation and transcutaneous spinal direct current stimulation on robot-assisted gait training in patients with chronic brain stroke: A pilot, single blind, randomized controlled trial," *Restorative Neurology and Neuroscience*, vol. 36, no. 2, pp. 161–171, 3 2018. [Online]. Available: http://www.medra.org/servlet/aliasResolver?alias=iospress&doi=10.3233/RNN-170784

[16] "Rex Bionics - Reimagining Rehabilitation, https://www.rexbionics.com/." [Online]. Available: https://www.rexbionics.com/

[17] R. W. Jackson and S. H. Collinsz, "An experimental comparison of the relative

benefits of work and torque assistance in ankle exoskeletons," *Journal of Applied Physiology*, vol. 119, no. 5, pp. 541–557, 9 2015. [Online]. Available: http://www.jappl.org

[18] S. C. Cramer, "Repairing the human brain after stroke. II. Restorative therapies," *Annals of Neurology*, vol. 63, no. 5, pp. 549–560, 5 2008. [Online]. Available: http://www.ncbi.nlm.nih.gov/pubmed/18481291http://doi.wiley.com/10.1002/ana.21412

[19] A. Gharabaghi, "What turns assistive into restorative brain-machine interfaces?" *Frontiers in Neuroscience*, vol. 10, no. OCT, p. 456, 10 2016. [Online]. Available: http://journal.frontiersin.org/article/10.3389/fnins.2016.00456/full

[20] S. K. Banala, S. H. Kim, S. K. Agrawal, and J. P. Scholz, "Robot assisted gait training with active leg exoskeleton (ALEX)," *IEEE Transactions on Neural Systems and Rehabilitation Engineering*, vol. 17, no. 1, pp. 2–8, 2008.

[21] A. Pennycott, D. Wyss, H. Vallery, V. Klamroth-Marganska, and R. Riener, "Towards more effective robotic gait training for stroke rehabilitation: a review," *Journal of NeuroEngineering and Rehabilitation*, vol. 9, no. 1, pp. 1–13, 2012.

[22] A. Jackson and J. B. Zimmermann, "Neural interfaces for the brain and spinal cord—restoring motor function," *Nature Reviews Neurology*, vol. 8, no. 12, p. 690, 2012.

[23] T. Aflalo, S. Kellis, C. Klaes, B. Lee, Y. Shi, K. Pejsa, K. Shanfield, S. Hayes-Jackson, M. Aisen, C. Heck, C. Liu, and R. A. Andersen, "Decoding motor imagery from the posterior parietal cortex of a tetraplegic human," *Science*, vol. 348, no. 6237, pp. 906–910, 2015.

[24] V. Gilja, C. Pandarinath, C. H. Blabe, P. Nuyujukian, J. D. Simeral, A. A. Sarma, B. L. Sorice, J. A. Perge, B. Jarosiewicz, L. R. Hochberg, K. V. Shenoy,

and J. M. Henderson, "Clinical translation of a high-performance neural prosthesis," *Nature Medicine*, vol. 21, no. 10, p. 1142, 2015.

[25] J. L. Collinger, B. Wodlinger, J. E. Downey, W. Wang, E. C. Tyler-Kabara, D. J. Weber, A. J. McMorland, M. Velliste, M. L. Boninger, and A. B. Schwartz, "High-performance neuroprosthetic control by an individual with tetraplegia," *Lancet*, vol. 381, no. 9866, pp. 557–564, 2013.

[26] L. R. Hochberg, D. Bacher, B. Jarosiewicz, N. Y. Masse, J. D. Simeral, J. Vogel, S. Haddadin, J. Liu, S. S. Cash, P. Van Der Smagt, and J. P. Donoghue, "Reach and grasp by people with tetraplegia using a neurally controlled robotic arm," *Nature*, vol. 485, no. 7398, p. 372, 2012.

[27] M. A. Lebedev and M. A. Nicolelis, "Brain–machine interfaces: past, present and future," *TRENDS in Neurosciences*, vol. 29, no. 9, pp. 536–546, 2006.

[28] Y. He, D. Eguren, J. M. Azorín, R. G. Grossman, T. P. Luu, and J. L. Contreras-Vidal, "Brain-machine interfaces for controlling lower-limb powered robotic systems," *Journal of Neural Engineering*, vol. 15, no. 2, p. 021004, 4 2018. [Online]. Available: https://iopscience.iop.org/article/10.1088/1741-2552/aaa8c0

[29] A. R. C. Donati, S. Shokur, E. Morya, D. S. F. Campos, R. C. Moioli, C. M. Gitti, P. B. Augusto, S. Tripodi, C. G. Pires, G. A. Pereira, F. L. Brasil, S. Gallo, A. A. Lin, A. K. Takigami, M. A. Aratanha, S. Joshi, H. Bleuler, G. Cheng, A. Rudolph, and M. A. L. Nicolelis, "Long-term training with a brain-machine interface-based gait protocol induces partial neurological recovery in paraplegic patients," *Scientific Reports*, vol. 6, no. 1, p. 30383, 9 2016. [Online]. Available: http://www.nature.com/articles/srep30383

[30] A. H. Do, P. T. Wang, C. E. King, S. N. Chun, and Z. Nenadic, "Brain-computer interface controlled robotic gait orthosis," *Journal of NeuroEngineering and*

Rehabilitation, vol. 10, no. 1, p. 111, 12 2013. [Online]. Available: http://jneuroengrehab.biomedcentral.com/articles/10.1186/1743-0003-10-111

[31] P. T. Wang, C. E. King, L. A. Chui, A. H. Do, and Z. Nenadic, "Self-paced brain-computer interface control of ambulation in a virtual reality environment," *Journal of Neural Engineering*, vol. 9, no. 5, pp. 1–20, 2012.

[32] G. Pfurtscheller and C. Neuper, "Event-related synchronization of mu rhythm in the EEG over the cortical hand area in man," *Neuroscience Letters*, vol. 174, no. 1, pp. 93–96, 6 1994. [Online]. Available: http://www.ncbi.nlm.nih.gov/pubmed/7970165

[33] B. Rebsamen, E. Burdet, C. Guan, H. Zhang, C. L. Teo, Q. Zeng, M. Ang, and C. Laugier, "A brain-controlled wheelchair based on P300 and path guidance," in *Proceedings of the First IEEE/RAS-EMBS International Conference on Biomedical Robotics and Biomechatronics, 2006, BioRob 2006*, vol. 2006. IEEE, 2006, pp. 1101–1106. [Online]. Available: http://ieeexplore.ieee.org/document/1639239/

[34] T. Lüth, D. Ojdanić, O. Friman, O. Prenzel, and A. Gräser, "Low level control in a semi-autonomous rehabilitation robotic system via a brain-computer interface," in *2007 IEEE 10th International Conference on Rehabilitation Robotics, ICORR'07*. IEEE, 6 2007, pp. 721–728. [Online]. Available: http://ieeexplore.ieee.org/document/4428505/

[35] I. Iturrate, J. M. Antelis, A. Kübler, and J. Minguez, "A noninvasive brain-actuated wheelchair based on a P300 neurophysiological protocol and automated navigation," *IEEE Transactions on Robotics*, vol. 25, no. 3, pp. 614–627, 6 2009. [Online]. Available: http://ieeexplore.ieee.org/document/4914843/

[36] M. Palankar, K. J. De Laurentis, R. Alqasemi, E. Veras, R. Dubey, Y. Arbel, and E. Donchin, "Control of a 9-DoF wheelchair-mounted

robotic arm system using a P300 brain computer interface: Initial experiments," in *2008 IEEE International Conference on Robotics and Biomimetics, ROBIO 2008*. IEEE, 2 2008, pp. 348–353. [Online]. Available: http://ieeexplore.ieee.org/document/4913028/

[37] E. Donchin and Y. Arbel, "P300 based brain computer interfaces: A progress report," in *Lecture Notes in Computer Science (including subseries Lecture Notes in Artificial Intelligence and Lecture Notes in Bioinformatics)*. Springer, Berlin, Heidelberg, 2009, vol. 5638 LNAI, pp. 724–731. [Online]. Available: http://link.springer.com/10.1007/978-3-642-02812-0_82

[38] G. D. Johnson, N. R. Waytowich, D. J. Cox, and D. J. Krusienski, "Extending the discrete selection capabilities of the P300 Speller to goal-oriented robotic arm control," in *2010 3rd IEEE RAS and EMBS International Conference on Biomedical Robotics and Biomechatronics, BioRob 2010*. IEEE, 9 2010, pp. 572–575. [Online]. Available: http://ieeexplore.ieee.org/lpdocs/epic03/wrapper.htm?arnumber=5628039

[39] C. J. Bell, P. Shenoy, R. Chalodhorn, and R. P. Rao, "Control of a humanoid robot by a noninvasive brain-computer interface in humans," *Journal of Neural Engineering*, vol. 5, no. 2, pp. 214–220, 6 2008. [Online]. Available: http://stacks.iop.org/1741-2552/5/i=2/a=012?key=crossref.37b71955383d6099dfe834692fda5f11

[40] N. A. Fitzsimmons, M. A. Lebedev, I. D. Peikon, and M. A. L. Nicolelis, "Extracting kinematic parameters for monkey bipedal walking from cortical neuronal ensemble activity." *Frontiers in Integrative Neuroscience*, vol. 3, no. March, p. 3, 2009.

[41] A. Presacco, R. Goodman, L. Forrester, and J. L. Contreras-Vidal, "Neural decoding of treadmill walking from noninvasive electroencephalographic

signals," *Journal of Neurophysiology*, vol. 106, no. 4, pp. 1875–1887, 10 2011. [Online]. Available: http://www.physiology.org/doi/10.1152/jn.00104.2011

[42] M. Bakker, F. P. De Lange, J. A. Stevens, I. Toni, and B. R. Bloem, "Motor imagery of gait: A quantitative approach," *Experimental Brain Research*, vol. 179, no. 3, pp. 497–504, 5 2007. [Online]. Available: http://www.ncbi.nlm.nih.gov/pubmed/17211663http://link.springer.com/10.1007/s00221-006-0807-x

[43] S. C. Cramer, L. Lastra, M. G. Lacourse, and M. J. Cohen, "Brain motor system function after chronic, complete spinal cord injury," *Brain*, vol. 128, no. 12, pp. 2941–2950, 12 2005. [Online]. Available: http://www.ncbi.nlm.nih.gov/pubmed/16246866http://academic.oup.com/brain/article/128/12/2941/420486/Brain-motor-system-function-after-chronic-complete

[44] Y. He, K. Nathan, A. Venkatakrishnan, R. Rovekamp, C. Beck, R. Ozdemir, G. E. Francisco, and J. L. Contreras-Vidal, "An integrated neuro-robotic interface for stroke rehabilitation using the NASA X1 powered lower limb exoskeleton," in *2014 36th Annual International Conference of the IEEE Engineering in Medicine and Biology Society, EMBC 2014*. IEEE, 8 2014, pp. 3985–3988. [Online]. Available: http://ieeexplore.ieee.org/document/6944497/

[45] J. L. Contreras-Vidal, M. Bortole, F. Zhu, K. Nathan, A. Venkatakrishnan, G. E. Francisco, R. Soto, and J. L. Pons, "Neural decoding of robot-assisted gait during rehabilitation after stroke," *American Journal of Physical Medicine and Rehabilitation*, vol. 97, no. 8, pp. 541–550, 2018.

[46] Y. He, T. P. Luu, K. Nathan, S. Nakagome, and J. L. Contreras-Vidal, "A mobile brainbody imaging dataset recorded during treadmill walking with a brain-computer interface," *Scientific Data*, vol. 5, no. 1, pp. 1–10, 4 2018. [Online]. Available: www.nature.com/sdata/

[47] T. P. Luu, Y. He, S. Brown, S. Nakagome, and J. L. Contreras-Vidal, "A closed-loop brain computer interface to a virtual reality avatar: Gait adaptation to visual kinematic perturbations," *International Conference on Virtual Rehabilitation*, vol. 2015, pp. 30–37, 6 2015. [Online]. Available: http://www.ncbi.nlm.nih.gov/pubmed/27713915http://www.pubmedcentral.nih.gov/articlerender.fcgi?artid=PMC5048680

[48] T. P. Luu, Y. He, S. Brown, S. Nakagome, and J. Contreras-Vidal, "Gait adaptation to visual kinematic perturbations using a real-time closed-loop brain-computer interface to a virtual reality avatar," *Journal of Neural Engineering*, vol. 13, no. 3, p. 36006, 2016.

[49] K. Gui, H. Liu, and D. Zhang, "Toward multimodal human-robot interaction to enhance active participation of users in gait rehabilitation," *IEEE Transactions on Neural Systems and Rehabilitation Engineering*, vol. 25, no. 11, pp. 2054–2066, 2017.

[50] A. Kilicarslan, S. Prasad, R. G. Grossman, and J. L. Contreras-Vidal, "High accuracy decoding of user intentions using EEG to control a lower-body exoskeleton," *Proceedings of the Annual International Conference of the IEEE Engineering in Medicine and Biology Society, EMBS*, pp. 5606–5609, 2013.

[51] A. Kilicarslan, R. G. Grossman, and J. L. Contreras-Vidal, "A robust adaptive denoising framework for real-time artifact removal in scalp EEG measurements," *Journal of Neural Engineering*, vol. 13, no. 2, p. 026013, 4 2016. [Online]. Available: http://stacks.iop.org/1741-2552/13/i=2/a=026013?key=crossref.9a4f5a0f498daf56c652b097daf59baa

[52] E. López-Larraz, F. Trincado-Alonso, V. Rajasekaran, S. Pérez-Nombela, A. J. Del-Ama, J. Aranda, J. Minguez, A. Gil-Agudo, and L. Montesano, "Control of an ambulatory exoskeleton with a brain–machine interface for spinal cord

injury gait rehabilitation," *Frontiers in Neuroscience*, vol. 10, p. 359, 8 2016. [Online]. Available: http://journal.frontiersin.org/Article/10.3389/fnins.2016.00359/abstract

[53] V. Rajasekaran, E. López-larraz, F. Trincado-alonso, J. Aranda, L. Montesano, J. Antonio, and J. L. Pons, "Volition-adaptive control for gait training using wearable exoskeleton: preliminary tests with incomplete spinal cord injury individuals," *Journal of NeuroEngineering and Rehabilitation*, pp. 1–15, 2018.

[54] M. Rodríguez-Ugarte, E. Iáñez, M. Ortiz, and J. M. Azorín, "Improving real-time lower limb motor imagery detection using tDCS and an exoskeleton," *Frontiers in Neuroscience*, vol. 12, no. October, p. 757, 2018.

[55] D. Liu, W. Chen, Z. Pei, and J. Wang, "A brain-controlled lower-limb exoskeleton for human gait training," *Review of Scientific Instruments*, vol. 88, no. 10, 2017.

[56] E. García-Cossio, M. Severens, B. Nienhuis, J. Duysens, P. Desain, N. Keijsers, and J. Farquhar, "Decoding sensorimotor rhythms during robotic-assisted treadmill walking for brain computer interface (BCI) applications," *PLOS One*, vol. 10, no. 12, p. e0137910, 12 2015. [Online]. Available: http://dx.plos.org/10.1371/journal.pone.0137910

[57] X. Zhang, G. Xu, I. Member, J. Xie, I. Member, M. Li, I. Member, and W. Pei, "An EEG-driven lower limb rehabilitation training system for active and passive co-stimulation," *2015 37th Annual International Conference of the IEEE Engineering in Medicine and Biology Society (EMBC)*, pp. 4582–4585, 2015.

[58] N.-S. Kwak, K.-R. Müller, and S.-W. Lee, "A lower limb exoskeleton control system based on steady state visual evoked potentials," *Journal of Neural Engineering*, vol. 12, no. 5, p. 056009, 10 2015. [Online].

Available: http://stacks.iop.org/1741-2552/12/i=5/a=056009?key=crossref.d574e38494295e53b491abb83540a57c

[59] N. S. Kwak, K. R. Müller, and S. W. Lee, "A convolutional neural network for steady state visual evoked potential classification under ambulatory environment," *PLOS One*, vol. 12, no. 2, pp. 1–20, 2017.

[60] K. Lee, D. Liu, L. Perroud, R. Chavarriaga, and J. d. R. Millán, "A brain-controlled exoskeleton with cascaded event-related desynchronization classifiers," *Robotics and Autonomous Systems*, vol. 90, pp. 15–23, 4 2017. [Online]. Available: https://www.sciencedirect.com/science/article/pii/S0921889016304948?via%3Dihub

[61] Y. Zhang, S. Prasad, A. Kilicarslan, and J. L. Contreras-Vidal, "Multiple kernel based region importance learning for neural classification of gait states from EEG signals," *Frontiers in Neuroscience*, vol. 11, no. APR, p. 170, 4 2017. [Online]. Available: http://journal.frontiersin.org/article/10.3389/fnins.2017.00170/full

[62] J. L. Contreras-Vidal and R. G. Grossman, "NeuroRex: A clinical neural interface roadmap for EEG-based brain machine interfaces to a lower body robotic exoskeleton," in *Proceedings of the Annual International Conference of the IEEE Engineering in Medicine and Biology Society, EMBS*. IEEE, 7 2013, pp. 1579–1582. [Online]. Available: http://ieeexplore.ieee.org/document/6609816/

[63] J. A. Brantley, T. P. Luu, S. Nakagome, F. Zhu, and J. L. Contreras-Vidal, "Full body mobile brain-body imaging data during unconstrained locomotion on stairs, ramps, and level ground," *Scientific Data*, vol. 5, p. 180133, 2018. [Online]. Available: https://doi.org/10.1038/sdata.2018.133

[64] M. Eimer, "Effects of attention and stimulus probability on ERPs in a Go/Nogo task," *Biological Psychology*, vol. 35, no. 2, pp. 123–138, 1993.

[65] P. L. Enright, "The six-minute walk test," *Respiratory Care*, vol. 48, no. 8, pp. 783–785, 2003.

[66] H. H. Jasper, "The ten-twenty electrode system of the international federation," *Electroencephalogr. Clin. Neurophysiol.*, vol. 10, pp. 370–375, 1958. [Online]. Available: https://ci.nii.ac.jp/naid/10017996828/

[67] T. Nguyen, T. Potter, C. Karmonik, R. Grossman, and Y. Zhang, "Concurrent EEG and functional MRI recording and integration analysis for dynamic cortical activity imaging," *JoVE (Journal of Visualized Experiments)*, no. 136, p. e56417, 2018.

[68] M. Sugiyama, "Dimensionality reduction of multimodal labeled data by local fisher discriminant analysis," *Journal of Machine Learning Research*, vol. 8, pp. 1027–1061, 2007. [Online]. Available: http://sugiyama-www.cs.titech.ac.jp/

[69] W. Li, S. Prasad, J. E. Fowler, and L. M. Bruce, "Locality-preserving dimensionality reduction and classification for hyperspectral image analysis," *IEEE Transactions on Geoscience and Remote Sensing*, vol. 50, no. 4, pp. 1185–1198, 2011.

[70] B. Hjorth, "EEG analysis based on time domain properties," *Electroencephalography and Clinical Neurophysiology*, vol. 29, no. 3, pp. 306–310, 1970.

[71] B. H. Brinkmann, J. Wagenaar, D. Abbot, P. Adkins, S. C. Bosshard, M. Chen, Q. M. Tieng, J. He, F. Muñoz-Almaraz, P. Botella-Rocamora, J. Pardo, F. Zamora-Martinez, M. Hills, W. Wu, I. Korshunova, W. Cukierski, C. Vite, E. E. Patterson, B. Litt, and G. A. Worrell, "Crowdsourcing reproducible seizure forecasting in human and canine epilepsy," *Brain*, vol. 139, no. 6, pp. 1713–1722, 2016.

[72] M. Misiti, Y. Misiti, G. Oppenheim, and J.-M. Poggi, "Wavelet toolbox," *The MathWorks Inc., Natick, MA*, vol. 15, p. 21, 1996.

[73] M. Cukic, D. Pokrajac, M. Stokic, V. Radivojevic, and M. Ljubisavljevic, "EEG machine learning with Higuchi fractal dimension and sample entropy as features for successful detection of depression," *arXiv preprint arXiv:1803.05985*, 2018.

[74] M. Allen, D. Poggiali, K. Whitaker, T. R. Marshall, and R. A. Kievit, "Raincloud plots: a multi-platform tool for robust data visualization," *Wellcome Open Research*, vol. 4, 2019.

[75] G. Pfurtscheller and T. Solis-Escalante, "Could the beta rebound in the EEG be suitable to realize a "brain switch"?" *Clinical Neurophysiology*, vol. 120, no. 1, pp. 24–29, 2009.

[76] T. P. Luu, S. Nakagome, Y. He, and J. L. Contreras-Vidal, "Real-time EEG-based brain-computer interface to a virtual avatar enhances cortical involvement in human treadmill walking," *Scientific Reports*, vol. 7, no. 1, p. 8895, 2017. [Online]. Available: https://doi.org/10.1038/s41598-017-09187-0http://www.nature.com/articles/s41598-017-09187-0.pdf

[77] T. P. Luu, Y. He, S. Nakagome, K. Nathan, S. Brown, J. Gorges, and J. L. Contreras-Vidal, "Multi-trial gait adaptation of healthy individuals during visual kinematic perturbations," *Frontiers in Human Neuroscience*, vol. 11, p. 320, 6 2017. [Online]. Available: http://journal.frontiersin.org/article/10.3389/fnhum.2017.00320/full

[78] K. Nathan and J. L. Contreras-Vidal, "Negligible motion artifacts in scalp electroencephalography (EEG) during treadmill walking," *Frontiers in Human Neuroscience*, vol. 9, p. 708, 2016. [Online]. Available: http://www.ncbi.nlm.nih.gov/pubmed/26793089http://www.pubmedcentral.nih.gov/articlerender.fcgi?artid=PMC4710850

[79] T. R. Mullen, C. A. Kothe, Y. M. Chi, A. Ojeda, T. Kerth, S. Makeig, T. P. Jung, and G. Cauwenberghs, "Real-time neuroimaging and cognitive monitoring using wearable dry EEG," *IEEE Trans. Biomed. Eng.*, vol. 62, no. 11, pp. 2553–67, 2015.

[80] C. Chang, S. Hsu, L. Pion-Tonachini, and T. Jung, "Evaluation of artifact subspace reconstruction for automatic artifact components removal in multi-channel EEG recordings," *IEEE Trans. Biomed. Eng.*, pp. 1–1, 2019.

[81] A. S. Oliveira, B. R. Schlink, W. D. Hairston, P. König, and D. P. Ferris, "Induction and separation of motion artifacts in EEG data using a mobile phantom head device," *J. Neural Eng.*, vol. 13, no. 3, p. 036014, 2016. [Online]. Available: http://dx.doi.org/10.1088/1741-2560/13/3/036014

[82] A. Kilicarslan and J. L. Contreras Vidal, "Characterization and real-time removal of motion artifacts from EEG signals," *J. Neural Eng.*, vol. 16, no. 5, p. 056027, 2019. [Online]. Available: http://dx.doi.org/10.1088/1741-2552/ab2b61

[83] A. Guillot, C. Collet, V. A. Nguyen, F. Malouin, C. Richards, and J. Doyon, "Brain activity during visual versus kinesthetic imagery: an fMRI study," *Human Brain Mapping*, vol. 30, no. 7, pp. 2157–2172, 2009.

[84] W. X. Yao, V. K. Ranganathan, D. Allexandre, V. Siemionow, and G. H. Yue, "Kinesthetic imagery training of forceful muscle contractions increases brain signal and muscle strength," *Frontiers in Human Neuroscience*, vol. 7, p. 561, 2013.

[85] C. Frith and R. J. Dolan, "Brain mechanisms associated with top-down processes in perception," *Philosophical Transactions of the Royal Society of London. Series B: Biological Sciences*, vol. 352, no. 1358, pp. 1221–1230, 1997.

[86] V. K. Ranganathan, V. Siemionow, J. Z. Liu, V. Sahgal, and G. H. Yue, "From

mental power to muscle power—gaining strength by using the mind," *Neuropsychologia*, vol. 42, no. 7, pp. 944–956, 2004.

[87] J. Decety, M. Jeannerod, M. Germain, and J. Pastene, "Vegetative response during imagined movement is proportional to mental effort," *Behavioural Brain Research*, vol. 42, no. 1, pp. 1–5, 1991.

[88] F. Lebon, C. Collet, and A. Guillot, "Benefits of motor imagery training on muscle strength," *The Journal of Strength & Conditioning Research*, vol. 24, no. 6, pp. 1680–1687, 2010.

[89] G. Yue and K. J. Cole, "Strength increases from the motor program: comparison of training with maximal voluntary and imagined muscle contractions," *Journal of Neurophysiology*, vol. 67, no. 5, pp. 1114–1123, 1992.

[90] D. M. Landers, "The effects of mental practice on motor skill learning and performance: A meta-analysis." *Journal of Sport Psychology*, vol. 5, no. 1, 1983.

[91] B. Mumford and C. Hall, "The effects of internal and external imagery on performing figures in figure skating." *Canadian Journal of Applied Sport Sciences*, vol. 10, no. 4, pp. 171–177, 1985.

[92] R. Gentili, C. E. Han, N. Schweighofer, and C. Papaxanthis, "Motor learning without doing: trial-by-trial improvement in motor performance during mental training," *Journal of Neurophysiology*, vol. 104, no. 2, pp. 774–783, 2010.

[93] W. Kim, Y. Chang, J. Kim, J. Seo, K. Ryu, E. Lee, M. Woo, and C. M. Janelle, "An fMRI study of differences in brain activity among elite, expert, and novice archers at the moment of optimal aiming," *Cognitive and Behavioral Neurology*, vol. 27, no. 4, pp. 173–182, 2014.

[94] A. Pascual-Leone, D. Nguyet, L. G. Cohen, J. P. Brasil-Neto, A. Cammarota,

and M. Hallett, "Modulation of muscle responses evoked by transcranial magnetic stimulation during the acquisition of new fine motor skills," *Journal of Neurophysiology*, vol. 74, no. 3, pp. 1037–1045, 1995.

[95] R. Roure, C. Collet, C. Deschaumes-Molinaro, A. Dittmar, H. Rada, G. Delhomme, and E. Vernet-Maury, "Autonomic nervous system responses correlate with mental rehearsal in volleyball training," *European Journal of Applied Physiology and Occupational Physiology*, vol. 78, no. 2, pp. 99–108, 1998.

[96] J.-S. Kim, D.-W. Oh, S.-Y. Kim, and J.-D. Choi, "Visual and kinesthetic locomotor imagery training integrated with auditory step rhythm for walking performance of patients with chronic stroke," *Clinical Rehabilitation*, vol. 25, no. 2, pp. 134–145, 2011.

[97] S. M. Braun, A. J. Beurskens, S. M. Van Kroonenburgh, J. Demarteau, J. M. Schols, and D. T. Wade, "Effects of mental practice embedded in daily therapy compared to therapy as usual in adult stroke patients in dutch nursing homes: design of a randomised controlled trial," *BMC Neurology*, vol. 7, no. 1, pp. 1–13, 2007.

[98] A. Zimmermann-Schlatter, C. Schuster, M. A. Puhan, E. Siekierka, and J. Steurer, "Efficacy of motor imagery in post-stroke rehabilitation: a systematic review," *Journal of NeuroEngineering and Rehabilitation*, vol. 5, no. 1, pp. 1–10, 2008.

[99] B. H. Dobkin, "Brain–computer interface technology as a tool to augment plasticity and outcomes for neurological rehabilitation," *The Journal of Physiology*, vol. 579, no. 3, pp. 637–642, 2007.

[100] V. Kaiser, G. Bauernfeind, A. Kreilinger, T. Kaufmann, A. Kübler, C. Neuper, and G. R. Müller-Putz, "Cortical effects of user training in a motor imagery

based brain–computer interface measured by fNIRS and EEG," *NeuroImage*, vol. 85, pp. 432–444, 2014.

[101] N. Mrachacz-Kersting, S. R. Kristensen, I. K. Niazi, and D. Farina, "Precise temporal association between cortical potentials evoked by motor imagination and afference induces cortical plasticity," *The Journal of Physiology*, vol. 590, no. 7, pp. 1669–1682, 2012.

[102] C. M. Stinear, W. D. Byblow, M. Steyvers, O. Levin, and S. P. Swinnen, "Kinesthetic, but not visual, motor imagery modulates corticomotor excitability," *Experimental Brain Research*, vol. 168, no. 1-2, pp. 157–164, 2006.

[103] G. Allali, M. Van Der Meulen, O. Beauchet, S. W. Rieger, P. Vuilleumier, and F. Assal, "The neural basis of age-related changes in motor imagery of gait: An fMRI study," *Journals of Gerontology - Series A Biological Sciences and Medical Sciences*, vol. 69, no. 11, pp. 1389–1398, 8 2014.

[104] C. Neuper, R. Scherer, M. Reiner, and G. Pfurtscheller, "Imagery of motor actions: Differential effects of kinesthetic and visual–motor mode of imagery in single-trial EEG," *Cognitive Brain Research*, vol. 25, no. 3, pp. 668–677, 2005.

[105] C. La Fougere, A. Zwergal, A. Rominger, S. Förster, G. Fesl, M. Dieterich, T. Brandt, M. Strupp, P. Bartenstein, and K. Jahn, "Real versus imagined locomotion: a [18F]-FDG PET-fMRI comparison," *NeuroImage*, vol. 50, no. 4, pp. 1589–1598, 2010.

[106] P. Dechent, K.-D. Merboldt, and J. Frahm, "Is the human primary motor cortex involved in motor imagery?" *Cognitive Brain Research*, vol. 19, no. 2, pp. 138–144, 2004.

[107] F. Lebon, U. Horn, M. Domin, and M. Lotze, "Motor imagery training: kinesthetic imagery strategy and inferior parietal fMRI activation," *Human Brain Mapping*, vol. 39, no. 4, pp. 1805–1813, 2018.

[108] M. Jeannerod, "Neural simulation of action: a unifying mechanism for motor cognition," *NeuroImage*, vol. 14, no. 1, pp. S103–S109, 2001.

[109] N. Sharma and J. C. Baron, "Does motor imagery share neural networks with executed movement: A multivariate fMRI analysis," *Frontiers in Human Neuroscience*, vol. 7, no. SEP, p. 564, 9 2013.

[110] A. Sirigu, J.-R. Duhamel, L. Cohen, B. Pillon, B. Dubois, and Y. Agid, "The mental representation of hand movements after parietal cortex damage," *Science*, vol. 273, no. 5281, pp. 1564–1568, 1996.

[111] B. Suchan, L. Yágüez, G. Wunderlich, A. G. Canavan, H. Herzog, L. Tellmann, V. Hömberg, and R. J. Seitz, "Neural correlates of visuospatial imagery," *Behavioural Brain Research*, vol. 131, no. 1-2, pp. 163–168, 2002.

[112] M. Tariq, P. M. Trivailo, and M. Simic, "Mu-beta event-related (de) synchronization and EEG classification of left-right foot dorsiflexion kinaesthetic motor imagery for BCI," *PLOS One*, vol. 15, no. 3, p. e0230184, 2020.

[113] M. Labriffe, C. Annweiler, L. E. Amirova, G. Gauquelin-Koch, A. Ter Minassian, L.-M. Leiber, O. Beauchet, M.-A. Custaud, and M. Dinomais, "Brain activity during mental imagery of gait versus gait-like plantar stimulation: a novel combined functional MRI paradigm to better understand cerebral gait control," *Frontiers in Human Neuroscience*, vol. 11, p. 106, 2017.

[114] K. Jahn, A. Deutschländer, T. Stephan, M. Strupp, M. Wiesmann, and T. Brandt, "Brain activation patterns during imagined stance and locomotion in functional magnetic resonance imaging," *NeuroImage*, vol. 22, no. 4, pp. 1722–1731, 2004.

[115] D. J. Clark, "Automaticity of walking: functional significance, mechanisms, measurement and rehabilitation strategies," *Frontiers in Human Neuroscience*, vol. 9, p. 246, 2015.

[116] D. Hamacher, F. Herold, P. Wiegel, D. Hamacher, and L. Schega, "Brain activity during walking: a systematic review," *Neuroscience & Biobehavioral Reviews*, vol. 57, pp. 310–327, 2015.

[117] C. Reynolds, B. A. Osuagwu, and A. Vuckovic, "Influence of motor imagination on cortical activation during functional electrical stimulation," *Clinical Neurophysiology*, vol. 126, no. 7, pp. 1360–1369, 7 2015. [Online]. Available: http://www.sciencedirect.com/science/article/pii/S1388245714005392

[118] G. Pfurtscheller and F. L. Da Silva, "Event-related EEG/MEG synchronization and desynchronization: basic principles," *Clinical Neurophysiology*, vol. 110, no. 11, pp. 1842–1857, 1999.

[119] P. Suffczynski, "Event-related dynamics of alpha band rhythms: a neuronal network model of focal ERD/surround ERS," *Event-Related Desynchronization: Handbook of Electroencephalography and Clinical Neurophysiology*, vol. 6, pp. 67–85, 1999.

[120] G. Pfurtscheller, T. Solis-Escalante, R. Ortner, P. Linortner, and G. R. Muller-Putz, "Self-paced operation of an SSVEP-Based orthosis with and without an imagery-based "brain switch:" a feasibility study towards a hybrid BCI," *IEEE Transactions on Neural Systems and Rehabilitation Engineering*, vol. 18, no. 4, pp. 409–414, 2010.

[121] M. Gregg, C. Hall, and A. Butler, "The MIQ-RS: a suitable option for examining movement imagery ability," *Evidence-Based Complementary and Alternative Medicine*, vol. 7, no. 2, pp. 249–257, 2010.

[122] A. Delorme and S. Makeig, "EEGLAB: an open source toolbox for analysis of single-trial EEG dynamics including independent component analysis," *J. Neurosci. Methods*, vol. 134, no. 1, pp. 9–21, 2004. [Online]. Available: http://ac.els-cdn.com/S0165027003003479/1-s2.0-S0165027003003479-main.

pdf?_tid=6a419c2c-d408-11e4-acc4-00000aab0f6b&acdnat=1427409513_9dc35cac3fbe42e120d6ebef54bfb8e9

[123] R. Oostenveld, P. Fries, E. Maris, and J.-M. Schoffelen, "FieldTrip: open source software for advanced analysis of MEG, EEG, and invasive electrophysiological data," *Comput. Intell. Neurosci.*, vol. 2011, p. 9, 2011. [Online]. Available: http://dx.doi.org/10.1155/2011/156869

[124] J. A. Palmer, K. Kreutz-Delgado, and S. Makeig, "AMICA: An adaptive mixture of independent component analyzers with shared components," *Swartz Center for Computatonal Neursoscience, University of California San Diego, Tech. Rep*, 2012.

[125] A. Delorme, J. Palmer, J. Onton, R. Oostenveld, and S. Makeig, "Independent eeg sources are dipolar," *PloS one*, vol. 7, no. 2, p. e30135, 2012.

[126] V. Fonov, A. C. Evans, K. Botteron, C. R. Almli, R. C. McKinstry, and D. L. Collins, "Unbiased average age-appropriate atlases for pediatric studies," *NeuroImage*, vol. 54, no. 1, pp. 313–27, 2011.

[127] C. Piazza, M. Miyakoshi, Z. Akalin-Acar, C. Cantiani, G. Reni, A. M. Bianchi, and S. Makeig, "An automated function for identifying EEG independent components representing bilateral source activity," in *XIV Mediterranean Conference on Medical and Biological Engineering and Computing 2016*. Springer, 2016, pp. 105–109.

[128] L. Pion-Tonachini, K. Kreutz-Delgado, and S. Makeig, "Iclabel: An automated electroencephalographic independent component classifier, dataset, and website," *NeuroImage*, vol. 198, pp. 181–197, 2019.

[129] J. Ashburner, G. Barnes, C.-C. Chen, J. Daunizeau, G. Flandin, K. Friston, S. Kiebel, J. Kilner, V. Litvak, R. Moran, W. Penny, A. Razi, K. Stephan,

S. Tak, P. Zeidman, D. Gitelman, R. Henson, C. Hutton, V. Glauche, J. Mattout, and C. Phillips, "SPM12 manual," *Wellcome Trust Centre for Neuroimaging, London, UK*, vol. 2464, 2014.

[130] G. Pfurtscheller, C. Brunner, A. Schlögl, and F. H. Lopes da Silva, "Mu rhythm (de)synchronization and EEG single-trial classification of different motor imagery tasks," *NeuroImage*, vol. 31, no. 1, pp. 153–159, 5 2006. [Online]. Available: http://www.ncbi.nlm.nih.gov/pubmed/16443377http://linkinghub.elsevier.com/retrieve/pii/S1053811905025140

[131] N. A. Bhagat, A. Venkatakrishnan, B. Abibullaev, E. J. Artz, N. Yozbatiran, A. A. Blank, J. French, C. Karmonik, R. G. Grossman, M. K. O'Malley, G. E. Francisco, and J. L. Contreras-Vidal, "Design and optimization of an EEG-based brain machine interface (BMI) to an upper-limb exoskeleton for stroke survivors," *Frontiers in Neuroscience*, vol. 10, no. MAR, 3 2016. [Online]. Available: http://journal.frontiersin.org/Article/10.3389/fnins.2016.00122/abstract

[132] D. J. McFarland, L. M. McCane, S. V. David, and J. R. Wolpaw, "Spatial filter selection for EEG-based communication," *Electroencephalography and Clinical Neurophysiology*, vol. 103, no. 3, pp. 386–394, 1997.

[133] H. Shibasaki and M. Hallett, "What is the Bereitschaftspotential?" *Clinical Neurophysiology*, vol. 117, no. 11, pp. 2341–2356, 11 2006. [Online]. Available: https://www.sciencedirect.com/science/article/pii/S138824570600229X?via%3Dihub

[134] I. Miyai, H. C. Tanabe, I. Sase, H. Eda, I. Oda, I. Konishi, Y. Tsunazawa, T. Suzuki, T. Yanagida, and K. Kubota, "Cortical mapping of gait in humans: a near-infrared spectroscopic topography study," *NeuroImage*, vol. 14, no. 5, pp. 1186–1192, 2001.

[135] F. Malouin, C. L. Richards, P. L. Jackson, M. F. Lafleur, A. Durand, and J. Doyon, "The Kinesthetic and Visual Imagery Questionnaire (KVIQ) for assessing motor imagery in persons with physical disabilities: a reliability and construct validity study," *Journal of Neurologic Physical Therapy*, vol. 31, no. 1, pp. 20–29, 2007.

[136] W. Sato, T. Kochiyama, S. Uono, K. Matsuda, K. Usui, N. Usui, Y. Inoue, and M. Toichi, "Bidirectional electric communication between the inferior occipital gyrus and the amygdala during face processing," *Human Brain Mapping*, vol. 38, no. 9, pp. 4511–4524, 2017.

[137] C. Jacques, J. Jonas, L. Maillard, S. Colnat-Coulbois, L. Koessler, and B. Rossion, "The inferior occipital gyrus is a major cortical source of the face-evoked N170: Evidence from simultaneous scalp and intracerebral human recordings," *Human Brain Mapping*, vol. 40, no. 5, pp. 1403–1418, 2019.

[138] Z. Zhen, H. Fang, and J. Liu, "The hierarchical brain network for face recognition," *PLOS One*, vol. 8, no. 3, p. e59886, 2013.

[139] Y.-Y. Wai, J.-J. Wang, Y.-H. Weng, W.-Y. Lin, H.-K. Ma, S.-H. Ng, Y.-L. Wan, and C.-H. Wang, "Cortical involvement in a gait-related imagery task: comparison between Parkinson's disease and normal aging," *Parkinsonism & Related Disorders*, vol. 18, no. 5, pp. 537–542, 2012.

[140] M. Van Der Meulen, G. Allali, S. W. Rieger, F. Assal, and P. Vuilleumier, "The influence of individual motor imagery ability on cerebral recruitment during gait imagery," *Human brain mapping*, vol. 35, no. 2, pp. 455–470, 2014.

[141] P. Fransson and G. Marrelec, "The precuneus/posterior cingulate cortex plays a pivotal role in the default mode network: Evidence from a partial correlation network analysis," *NeuroImage*, vol. 42, no. 3, pp. 1178–1184, 2008.

[142] A. V. Utevsky, D. V. Smith, and S. A. Huettel, "Precuneus is a functional core of the default-mode network," *Journal of Neuroscience*, vol. 34, no. 3, pp. 932–940, 2014.

[143] J. L. Smith, S. Jamadar, A. L. Provost, and P. T. Michie, "Motor and non-motor inhibition in the Go/NoGo task: an ERP and fMRI study," *International Journal of Psychophysiology*, vol. 87, no. 3, pp. 244–253, 2013.

[144] S. Galdo-Alvarez, F. M. Bonilla, A. J. González-Villar, and M. T. Carrillo-de-la Peña, "Functional equivalence of imagined vs. real performance of an inhibitory task: an EEG/ERP study," *Frontiers in Human Neuroscience*, vol. 10, p. 467, 2016.

[145] R. Caldara, M.-P. Deiber, C. Andrey, C. M. Michel, G. Thut, and C.-A. Hauert, "Actual and mental motor preparation and execution: a spatiotemporal ERP study," *Experimental Brain Research*, vol. 159, no. 3, pp. 389–399, 2004.

[146] H. G. Vaughan Jr and W. Ritter, "The sources of auditory evoked responses recorded from the human scalp," *Electroencephalography and Clinical Neurophysiology*, vol. 28, no. 4, pp. 360–367, 1970.

[147] A. P. Key and P. J. Yoder, "Equiprobable and oddball paradigms: two approaches for documenting auditory discrimination," *Developmental Neuropsychology*, vol. 38, no. 6, pp. 402–417, 2013.

[148] H. T. Nagamoto, L. E. Adler, M. C. Waldo, J. Griffith, and R. Freedman, "Gating of auditory response in schizophrenics and normal controls: effects of recording site and stimulation interval on the P50 wave," *Schizophrenia Research*, vol. 4, no. 1, pp. 31–40, 1991.

[149] T. Solis-Escalante, G. Müller-Putz, C. Brunner, V. Kaiser, and G. Pfurtscheller, "Analysis of sensorimotor rhythms for the implementation of a brain switch for

healthy subjects," *Biomedical Signal Processing and Control*, vol. 5, no. 1, pp. 15–20, 2010.

[150] A. K. Engel and P. Fries, "Beta-band oscillations—signalling the status quo?" *Current Opinion in Neurobiology*, vol. 20, no. 2, pp. 156–165, 2010.

[151] Y. Zhang, Y. Chen, S. L. Bressler, and M. Ding, "Response preparation and inhibition: the role of the cortical sensorimotor beta rhythm," *Neuroscience*, vol. 156, no. 1, pp. 238–246, 2008.